RESOURCE ALLOCATION AND PERFORMANCE ANALYSIS FOR NEXT GENERATION WIRELESS COMMUNICATION AND RADIO ASTRONOMY SYSTEMS

by

Dong Han

APPROVED BY SUPERVISORY COMMITTEE:

____

Dr. Hlaing Minn, Chair

____

Dr. Naofal Al-Dhahir

____

Dr. Aria Nosratinia

____

Dr. Murat Torlak

Dedicated to my paternal grandmother.

RESOURCE ALLOCATION AND PERFORMANCE ANALYSIS FOR NEXT GENERATION WIRELESS COMMUNICATION AND RADIO ASTRONOMY SYSTEMS

by

DONG HAN, BE, MS

DISSERTATION

Presented to the Faculty of

The University of Texas at Dallas

in Partial Fulfillment

of the Requirements

for the Degree of

DOCTOR OF PHILOSOPHY IN

ELECTRICAL ENGINEERING

THE UNIVERSITY OF TEXAS AT DALLAS

May 2020

ACKNOWLEDGMENTS

I would like to thank my PhD advisor, Dr. Hlaing Minn, for his suggestions, dedicated guidance, and constant support that made this work possible. I appreciate the valuable remarks of my PhD committee members, Drs. Naofal Al-Dhahir, Aria Nosratinia, and Murat Torlak.

I am also grateful to my collaborators, Drs. Teng Joon Lim and Utku Tefek, for their great guidance and remarks on the machine-type communication part.

I would also like to say a heartfelt thank you to my parents for their patience and encouraging me to follow my dream.

March 2020

RESOURCE ALLOCATION AND PERFORMANCE ANALYSIS FOR NEXT GENERATION WIRELESS COMMUNICATION AND RADIO ASTRONOMY SYSTEMS

Dong Han, PhD
The University of Texas at Dallas, 2020

Supervising Professor: Dr. Hlaing Minn, Chair

Radio spectrum is a limited resource for both scientific research and wireless communications industry. The usage of spectrum can be either active, e.g., wireless data transmission and radar detection, or passive, e.g., radio astronomy observation. However, with the rapid growth of active communication and passive signal receiving demand, more efficient and flexible utilization of spectrum is vital. On the other hand, achieving a high power efficiency is also important to signal transmission and detection. This dissertation devotes to developing machine-type communication systems and distributed radio astronomy systems with limited spectrum and power resources.

For a radio resource limited multi-tier Machine-type Communication (MTC) network, controlling random access congestion while satisfying the unique requirements of each tier and guaranteeing fairness among nodes is always a challenge. In the first part, we study the network dimensioning and radio resource partitioning for the uplink of an MTC network with signal-to-interference ratio (SIR)-based clustering and relaying, where MTC gateways (MTCGs) capture and forward the packets sent from MTC devices (MTCDs) to the base station (BS). Specifically, under transmission outage probability constraints, we investigate the tradeoff between network utility (in terms of transmission capacity and revenue) and

resource allocation fairness. With both outage probability constraints and minimum MTCD density constraints, we propose approaches to maximize the weighted sum of quality of experience (QoE) of different tiers of MTCDs. Furthermore, a transmit power control strategy for MTCG-to-BS link is proposed to achieve a constant data rate.

In the second part of this dissertation, we consider a new large-scale communication scheme where randomly distributed backscatter nodes are involved as secondary users to primary transmitter and primary receiver pairs. The secondary communication between a backscatter transmitter and a backscatter receiver introduces additional double fading channels and has a two-side effect to the primary communications. We derive the signal-to-interference-plus-noise ratio and signal-to-interference ratio based coverage probabilities for two network configuration scenarios, which can provide useful insights in designing such systems.

A conflict of the spectrum rights and needs between active wireless communication systems and passive radio astronomy systems (RASs) has become substantially greater due to the phenomenal expansion of wireless communications and increased interest in RAS observation. For sustainable growth and coexistence of cellular wireless communications (CWC) and RAS, a coordinated shared spectrum access paradigm was recently introduced. Embracing such a paradigm, the third part of this dissertation proposes a distributed auxiliary radio telescope (DART) system which can geographically and spectrally coexist with CWC while offering additional capability or performance enhancement to RAS. Theoretical performance analysis of the DART system with different quantization resolutions is presented, and approximate closed-form expressions are obtained. Adaptation of the cooling power of DART receivers according to the time-varying ambient temperature is also proposed. Furthermore, an analytical expression for the DART system parameters under the shared spectrum access paradigm and cooling power constraint to achieve the same performance as the existing single-dish RAS with a radio quiet zone is developed to provide guidance in the DART system design. The numerical and simulation results illustrate the feasibility and potentials of the proposed DART system.

TABLE OF CONTENTS

ACKNOWLEDGMENTS v
ABSTRACT vi
LIST OF FIGURES xii
LIST OF TABLES xiv
CHAPTER 1 INTRODUCTION 1
1.1 Background 1
1.2 Outline and Contributions 3
1.3 Notations 4
CHAPTER 2 NETWORK DIMENSIONING, QOE MAXIMIZATION AND POWER CONTROL FOR MULTI-TIER MACHINE-TYPE COMMUNICATIONS 5
2.1 Introduction 5
2.2 System Model 9
2.2.1 Communication System and Data Aggregation Model 9
2.2.2 End-to-End Outage Probability and Capacity 11
2.2.3 System Model for MTCG Power Control 14
2.3 Network Dimensioning and Utility Maximization 15
2.3.1 Utility-Optimal Solution 17
2.3.2 Geometric Mean (GM) based Resource Allocation 17
2.3.3 Cauchy-Schwarz (CS) based Resource Allocation 19
2.3.4 Generalized Expression and Utility-Fairness Tradeoff 20
2.3.5 Numerical Performance Comparisons 21
2.4 Resource partitioning with minimum density requirements and QoE maximization 24
2.4.1 Problem Formulation 24
2.4.2 Numerical Results 28
2.5 MTCG uplink power control 30
2.5.1 Development of Outage Probability 35
2.5.2 Development of Aggregated Transmit Power 36

2.5.3 Numerical Results and Discussions 37
2.6 Conclusion 40
CHAPTER 3 COVERAGE PROBABILITY ANALYSIS UNDER CLUSTERED AMBIENT BACKSCATTER NODES 41
3.1 Introduction 41
3.2 System Model 42
3.2.1 Spatial Distribution Models 42
3.2.2 Signal Communication Model 44
3.3 Analysis of Coverage Probability 46
3.3.1 Signal and Interference Power 46
3.3.2 Coverage Probability Expression 47
3.4 Numerical Results and Discussions 50
3.5 Conclusion 56
3.6 Appendix 56
3.6.1 Proof of Lemma 4 56
3.6.2 Proof of Theorem 1 57
3.6.3 Proof of Theorem 2 59
CHAPTER 4 PERFORMANCE ANALYSIS OF DISTRIBUTED AUXILIARY RADIO TELESCOPES UNDER SHARED SPECTRUM ACCESS PARADIGM AND COOLING POWER CONSTRAINT 60
4.1 Introduction 60
4.2 System Model 62
4.3 Performance Analysis of RAS Signal Power Estimation under Finite ADC Resolutions 67
4.4 Approximate Closed-Form Analysis 69
4.5 Combination and Performance Comparison between DART and the Single-Dish RAS 76
4.6 Average Performance Under Cooling Power Constraint 81
4.6.1 DART Performance Analysis 81
4.6.2 Imperfect Temperature Information 87
4.6.3 Combination of DART and Single-dish RAS 89

4.6.4 Simulations 90
4.7 Conclusion 93
4.8 Appendix Proof of proposition 4 94
CHAPTER 5 CONCLUSION 96
REFERENCES 98
BIOGRAPHICAL SKETCH 105
CURRICULUM VITAE

LIST OF FIGURES

2.1 Network Structure (MTCGs capture and relay packets to the BS from MTCDs belonging to different tiers.) 9

2.2 Resource partitioning among MTCDs and MTCGs. 10

2.3 Comparison of resource partitioning parameter. 22

2.4 Comparison of MTCD density. 22

2.5 Comparison of capacity per tier. 23

2.6 Network utilities achieved by different resource partitioning schemes. 23

2.7 Sum QoE under different outage probability constraints. 29

2.8 QoE of tier-1 under different outage probability constraints. 30

2.9 Throughput of tier-1 under different outage probability constraints. 31

2.10 Allowable MTCD density of tier-1 under different outage probability constraints. 32

2.11 Resource allocation ratio of tier-1 under different outage probability constraints. 33

2.12 Comparison of outage capacities at different outage probabilities. ($P_{\mathrm{sum}} = 65$ dBW) 37

2.13 Comparison of outage capacities at different aggregated power levels. 38

2.14 Comparison of $\phi(\gamma)$ at different γ and aggregated power levels using (S1). ($Q_M = 48000,\ \delta_1 = 30,\ \delta_2 = 5,\ \eta = 3,\ \chi_1/\chi_2 = 1$) 39

3.1 Topology of the considered system (scenario-1) 43

3.2 Ambient backscatter scheme 44

3.3 Coverage probability versus TSRNR deducting the absolute value of path loss. ($r_0 = 15, \Gamma = 3\mathrm{dB}, \mu = 1, \beta = 0.8$) 51

3.4 Coverage probability versus useful signal power ratio β. ($r_0 = 15, \Gamma = 3\mathrm{dB}, \mu = 1, \mathrm{TSRNR} = 51\mathrm{dB}$) 52

3.5 Coverage probability versus mean fading power gain. ($r_0 = 15, \Gamma = 3\mathrm{dB}, \beta = 0.8, \mathrm{TSRNR} = 51\mathrm{dB}$) 53

3.6 Coverage probability versus typical PT to PR distance r_0. ($\Gamma = 3\mathrm{dB}, \beta = 0.8, \mu = 1, \mathrm{TSRNR} = 51\mathrm{dB}$) 54

3.7 Coverage probability versus SIR threshold Γ. ($r_0 = 15, \beta = 0.8, \mu = 1, \mathrm{TSRNR} = 51\mathrm{dB}$) 55

4.1 Geometric structure of the DART system and the single-dish RAS 62

4.2 Frame structure of the three-phase spectrum sharing paradigm where the durations of the phases could be different at different hours[52] 64

4.3 RAS receiver structure with noise referencing 64

4.4 The normalized mean of RAS signal power estimation under various ADC resolutions ($\sigma_s^2 = 1,\ N$ or $L = 10^4$) 72

4.5 The normalized variance of RAS signal power estimation under various ADC resolutions ($\sigma_s^2 = 1,\ N$ or $L = 10^4$) 73

4.6 The normalized variance of RAS signal power estimation after the bias compensation ($\sigma_s^2 = 1,\ N$ or $L = 10^4$) 74

4.7 Comparison between BLUE and simple averaging 78

4.8 Accuracy performance comparison and optimal subframe numbers 80

4.9 Solutions of cooling power allocation in terms of cooling temperatures. 86

4.10 Radio astronomical signal power estimation variance comparison among different strategies. 90

4.11 Percentage of power saved by the proposed dynamic cooling power allocation. . 91

LIST OF TABLES

4.1 Comparison of Different Quantization Resolutions 76
4.2 Comparison of Different Numbers of Antenna Elements 77

CHAPTER 1

INTRODUCTION

1.1 Background

Spectrum and power are two major resources for signal transmission and detection. With limited radio resources, next generation wireless communication systems aim to provide ubiquitous connections for a massive amount of devices, next generation radio astronomy systems (RASs) demand more observation opportunity and higher observation performance. Thus, it is necessary to investigate spectrum access and data transmission/receiving schemes for both the wireless communications industry and scientific research.

As part of the Internet-of-things (IoT), MTC devices (MTCDs) are expected to generate a huge amount of data every second. However, without timely gathering and processing of the data, useful information cannot be extracted and acted upon. For instance, future application scenarios include automobiles and unmanned aerial vehicles (UAVs) reporting traffic conditions to a data processing center, sensors transmitting video data to a server, computation-limited devices offloading tasks to a cloud server, etc. These applications may require massive numbers of simultaneous connections between devices and base stations (BS's), which leads to severe congestion on the random access channel (RACH) and impairs the reliability of both the MTC and Human-to-Human (H2H) communications networks [76].

At the same time, the coexistence of diverse devices requiring different Quality of Service (QoS) in terms of latency [58], transmission rate and outage, connection security [67], etc, is a key desired feature of M2M networks. How to efficiently aggregate the huge amount of transmissions while satisfying various QoS requirements and mitigating the negative effects on H2H communication is still a problem.

For large-scale MTC networks involving different tiers of MTCDs, fair resource allocation is always a challenge in that 1) the measurement of fairness is not unique, such as α-fairness

[38], bargaining achievable fairness [85], and 2) the fairness maximization problem may have no global optimal solution. On the other hand, quality of experience (QoE) has recently received more interest in the network design and optimization of many applications such as 5G [53, 41, 82, 86] and cloud computing [10]. As defined by the International Telecommunication Union (ITU), QoE is the overall acceptability of an application or service as perceived subjectively by the end-user [33]. Thus, improving the user experience of data-hungry applications under given QoS requirements is an interesting problem.

The backscatter mechanism enables backscatter transmitters (BTs) to have a simple structure consisting of no active radio frequency (RF) component, which is strongly favored by the Internet-of-things (IoT) application scenarios where many power-limited devices need to be connected. There are three configurations of backscatter communication systems, namely, monostatic backscatter, bistatic backscatter and ambient backscatter [75]. Recently, two research thrusts of backscatter communications are beginning to be eagerly investigated, i.e., the Wireless Powered Backscatter Communication (WPBC) [27] and the Ambient Backscatter Communication (AmBC) [43, 7, 83].

AmBC was proposed to enable devices to communicate by backscattering ambient RF signals. As shown in Fig. 3.2, the BT harvests energy from the ambient signal and quickly transmits its own information bits to the corresponding backscatter receiver (BR) by changing the impedance of its antenna in the presence of the ambient signal [43]. For instance, the BT transmits '0' by setting a high antenna impedance and transmits '1' by adjusting to a low antenna impedance so that the BR can distinguish the different backscattered signal energy levels from the BT.

Next, we consider the spectrum access issue between cellular wireless communications (CWC) and RAS. RAS provides economically and scientifically important observations of the cosmos which benefit the society consistently [55]. As RAS signals are very weak with signal-to-noise power ratio (SNR) as low as -60 dB [33], they are highly sensitive to radio frequency interference (RFI) caused by wireless communication systems. Thus, radio telescopes are built in remote areas surrounded by radio quiet zones for interference isolation [54], [74]. However, the expansion of wireless communication systems in terms of applications [5], radio coverage, radio spectrum [59], and spectrum utilization [49, 30, 39] has caused increased RFI to RAS. The direct results are RFI-corrupted radio astronomical data and less radio astronomical observation opportunities and the consequence is a severe hindrance to science and knowledge discovery. On the other hand, there are increased interests and needs for expanding RAS observations, thus enlarging the conflict of spectrum access rights/needs between the two systems [57, 32, 71].

To mitigate the conflict between CWC and RAS, [52] and [64] recently proposed a new spectrum sharing paradigm where both systems have RFI-free guaranteed spectrum access by means of a three-phase time-division approach. [64] also pointed out the instancy of embracing the new paradigm and justified that different from other spectrum sharing schemes [2, 87, 51, 84, 62, 12] for cognitive radio, the overall spectrum utilization is enhanced by designing time-dependent durations of the spectrum access phases according to the CWC traffic statistics (e.g., on an hourly basis). An extension for coexistence of WiFi and RAS was addressed in [63]. Thus, to accommodate expansions of both CWC and RAS, we embrace the shared spectrum access paradigm of [52] and propose a distributed auxiliary radio telescope (DART) system which can coexist with CWC and conventional single-dish RAS.

1.2 Outline and Contributions

In the first part of the dissertation (CHAPTER 2), we propose a multi-tier MTC data aggregation scheme under different QoS constraints. We develope spectrum resource partitioning approaches to 1) achieve different degrees of tradeoffs between the network utility and the fairness of radio resource allocation, and 2) maximize the weighted sum of QoEs. Next, we propose an MTC gateway transmit power control strategy to accommodate the proposed MTC data aggregation scheme.

In the second part of the dissertation (CHAPTER 3), we consider new large-scale communication scenarios where AmBNs are involved as secondary users. Because of the ambient backscatter mechanism, double fading channels are involved. Then, we investigate the backscatter nodes' interference and/or signal enhancing effect to the primary receiver, and derive the coverage probability of primary transmitter.

In the third part of the dissertation (CHAPTER 4), we propose a DART system to observe and process the radio astronomical signal, which coexists with CWC systems and conventional single-dish RAS. Theoretical performance analysis of the DART system with different quantization resolutions is presented, and approximate closed-form expressions are obtained. Adaptation of cooling power of DART receivers according to the time-varying ambient temperature is also proposed.

1.3 Notations

The following notations are used in this dissertation. x is a scalar. $\mathbf{x}$ is a vector, and $\|\mathbf{x}\|_p$ is its l_p-norm, where $p \geq 0$. Specifically, $\|\mathbf{x}\| = \|\mathbf{x}\|_2$. $(\cdot)^T$and $(\cdot)^H$ are the transpose and conjugate transpose operators respectively. $\mathbb{1}(\cdot)$ stands for the indicator function. $B(\boldsymbol{c}, r)$ represents a ball centered at $\boldsymbol{c}$ with radius r and bold number $\mathbf{0}$ refers to the origin. $\mathbb{E}(\cdot)$ and $\mathrm{Var}(\cdot)$ denote the expectation and variance operators, respectively. Particularly, $\mathbb{E}_{\mathrm{Y}}(\cdot)$ is the expectation operator over Y. $\mathbb{P}(x)$ denotes the probability of x. $\mathfrak{Re}(x)$ and $\mathfrak{Im}(x)$ are the real and image parts of x, respectively. For a real number a, $[a]^+$ represents the maxima of a and zero. $\lfloor a \rfloor$ represents the maximum integer not larger than a, and $\lceil a \rceil$ is the minimum integer not smaller than a.

CHAPTER 2

NETWORK DIMENSIONING, QOE MAXIMIZATION AND POWER CONTROL FOR MULTI-TIER MACHINE-TYPE COMMUNICATIONS

2.1 Introduction

In this chapter, we consider an uplink multi-tier MTC communication system and address the spectrum and power allocation issues. Since MTC data can be efficiently aggregated by a hierarchical network, a number of clustering and resource allocation methods have been proposed to solve this problem[40, 72, 6, 70, 69]. For instance, in [70] and [69], SIR and location based clustering and decode-and-forward relaying schemes for single-tier[1] MTCDs were proposed to maximize the transmission capacity of the MTC network under an outage probability constraint.

In general, orthogonal resource allocation such as time division [47, 46, 50] significantly reduces the interference but has low spectrum efficiency and requires more demanding synchronization. On the other hand, using nonorthogonal resource allocation such as the nonorthogonal multiple access (NOMA) [14, 45] enhances spectrum efficiency but introduces interference, leading to a more complicated decoding scheme [80]. In [70, 69, 26] and this chapter, the combination of orthogonal and nonorthogonal resource allocation approaches is used, where every H2H user, MTCG and MTCD tier are assigned orthogonal channel resources. MTCDs of the same tier share the same band in a nonorthogonal manner. In this way, the conventional H2H communication is free of MTC caused interference and the MTC achieves a higher spectrum efficiency through spectrum reuse.

---

[1]i.e., all MTCDs have the same QoS requirements.

Motivated by the massive data and connection demands and challenges mentioned above, the main goal of this chapter is to realize a cluster-based framework for efficient and flexible MTC data aggregation under multiple QoS constraints. We consider two data aggregation optimization problems, namely 1) network dimensioning and utility maximization with fairness constraints, where we measure fairness by how equally the radio resource is partitioned to different MTCD tiers and maximize the network utility[2] and 2) QoE maximization. Next, to support the data aggregation scheme, we propose a power control strategy for the randomly distributed MTCGs on the MTCG-to-BS link. We note that since the MTCD-to-MTCG links accommodate large numbers of devices based on grant-free random access, power control for MTCDs is impractical and hence is not considered in this chapter.

In the following, we distinguish our work from several state-of-the-art existing works. Regarding the MTC data aggregation, [50] proposed a multi-hop data aggregation scheme and found the tradeoffs between the energy density and the coverage characteristics. They assumed TDMA for the users within each Voronoi cell for the data aggregation. In contrast, in this chapter we investigate a random access approach for single-hop MTC data aggregation so that the devices with different QoS constraints can simultaneously transmit their packets. The authors in [22] designed a two-phase MTC data aggregation scheme for a single tier of devices and solved the problem of resource scheduling between different phases. However, all the aggregators were assumed to have a fixed disc-shaped serving zone (i.e., the MTCD locations are modeled as Matern cluster point process with the aggregator locations being the parent point process), which may limit the efficiency or flexibility of the aggregator when the device locations are uniformly distributed. In contrast, in our data aggregation scheme, the locations of different tiers of devices are assumed to form independent homogeneous PPPs without transmission boundaries and the aggregators (MTCGs) will successfully capture the packets from any MTCD if the SIR permits. While the energy-efficient

[2] The network utility is defined as the weighted sum of network capacity. When the weights are regarded as the price per unit of capacity, the network utility will represent the economic revenue of the network.

data aggregation scheme proposed in [73] requires the MTCDs (smart meters) to know the aggregator positions, the MTCDs in our scheme can transmit without any knowledge of the MTCG positions. Other papers such as [18] also deal with the energy-optimal routing issues in MTC data aggregation, but we focus on the maximization of the network utility and the weighted sum QoE, and the MTCG power control problem.

While the effects of channel inversion power control in the stochastic geometry modeling of cellular networks have been well studied e.g. [56, 42, 15], our proposed MTCG power control strategy focuses on a different aspect from those papers. Specifically, [56] and [15] investigated the channel inversion power control for different uplink transmission models in cellular networks and found the coverage probability based on the complementary cumulative distribution function (CCDF) of the signal-to-interference-plus-noise ratio (SINR). Addationally, using channel inversion to compensate the path loss was considered in [42] to study different spectrum sharing schemes (i.e., overlay and underlay) and transmission mode for D2D communications in cellular networks. In our proposed MTCG power control strategy, we apply channel inversion to compensate both the path loss and the Rayleigh fading. Since the MTCGs are allocated orthogonal radio resources, we derive the CCDF of the received signal-to-noise ratio (SNR) at the BS instead of the SINRs that were considered in [56] and [15], and hence obtain an accurate result without any approximation or modification in the system model.

The main contributions of this chapter are summarized as follows:

1. We propose a multi-tier MTC data aggregation scheme under different QoS constraints. The proposed scheme causes no interference to the conventional H2H communications due to orthogonal resource allocation between M2M and H2H users.

2. Defining the network utility as the weighted sum of network capacity (throughput), we develop three specific resource partitioning approaches and calculate the corresponding MTCD transmission densities of different tiers.

3. We develop a generalized resource partitioning approach to achieve different degrees of tradeoffs between the network utility and fairness of radio resource allocation.

4. Using an increasingly popular performance metric, namely the weighted sum of QoE as a measure of the satisfaction of network throughput, we also develop global optimal resource partitioning solutions.

5. Furthermore, we propose an MTCG transmit power control strategy to enhance the proposed MTC data aggregation scheme. The effect of the aggregated MTCG transmit power on the resource partitioning between MTCGs and MTCDs is analyzed.

The feasibility of this work can be justified as follows. The proposed network dimensioning is applied during the system design phase for the deployment of multi-tier MTCDs and no real-time processing is required. The proposed power control achieves the maximum MTCG-to-BS spectral efficiency with limited aggregated MTCG transmit power, provided that the channel state information (CSI) and the distance between the MTCG and BS are known to the transmitting MTCG. Operator installed devices as well as registered wireless users such as cell phones, laptops and WiFi access points, can serve as MTCGs. Thus, the proposed methods are practical.

The rest of this chapter is organized as follows. The MTC data aggregation model is proposed in Section 2.2, where the end-to-end outage probability is derived and the background of MTCG power control is introduced. In Section 2.3, we propose the network dimensioning and network utility maximization problem and analyze the tradeoff between resource partitioning fairness and network utility. Then, the QoE maximization problem under transmission outage probability constraints and minimum MTCD density constraints is solved in Section 2.4. Next, we investigate the MTCG power control strategies to achieve a constant MTCG-to-BS data rate in Section 2.5. Finally, Section 2.6 concludes this chapter.

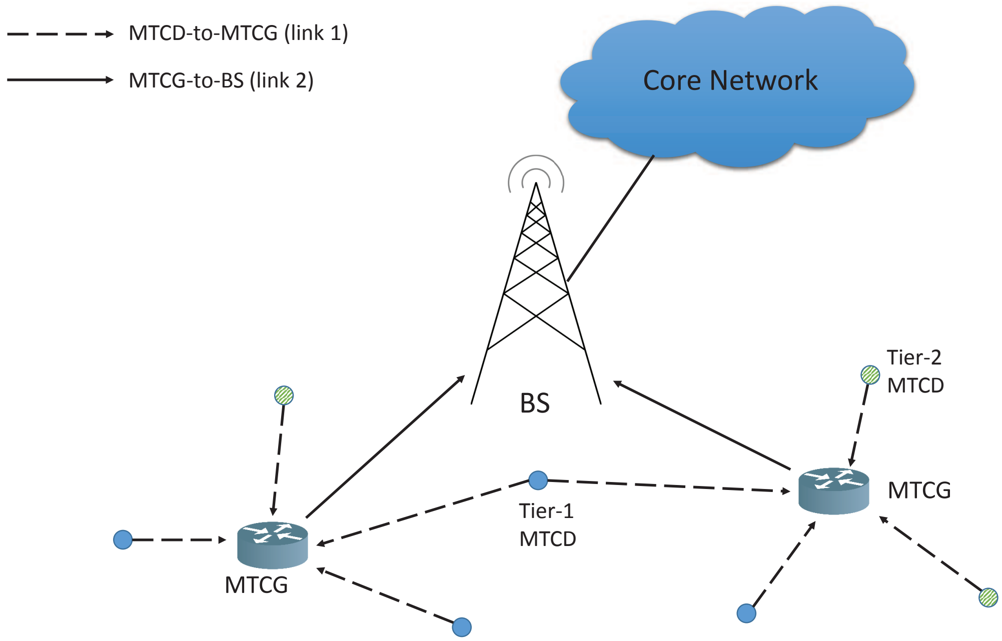

Figure 2.1: Network Structure (MTCGs capture and relay packets to the BS from MTCDs belonging to different tiers.)

2.2 System Model

2.2.1 Communication System and Data Aggregation Model

We consider a single-hop MTC uplink relay scenario as shown in Fig. 2.1. A group of packets sent from MTCDs are gathered by nearby MTCGs and then relayed (in a decode-and-forward way) to the BS so that random access requests to the BS are moderated. The MTCDs are classified into different tiers according to their required transmission outage probabilities $\{\zeta_j\}$. We assume that there are N tiers of devices and the locations of the tier j MTCDs form a homogeneous spatial PPP, $\Phi_{D_j} = \{X_{j,k}\}$ with density λ_j, $\forall j = 1, \ldots, N$. In compact form, we use vector $\boldsymbol{\lambda} = (\lambda_1, \ldots, \lambda_N)^{\mathrm{T}}$ to represent the densities. Similarly the MTCG locations form a homogeneous spatial PPP, $\Phi_G = \{Y_i\}$ with density λ_G. Φ_{D_j}'s are assumed to be pairwise independent from each other and from Φ_G.

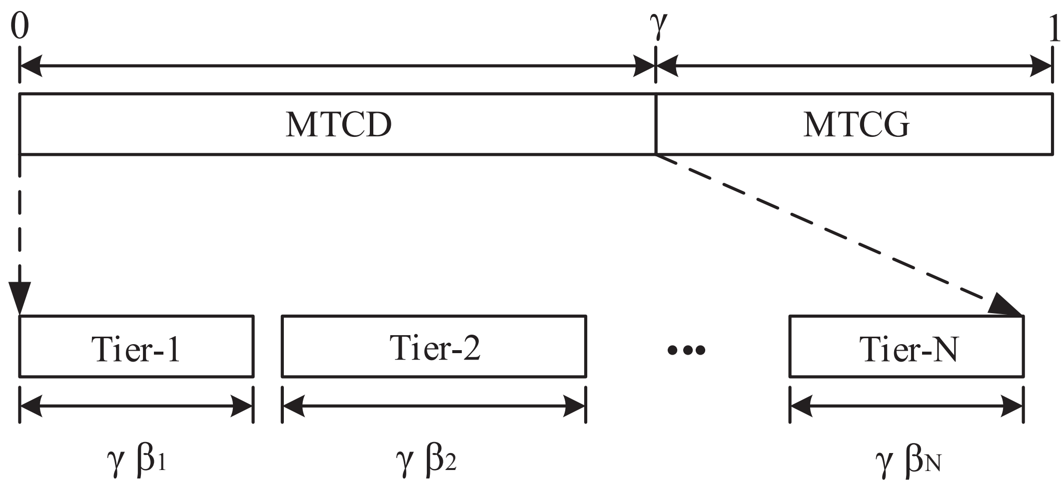

Figure 2.2: Resource partitioning among MTCDs and MTCGs.

The total amount of radio spectrum resources for MTC is limited and it should be partitioned among MTCGs and different tiers of MTCDs. Assuming that there are Q_M resource blocks (RBs) reserved for M2M communications and $Q_1 = \gamma Q_M$ RBs allocated for MTCD-to-MTCG link (link 1), then $Q_2 = (1-\gamma)Q_M$ RBs are allocated for MTCG-to-BS link (link 2), where $\gamma \in [0, 1]$. Next, $Q_1^j = \beta_j Q_1$ RBs are allocated for the jth tier of MTCDs, where $0 \leq \beta_j$ and $\sum_{j=1}^{N} \beta_j = 1$. The considered resource partitioning is shown in Fig. 2.2. We denote the spectrum partitioning factors in compact form with vector $\boldsymbol{\beta} = (\beta_1, \ldots, \beta_N)^{\mathrm{T}}$. Since [70] stated equal resource partitioning among MTCGs is optimal by showing that all MTCGs capture a packet with the same probability, Q_2/G RBs are allocated for each MTCG, where constant G is the number of MTCGs in the coverage of BS's[3].

Furthermore, the MTCDs use the same modulation and coding scheme to send fixed-length packets with a constant transmit power. The MTCGs decode the captured MTCD

[3]While [70] considers only one BS, we consider multiple BS's to analyze the power control problem. The total resource Q_M is then from all the considered BS's.

packets and forward the message on orthogonal channels to the BSs under cellular standards. In this scheme, the channel state information (CSI) of link 1 is not required by MTCDs unless adaptive modulation schemes are used, making the system simple and scalable. The CSI of link 2 is assumed known to the MTCGs since they are direct users in the cellular networks. Since link 1 and link 2 use different wireless technologies, transmitting the same message through link 1 and link 2 may require different amount of resources. We assume each MTCD needs δ_1 RBs to transmit one packet, and each MTCG needs δ_2 RBs in order to relay a MTCD's packet to the BS. Therefore, each MTCG can have at most $U_2 = \lfloor Q_2/(G\delta_2)\rfloor$ relay channels, while the jth tier of MTCDs has $U_1^j = \lfloor \beta_j Q_1/\delta_1 \rfloor$ orthogonal data channels and the total number of link 1 channels is $U_1 = \sum_{j=1}^{N} U_1^j \approx \lfloor Q_1/\delta_1 \rfloor$. We also assume independent and identically distributed (i.i.d.) Rayleigh fading with unit average power gain on each channel, and path loss with exponent α over all channels, i.e., the path loss from the transmitter to the receiver at a distance of r is $r^{-\alpha}$.

The data aggregation process is designed as follows. First, each active MTCD randomly selects a channel among those that are allocated for its tier. Since two or more MTCDs can potentially transmit on the same channel, they may interfere with each other. Second, each MTCG listens to all the MTCD-to-MTCG channels, but only chooses the MTCD with the highest average received power (i.e., the nearest MTCD) on each channel. Also, the MTCGs can successfully decode a packet only when their received SIR is higher than a threshold η. Third, the MTCGs treat packets from all MTCDs equally in the sense that if no greater than U_2 packets are decoded, all of them will be relayed; otherwise, the MTCG will randomly choose to relay U_2 packets and drop the rest.

2.2.2 End-to-End Outage Probability and Capacity

In the data aggregation process, we note that the resource partitioning between link 1 and link 2 determines the number of channels U_1 and U_2 for the two links, and hence affects the end-to-end outage probability. Intuitively, allocating more resources to link 1 leads to greater transmission density and less interference, but higher packet drop rate at the gateways. Therefore, there would be an optimal operating point in the resource partitioning between link 1 and link 2 as we can see in the next section.

Note that the end-to-end outage probability for single-tier SIR-based clustering and relaying MTC data aggregation scheme was analyzed in [70]. Therein, it was clarified that successful transmission is equivalent to the joint occurrence of three events, namely a) the typical MTCD is the nearest MTCD on a randomly selected channel u to an MTCG located at Y_i, denoted by $\mathcal{N}^u_{X_0,Y_i}$, b) the typical MTCD's packet on channel u is successfully captured by an MTCG located at Y_i, denoted by $\mathcal{C}^u_{X_0,Y_i}$, c) the typical MTCD's packet received on u is successfully relayed by an MTCG located at Y_i, denoted by $\mathcal{R}^u_{X_0,Y_i}$, where X_0 represents the nearest MTCD to Y_i transmitting on channel u. Provided that the MTCD density is λ_D, the (conditional) probabilities of these three events are

$$\Pr(\mathcal{N}^u_{X_0,Y_i}) = \exp\left(-\pi\frac{\lambda_D}{U_1}\|X_0 - Y_i\|^2\right) \tag{2.1}$$

$$\Pr(\mathcal{C}^u_{X_0,Y_i}|\mathcal{N}^u_{X_0,Y_i}) = \exp\left(-\pi\frac{\lambda_D}{U_1}\eta^{\frac{2}{\alpha}}\|X_0 - Y_i\|^2 K_{\alpha,\eta}\right) \tag{2.2}$$

$$\Pr(\mathcal{R}^u_{X_0,Y_i}|\mathcal{C}^u_{X_0,Y_i}) = 1-\varepsilon = 1-\sum_{n=U_2}^{U_1-1}\begin{pmatrix} U_1-1 \\ n \end{pmatrix} p^n_{c,\mathrm{SIR}} \times (1-p_{c,\mathrm{SIR}})^{U_1-1-n}\left(1-\frac{U_2}{1+n}\right) \tag{2.3}$$

where $K_{\alpha,\eta} = \int_{\eta^{-\frac{2}{\alpha}}}^{\infty} \frac{dt}{1+t^{\alpha/2}}$, $p_{c,\mathrm{SIR}} = \left(1+\eta^{\frac{2}{\alpha}}K_{\alpha,\eta}\right)^{-1}$ is the probability of an MTCG capturing a packet on any link 1 channel and ε represents the link 2 outage probability. We note that if $U_2 \geq U_1$, then $\varepsilon = 0$.

To be specific, Eq. (2.1) is the probability of there being no MTCDs in the circular region $B(Y_i, \|X_0 - Y_i\|)$[4], where $B(\boldsymbol{x}_c, \rho)$ represents a circle centered at $\boldsymbol{x}_c$ with radius ρ. Eq. (2.2) is achieved by deriving the Laplace transform of the probability density function (PDF) of the sum interference observed at Y_i from all MTCDs transmitting on channel u. Then, the expression of $p_{c,\mathrm{SIR}}$ is found by de-conditioning Eq. (2.2) over the distance $\|X_0 - Y_i\|$. Since the capture events are independent and equally probable across all channels with probability $p_{c,\mathrm{SIR}}$, the total number of the packets captured by the MTCG at Y_i is Binomial distributed as $\mathrm{Bin}(U_1, p_{c,\mathrm{SIR}})$. Finally, by considering the failure due to random packet dropping at the MTCG when $U_2 < U_1$, Eq. (2.3) is obtained.

Next, applying the chain rule on (conditional) probabilities in (2.1) - (2.3), the end-to-end outage probability of a typical MTCD transmission is expressed as

$$\begin{aligned}\epsilon(\lambda_D,\gamma) =& \mathbb{E}\prod_{Y_i\in\Phi_G}\left[1-\Pr(\mathcal{R}^u_{X_0,Y_i}|\mathcal{C}^u_{X_0,Y_i})\times\Pr(\mathcal{C}^u_{X_0,Y_i}|\mathcal{N}^u_{X_0,Y_i})\Pr(\mathcal{N}^u_{X_0,Y_i})\right]\\ =& \exp\left(-\frac{\lambda_G U_1}{\lambda_D\left(1+\eta^{2/\alpha}K_{\alpha,\eta}\right)}(1-\varepsilon)\right),\end{aligned} \tag{2.4}$$

where in the derivation of Eq. (2.4), probability generating functional (PGFL)[23] and variable change $t \leftarrow r^2$ (r is the radial coordinate of a two-dimensional polar coordinate) are applied. The details of the derivation for (2.1)-(2.4) can be found in [70].

For the multi-tier scenario, we apply the same data aggregation scheme, and the gateways treat all the packets equally. Thus, the (conditional) probabilities of the events, $\mathcal{N}^{u_j}_{X_0,Y_i}$ and $\mathcal{C}^{u_j}_{X_0,Y_i}|\mathcal{N}^{u_j}_{X_0,Y_i}$ are only modified by $\lambda_j \leftarrow \lambda_D$ and $U_1^j \leftarrow U_1$ for the jth tier, while $\Pr(\mathcal{R}^{u_j}_{X_0,Y_i}|\mathcal{C}^{u_j}_{X_0,Y_i})$ is the same as (2.3) for all tiers because each MTCG listens to the U_1 channels but not some specific U_1^j channels. Therefore, the end-to-end outage probabilities can be easily extended from (2.4) as

$$\epsilon(\lambda_j,\gamma) = \exp\left(-\frac{\lambda_G U_1^j}{\lambda_j\left(1+\eta^{2/\alpha}K_{\alpha,\eta}\right)}(1-\varepsilon)\right) \approx \exp\left(-\frac{\beta_j\phi(\gamma)}{\lambda_j}\right), \tag{2.5}$$

where we define

$$\phi(\gamma) \triangleq \frac{\lambda_G U_1}{1+\eta^{2/\alpha}K_{\alpha,\eta}}(1-\varepsilon) \tag{2.6}$$

as a function[4] of γ. We note that the approximation in (2.5) is due to the approximation in allocating the resource blocks, i.e., $U_1^j = \lfloor \beta_j Q_1/\delta_1 \rfloor \approx \beta_j \lfloor Q_1/\delta_1 \rfloor \approx \beta_j U_1$, and it is asymptotically close to the exact value of $\epsilon(\lambda_j, \gamma)$ when Q_1/δ_1 is large.

According to [78], the transmission capacity or area spectral efficiency for a single type of device is the density of the simultaneously transmitting MTCDs multiplied with their end-to-end transmission success probability. Thus, for an N-tier MTC network, the sum network capacity can be expressed by $\sum_{j=1}^{N} \lambda_j (1 - \epsilon_j)$, where $\epsilon_j = \epsilon(\lambda_j, \gamma)$ is the end-to-end outage probability of the jth tier of MTCDs. We may also consider the economic revenue of this MTC network as $\sum_{j=1}^{N} \lambda_j \pi_j (1 - \epsilon_j)$, where π_j denotes the price or revenue per unit capacity of tier j.

2.2.3 System Model for MTCG Power Control

We analyze the MTCG transmit power control strategy under an aggregated MTCG power constraint. Recall that to analyze the worst-case interference at MTCGs and the end-to-end MTC outage probabilities, the MTCD and MTCG locations are assumed to form homogeneous PPPs in an infinite region. However, investigating the aggregated MTCG transmit power consumption in an infinite region will result in unrealistically unbounded results. Therefore, we assume the MTCG locations form a PPP with constant density λ_G within a finite circular region $B(\mathbf{0}, \rho)$, where $B(\boldsymbol{x}_c, \rho)$ represents a circle centered at $\boldsymbol{x}_c$ with radius ρ, and the BS locations form another PPP with density λ_B within this region. We note that as long as the area of the finite region is large enough to contain a reasonable number of devices, the analytical results based on the infinite region scenario can be close to the results based on the finite region scenario, since the interference to a typical receiver is dominated by the nearby transmitters[16]. To be more convincing, [70] shows that the

[4] $\phi(\gamma)$ is also a function of λ_G and $\max \phi(\gamma)$ determines whether the MTCG deployment is able to support the required MTCD densities with the outage probability constraint.

single-tier transmission capacity simulated with Monte Carlo method in a finite region is close to the corresponding analytical capacity based on an infinite region.

We consider that the transmissions between MTCGs and the BS encounter both Rayleigh fading and path loss. The path loss model is represented as $L(r) = r^{-\alpha}$, where r is the distance between the MTCG and the BS. Practically, $L(r)$ holds for $r \geq 1$, meaning that the path loss is normalized to unity at unit distance. We note that some papers use the path loss model $L'(r) = \frac{1}{1+r^\alpha}$ to avoid the singularity at the origin [31]. Our analysis applies to both $L(r)$ and $L'(r)$ and the numerical results based on both path loss models are similar since for most of the distances we have $r \gg 1$. Therefore, to be consistent with the data aggregation model, we chose $L(r)$ as the path loss model to analyze MTCG power control strategies.

2.3 Network Dimensioning and Utility Maximization

In this section, we consider the scenario of N tiers of MTCDs for which the required outage probabilities are $\zeta_1, \ldots, \zeta_N$. In particular, assuming the MTCGs treat all the packets equally, for the jth tier, the outage probability $\epsilon(\lambda_j, \gamma)$ is upper bounded by ζ_j. Accordingly, the network utility maximization problem can be formulated as

$$(\text{P1}): \max_{\boldsymbol{\lambda},\boldsymbol{\beta},\gamma} \sum_{j=1}^{N} \lambda_j \pi_j \left(1 - \exp\left(-\frac{\beta_j \phi(\gamma)}{\lambda_j}\right)\right) \tag{2.7a}$$

$$\text{s.t.} \;\; 0 \leq \lambda_j \leq \frac{\beta_j \phi(\gamma)}{\ln(1/\zeta_j)}, \tag{2.7b}$$

$$\sum_{j=1}^{N} \beta_j = 1, \;\; 0 \leq \beta_j \tag{2.7c}$$

$$0 \leq \gamma \leq 1 \tag{2.7d}$$

where the right-hand-side inequality in (2.7b) comes from the requirement that $\epsilon(\lambda_j, \gamma) \approx \exp(-\beta_j \phi(\gamma)/\lambda_j) \leq \zeta_j$. Note that $\lambda_j \left(1 - \exp\left(-\frac{\beta_j \phi(\gamma)}{\lambda_j}\right)\right)$ is the effective network throughput of tier-j MTCDs, and thus when π_j's denote the pricing strategy (i.e., revenue per unit capacity) of tier j, the objective can be regarded as the economic revenue of the MTC network, and when π_j's are not given specific physical meanings, the objective is the weighted sum network capacity of the MTC network.

Lemma 1. *The network utility maximization problem (P1) described by (2.7a) - (2.7d) can be simplified to*

$$\text{(P1-1)}: \quad \max_{\boldsymbol{\beta}} \sum_{j=1}^{N} \frac{\beta_j \pi_j (1-\zeta_j)}{\ln(1/\zeta_j)} \phi(\gamma^\star) \tag{2.8a}$$

$$\text{s.t.} \quad \sum_{j=1}^{N} \beta_j = 1, \; 0 \le \beta_j, \tag{2.8b}$$

where $\gamma^\star = \arg\max \phi(\gamma)$ is the optimal resource partitioning parameter that maximizes the objective functions of (P1-1) and (P1). Correspondingly, the optimal MTCD density of the jth tier relates to its bandwidth proportion as

$$\lambda_j^\star = \frac{\phi(\gamma^\star)\beta_j}{\ln(1/\zeta_j)}. \tag{2.9}$$

Proof. Given $\boldsymbol{\beta}$ and γ, objective function in (2.7a) increases monotonically with λ_j, $\forall j$. Thus, according to the constraint on λ_j in (2.7b), the MTCD density of the jth tier should relate to its bandwidth proportion as

$$\lambda_j = \frac{\phi(\gamma)\beta_j}{\ln(1/\zeta_j)} \tag{2.10}$$

to achieve maximum network utility. Substituting λ_j in (2.10) into (2.7a), we simplify the original problem to

$$\max_{\boldsymbol{\beta},\gamma} \sum_{j=1}^{N} \frac{\beta_j \pi_j (1-\zeta_j)}{\ln(1/\zeta_j)} \phi(\gamma) \tag{2.11a}$$

$$\text{s.t.} \quad \sum_{j=1}^{N} \beta_j = 1, \; 0 \le \beta_j, \; 0 \le \gamma \le 1, \tag{2.11b}$$

where we can recognize that to maximize the objective function (2.11a), we should have $\gamma^\star = \arg\max \phi(\gamma)$. Then, the corresponding optimal $\lambda_j^\star$ is achieved according to (2.10). Thus the problem is further simplified to (P1-1) and Lemma 1 is proved. $\square$

In the rest of this section, we will discuss network dimensioning and resource partitioning methods that solve the network utility maximization problem (P1) while satisfying different fairness requirements in resource allocation.

2.3.1 Utility-Optimal Solution

According to Lemma 1, we solve (P1) with the simplified problem (P1-1). As we can always find a tier n^* such that $n^* = \arg\max_j \frac{\pi_j(1-\zeta_j)}{\ln(1/\zeta_j)}$, allocating all resources to this tier, i.e., $\boldsymbol{\beta}^* = \boldsymbol{e}_{n^*}$[5] and thereby $\boldsymbol{\lambda}^* = \frac{\phi(\gamma^\star)}{\ln(1/\zeta_{n^*})}\boldsymbol{e}_{n^*}$, will achieve the maximum network utility

$$R^* = \frac{\pi_{n^*}(1-\zeta_{n^*})}{\ln(1/\zeta_{n^*})}\phi(\gamma^\star). \tag{2.12}$$

For the convenience of analysis, let $\mathbf{z} = (z_1, z_2, ..., z_N)^T$ where $z_j = \frac{\pi_j(1-\zeta_j)}{\ln(1/\zeta_j)} \geq 0$, and we rewrite (2.12) as

$$R^* = \|\mathbf{z}\|_\infty \phi(\gamma^\star) \tag{2.13}$$

where $\|\cdot\|_\infty$ represents the infinity norm. We note this resource allocation method strongly favors the tier with the least stringent outage constraint, or the one paying the highest price. We also notice that z_j monotonically increases with ζ_j and π_j. Intuitively, z_j reflects the favorability of the jth tier from the perspective of the network operator, since a greater z_j indicates either a higher price π_j or a less stringent (a greater value of) outage probability constraint ζ_j. In the following subsections, we will provide other resource allocation methods focusing on the fairness issue.

2.3.2 Geometric Mean (GM) based Resource Allocation

Instead of maximizing weighted sum network capacity, we replace the objective function of (P1) in (2.7a) with the geometric mean of the weighted capacities of all tiers as

$$\frac{1}{N}\log R_{\text{total}} = \frac{1}{N}\log\left(\prod_{j=1}^{N} R_j\right) = \frac{1}{N}\sum_{j=1}^{N}\log R_j \tag{2.14}$$

[5] We define $\boldsymbol{e}_i = (0, \ldots, 0, 1, 0, \ldots, 0)^{\mathrm{T}}$ where only the ith element is 1.

where the tier-utility, $R_j = \lambda_j \pi_j \left(1 - \exp\left[-\frac{\beta_j \phi(\gamma)}{\lambda_j}\right]\right)$, represents the weighted capacity or economic revenue of the jth tier. The motivation of using this logarithmic product function comes from a branch of cooperative game theory, namely bargaining theory[28] and the notion of proportional fairness[36]. Further justification of this bargaining model is beyond the scope of this chapter, and interested readers can refer to section 7.1.3 of [28] and [36, 9] for more details. Similar to the proof of Lemma 1, we notice that the objective increases monotonically with λ_j. Thus, to satisfy the first constraint of (P1) by equality, optimal MTCD density of the jth tier should also be the $\lambda_j^\star$ specified in (2.9). With this knowledge, we obtain the following simplified problem,

$$\text{(P1-2)}: \quad \max_{\boldsymbol{\beta}} \sum_{j=1}^{N} \log\left(\frac{\beta_j \pi_j (1-\zeta_j)}{\ln(1/\zeta_j)} \phi(\gamma^\star)\right) \tag{2.15a}$$

$$\text{s.t.} \quad \sum_{j=1}^{N} \beta_j = 1, \; 0 \leq \beta_j. \tag{2.15b}$$

The objective function in (2.15a) can be rewritten as

$$\max_{\boldsymbol{\beta}} \sum_{j=1}^{N} \log \beta_j + \sum_{j=1}^{N} \log\left(\frac{\pi_j (1-\zeta_j)}{\ln(1/\zeta_j)} \phi(\gamma^\star)\right) \tag{2.16}$$

which allows us to maximize the objective function over β_j. Due to the concavity of log function, equal partition is the optimal GM-based resource allocation among MTCDs, i.e., $\beta_j^{\mathrm{GM}} = \frac{1}{N}$. Thus, the corresponding MTCD density is $\lambda_j^{\mathrm{GM}} = \frac{\phi(\gamma^\star)}{N \ln(1/\zeta_j)}$ according to (2.9). Substituting λ_j, β_j and γ in the objective function of (P1) with λ_j^{GM}, β_j^{GM} and $\gamma^\star$ respectively, the network utility achieved by the GM-based method is

$$R^{\mathrm{GM}} = \frac{1}{N} \sum_{j=1}^{N} \frac{\pi_j (1-\zeta_j)}{\ln(1/\zeta_j)} \phi(\gamma^\star) = \frac{1}{N} \|\mathbf{z}\|_1 \phi(\gamma^\star) \tag{2.17}$$

where $\|\cdot\|_1$ represents the l_1-norm. Different from the method introduced in section III-A, this GM-based method achieves absolute fairness in terms of an equal resource allocation across all tiers of MTCDs, regardless of the outage probability constraints.

Comparing the network utility achieved by the GM-based method in (2.17) with the maximum value in (2.13), we have $R^{\mathrm{GM}} \leq R^*$, where equality holds when all the elements in $\mathbf{z}$ are equal. Clearly, the fairness achieved by the GM-based method is at the cost of network utility. On the other hand, if the price values (weights) π_j's are adjusted to make the value of elements in $\mathbf{z}$ more uniform, the difference between R^{GM} and R^* will be reduced.

2.3.3 Cauchy-Schwarz (CS) based Resource Allocation

While the GM-based method results in equal partitioning, and the utility-optimal allocation yields maximum network utility, we are also interested in a trade-off between fairness and efficiency, which motivated us to propose the CS-based resource allocation.

We consider the optimization problem (P1-1). With Cauchy-Schwarz inequality, we have

$$(\boldsymbol{\beta}^T \mathbf{z})^2 \leq \|\boldsymbol{\beta}\|_2^2 \|\mathbf{z}\|_2^2 \tag{2.18}$$

where $\|\cdot\|_2$ represents l_2-norm and the equality holds when $\beta_1/z_1 = \ldots = \beta_N/z_N$. Specifically, with this equality and the fact that the summation of all the nonnegative β_j is 1, we have

$$\beta_j^{\mathrm{CS}} = \frac{z_j}{\|\mathbf{z}\|_1} = \frac{\frac{\pi_j(1-\zeta_j)}{\ln(1/\zeta_j)}}{\sum_{l=1}^N \frac{\pi_l(1-\zeta_l)}{\ln(1/\zeta_l)}}. \tag{2.19}$$

We can see that this solution relates the resource partitioning parameter to the outage probability constraints and prices. For each tier, the stricter the outage constraint is, less resource is allocated; and the higher the price is, more resources are allocated. Therefore, we set β_j^{CS} as the resource partitioning parameter and name this method as CS-based resource allocation.

By substituting β_j with β_j^{CS} in (2.9), the maximum transmission density for tier j is

$$\lambda_j^{\mathrm{CS}} = \frac{\frac{\pi_j(1-\zeta_j)}{[\ln(1/\zeta_j)]^2}}{\sum_{l=1}^N \frac{\pi_l(1-\zeta_l)}{\ln(1/\zeta_l)}} \phi(\gamma^\star) \tag{2.20}$$

which results in the network utility

$$R^{\mathrm{CS}} = \frac{\sum_{j=1}^{N}\left(\frac{\pi_j(1-\zeta_j)}{\ln(1/\zeta_j)}\right)^2}{\sum_{j=1}^{N}\frac{\pi_j(1-\zeta_j)}{\ln(1/\zeta_j)}}\phi(\gamma^\star) = \frac{\|\mathbf{z}\|_2^2}{\|\mathbf{z}\|_1}\phi(\gamma^\star). \tag{2.21}$$

Compared with the GM-based method that provides equal resource partitioning for all tiers, the CS-based method provides less uniform resource allocation for different tiers. Furthermore, since $\|\mathbf{z}\|_1^2 \leq N\|\mathbf{z}\|_2^2$ for $\mathbf{z} \succeq 0$, we can conclude $R^{\mathrm{GM}} \leq R^{\mathrm{CS}}$. The equality holds when all the elements in $\mathbf{z}$ are equal. In other words, the equality condition is

$$\pi_j = \frac{\ln(1/\zeta_j)}{1-\zeta_j}a, \quad j = 1, ..., N \tag{2.22}$$

where a is a nonnegative constant. Equation (2.22) indicates that the GM-based resource allocation can be regarded as a special case of the CS-based method and that, this pricing (weighting) strategy serves as a reference to evaluate fairness level in the CS-based resource allocation process. In general, the closer to this pricing strategy, the fairer resource allocation will be. We notice that the relationship between the three resource allocation methods is

$$R^{\mathrm{GM}} \leq R^{\mathrm{CS}} \leq R^* \tag{2.23}$$

where both inequalities are satisfied with equality when (2.22) holds. Besides, the GM-based method and the utility-optimal allocation method achieve absolute fairness and absolute unfairness respectively, while the CS-based method offers a trade-off between the two extremes.

2.3.4 Generalized Expression and Utility-Fairness Tradeoff

Recalling the three proposed approaches to allocate the radio resource in the MTC data aggregation scheme, we found the utility-optimal solution by directly solving (P1-1) but it results in all resource being monopolized by one specific tier. We then change the linear summation into the sum-log form which is the same to the objective in a bargaining process and an equal resource partitioning is achieved. A heuristic CS-based resource allocation is then proposed to trade off the needs of maximal network utility for a fair resource allocation. Nevertheless, whether the CS-based method keeps a good balance between utility and fairness given the specific QoS requirements, i.e., the outage probability constraints, and the pricing strategy, is not clarified. In this subsection, we generalize an uniform expression (2.24) from the above three resource partitioning parameters $\boldsymbol{\beta}^*$, $\boldsymbol{\beta}^{\mathrm{GM}}$ and $\boldsymbol{\beta}^{\mathrm{CS}}$.

$$\beta_j(k) = \frac{z_j^k}{\sum_{i=1}^N z_i^k} = \begin{cases} \frac{1}{\|\boldsymbol{z}\|_0}, & k = 0 \text{ (GM-based)} \\ \vdots & \\ \frac{z_j}{\|\boldsymbol{z}\|_1}, & k = 1 \text{ (CS-based)} \\ \vdots & \\ \frac{z_j^\infty}{\sum_{i=1}^N z_i^\infty}, & k = \infty \text{ (Utility-optimal)}, \end{cases} \tag{2.24}$$

$\forall j \in \{1, \ldots, N\}$. This generic resource partitioning based on k-norm can achieve different fairness levels by varying the value of a single factor $k \in [0, +\infty]$. Specifically, the fairness level increases monotonically with decreasing k. For instance, when $k = 0,\ 1$ and ∞, the generic resource allocation parameter $\beta_j(k)$ corresponds to the GM-based solution β_j^{GM}, CS-based solution β_j^{CS} and utility-optimal solution β_j^*, respectively. Furthermore, with (2.9), the network utility achieved by the generic resource partitioning is

$$\sum_{i=1}^N \lambda_i \pi_i (1 - \zeta_i) = \frac{\sum_{i=1}^N z_i^{k+1}}{\sum_{i=1}^N z_i^k} \phi(\gamma^\star) \tag{2.25}$$

where k is the parameter as in (2.24).

2.3.5 Numerical Performance Comparisons

Comparisons among different resource partitioning methods are shown in Fig. 2.3-2.6 respectively. To be specific, we consider $N = 10$ tiers of MTCDs with outage probability constraints, $\zeta_1, \ldots, \zeta_N$, ranging from 0.05 to 0.5 (the tier with a larger number has a larger outage probability) and assume that $\phi(\gamma^\star) = 1, \pi_j = 1, \forall j$. As can be seen from Fig. 2.3,

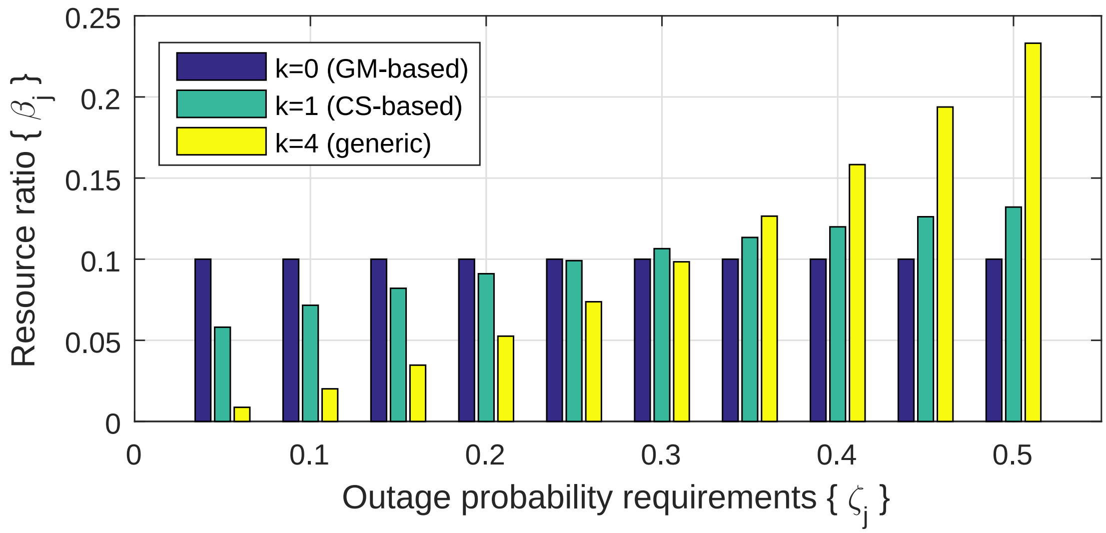

Figure 2.3: Comparison of resource partitioning parameter.

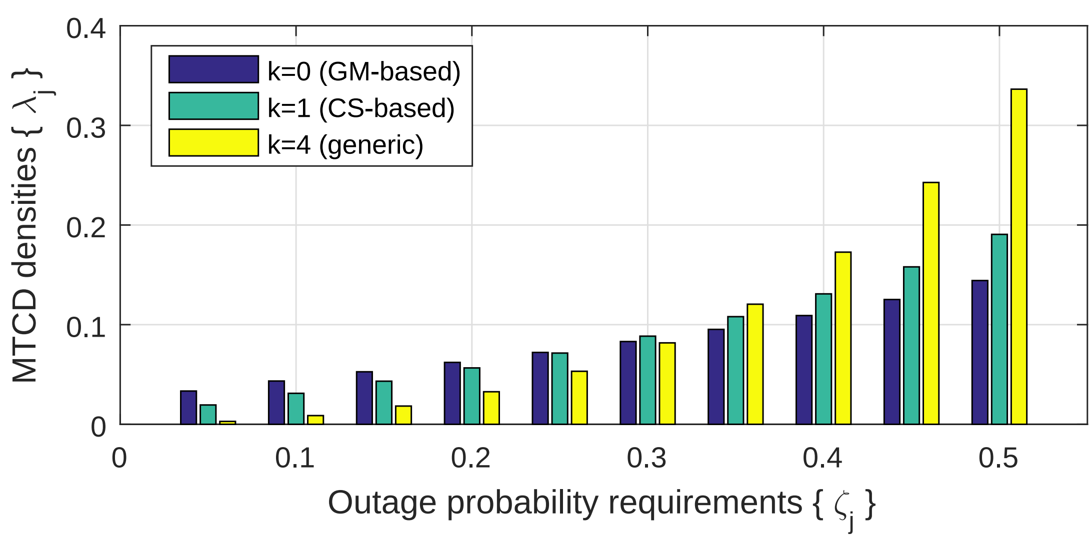

Figure 2.4: Comparison of MTCD density.

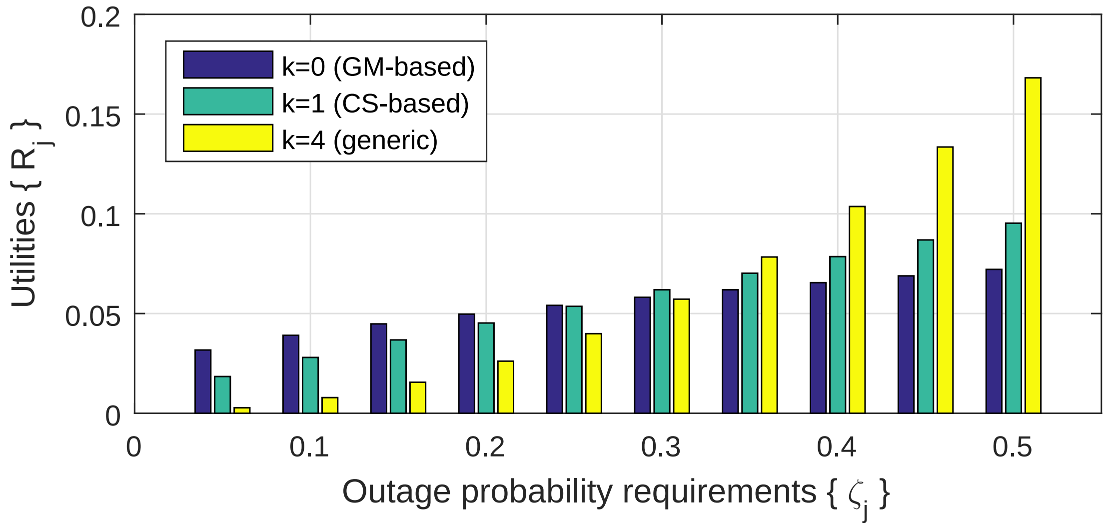

Figure 2.5: Comparison of capacity per tier.

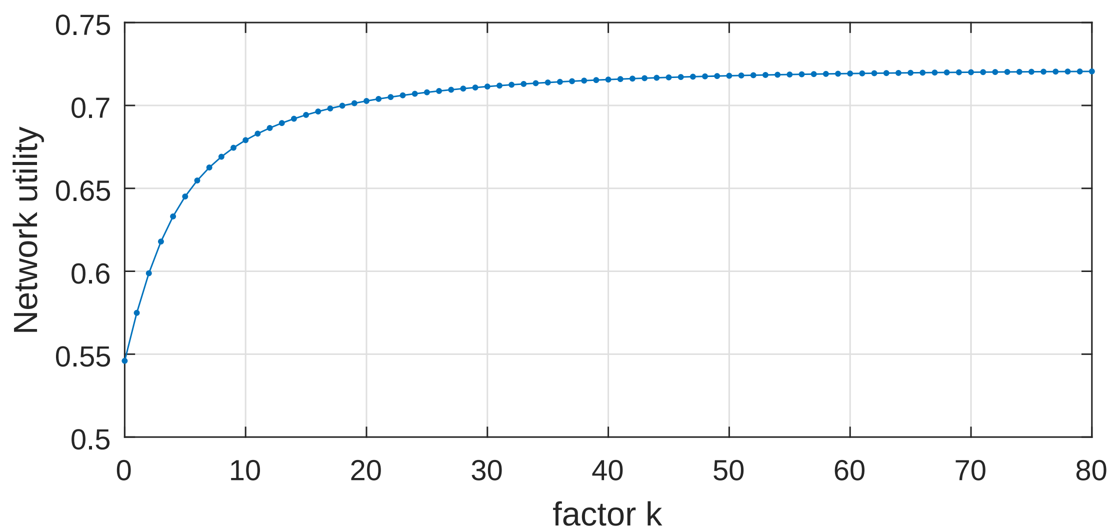

Figure 2.6: Network utilities achieved by different resource partitioning schemes.

while GM based method (when $k = 0$) allocates the resources equally, the increase of the value of k tends to allocate less resources to the tiers with more stringent outage constraints as the green and yellow bars show. Under our definition of fairness, the GM-based method provides the fairest allocation, the utility-optimal resource allocation method (when $k = +\infty$) is the most unfair one, and the methods when $k \in (0, +\infty)$ achieves different degrees of fairness between the two extremes. The differences in the focus on fairness lead to the differences in MTCD density and transmission capacity which are shown in Fig. 2.4 and Fig. 2.5 respectively. Comparing the resource partitioning methods for different values of k in Fig. 2.4 and Fig. 2.5, it is clear that a larger k results in higher densities and per-tier utilities of the tiers with more stringent outage constraints, than those of the other two methods. On the other hand, as shown in Fig. 2.6, the network utility increases with the increase of the k value and it converges to around 0.72 when all the resources are monopolized by a single tier.

2.4 Resource partitioning with minimum density requirements and QoE maximization

2.4.1 Problem Formulation

The network dimensioning solution provides an approach to allocate the radio resources among the gateways and different MTCD tiers under QoS constraints in terms of outage probability such that the densities of the MTCDs of different tiers are found to maximize the network utility. The essential of the proposed network dimensioning approach is that it can achieve different trade-off levels between the network utility and the fairness of resource partitioning.

On the other hand, the minimum MTCD transmission density (or equivalent capacity) requirement might be specified in some practical scenarios such that each tier of MTCDs can be guaranteed to conduct some basic tasks and achieve a basic level of satisfaction. In practice, the user's satisfaction towards a certain tier-utility, e.g., capacity, delay, etc., is also regarded as quality of experience (QoE). The QoE is not a linear function of the corresponding tier-utility but has a logarithmic relationship to it according to the Weber-Fechner Law (WFL). Intuitively, the QoE increases rapidly when the current experience is very poor but increases slightly when the current experience is already good enough.

In this section, our objective is to maximize the weighted sum of the QoEs of different tiers instead of the linearly weighted sum of the capacities. The QoE is estimated by means of how satisfiable the tier-utility R_j is to the jth tier. The QoE factor for the jth tier is represented by

$$\Gamma_j = 1 - \exp\left(-\tau \frac{R_j}{\tilde{R}_j}\right), \quad j = 1, \ldots, N \tag{2.26}$$

according to [86], where $\tilde{R}_j = \tilde{\lambda}_j(1-\zeta_j)$, $\forall j$, is the minimum tier-utility requirement (which also serves as a reference point for the satisfaction of tier-utility R_j), $\tilde{\lambda}_j$ is the corresponding minimum density requirement and τ is a factor indicating the steepness of the QoE curve. For instance, when the tier-utility R_j is greater than its reference value $\tilde{R}_j$, the QoE factor of the jth tier increases slowly. On the contrary, when R_j is lower than $\tilde{R}_j$, the QoE factor decreases dramatically. Considering the QoS requirements in both the maximum outage probability and the minimum transmission density, we formulate a weighted sum QoE maximization problem as

$$\text{(P2)}: \quad \max_{\boldsymbol{\lambda},\boldsymbol{\beta}} \sum_{j=1}^{N} \omega_j \left[1 - \exp\left(-\tau \frac{R_j}{\tilde{R}_j}\right)\right] \tag{2.27a}$$

$$\text{s.t.} \quad R_j = \lambda_j \pi_j \left[1 - \exp\left(-\frac{\beta_j \phi(\gamma^\star)}{\lambda_j}\right)\right] \tag{2.27b}$$

$$\tilde{\lambda}_j \le \lambda_j \le \frac{\beta_j \phi(\gamma^\star)}{\ln(1/\zeta_j)} \tag{2.27c}$$

$$\sum_{j=1}^{N} \beta_j = 1, \ 0 \le \beta_j \tag{2.27d}$$

where $\tilde{R}_j = \tilde{\lambda}_j(1-\zeta_j),\ \forall j$. We note that in (P2) we directly use $\gamma^\star = \arg\max \phi(\gamma)$ as the optimal resource partitioning between link 1 and link 2, since it maximizes not only the objective function but also the size of feasible regions of both $\boldsymbol{\lambda}$ and $\boldsymbol{\beta}$. To solve (P2), we have the following two propositions.

Proposition 1. *The solution of (P2) can be represented by*

$$\beta_j = \tilde{\beta}_j + \bar{\beta}_j \tag{2.28}$$

$$\lambda_j = \frac{\beta_j \phi(\gamma^\star)}{\ln(1/\zeta_j)} \tag{2.29}$$

where $\tilde{\beta}_j = \frac{\tilde{\lambda}_j \ln(1/\zeta_j)}{\phi(\gamma^\star)}$ *and* $\bar{\beta}_j$ *is the solution of*

$$\text{(P3)}: \quad \min_{\{\bar{\beta}_j\}} \sum_{j=1}^{N} \omega_j \exp\left(-\tau \frac{\bar{\beta}_j z_j \phi(\gamma^\star)}{\tilde{R}_j}\right) \tag{2.30a}$$

$$\text{s.t.} \quad \sum_{j=1}^{N} \bar{\beta}_j \leq \Delta\beta,\ 0 \leq \bar{\beta}_j \tag{2.30b}$$

where $\Delta\beta = 1 - \frac{\sum \tilde{\lambda}_j \ln(1/\zeta_j)}{\phi(\gamma^\star)}$.

Proof. To simplify (P2), we first recognize that the objective of (P2) monotonically increases with the increase of $\lambda_j,\ \forall j$. In addition, the λ_j has both upper and lower bounds shown in (2.27c), where the upper bound is linearly proportional to the resource ratio β_j and the lower bound is the minimum density constraint. Therefore, given a certain ratio β_j, the upper bound of MTCD density should be achieved. In other words, the optimal solution of (P2) should guarantee

$$\lambda_j = \frac{\beta_j \phi(\gamma^\star)}{\ln(1/\zeta_j)}. \tag{2.31}$$

Generally, these facts motivate us to solve (P2) with the following two steps:

1. allocating minimum resource to each tier to meet the minimum transmission density requirements,

2. maximizing the QoE with the residual resources.

Specifically, after replacing λ_j with $\frac{\beta_j \phi(\gamma^\star)}{\ln(1/\zeta_j)}$ according to (2.31), (P2) is simplified as

$$\min_{\boldsymbol{\beta}} \sum_{j=1}^{N} \omega_j \exp\left(-\tau \frac{\beta_j z_j \phi(\gamma^\star)}{\tilde{R}_j}\right) \tag{2.32a}$$

$$\text{s.t.} \ \ \tilde{\lambda}_j \leq \frac{\beta_j \phi(\gamma^\star)}{\ln(1/\zeta_j)} \tag{2.32b}$$

$$\sum_{j=1}^{N} \beta_j = 1, \ 0 \leq \beta_j. \tag{2.32c}$$

where $\tilde{R}_j = \tilde{\lambda}_j(1-\zeta_j)$. Next, we denote

$$\tilde{\beta}_j = \frac{\tilde{\lambda}_j \ln(1/\zeta_j)}{\phi(\gamma^\star)} \tag{2.33}$$

according to (2.32b), and

$$\Delta\beta = 1 - \sum_{j=1}^{N} \tilde{\beta}_j = 1 - \frac{\sum \tilde{\lambda}_j \ln(1/\zeta_j)}{\phi(\gamma^\star)} \geq 0. \tag{2.34}$$

We mention that $\Delta\beta \geq 0$ since $\sum_{j=1}^{N} \tilde{\beta}_j \leq 1$ as $\tilde{\beta}_j \leq \beta_j$ according to (2.32b) and (2.33).

Furthermore, we represent the original resource ratio β_j as $\beta_j = \tilde{\beta}_j + \bar{\beta}_j, \ \forall j$, where $\tilde{\beta}_j \geq 0$ indicates the minimum resource ratio allocated to tier-j to meet the minimum MTCD transmission density requirements and the $\bar{\beta}_j \geq 0$ is a new optimization variable representing the resource partitioning ratio for the residue amount of resource $\Delta\beta$ to tier-j. Replacing β_j with $\tilde{\beta}_j + \bar{\beta}_j$ in (2.32a) to (2.32c) and regarding $\bar{\beta}_j$ as a the optimization variable, the problem will be further simplified to (P3). $\square$

Proposition 2. *The solution to (P3) is*

$$\bar{\beta}_j = \left[-\frac{1}{\tau \bar{z}_j} \ln\left(\frac{\nu}{\omega_j \tau \bar{z}_j}\right)\right]^+ \tag{2.35}$$

with $\bar{z}_j = \frac{z_j \phi(\gamma^\star)}{\tilde{R}_j}$ *and* $\nu \geq 0$*, such that* $\sum_{j=1}^{N} \bar{\beta}_j = \Delta\beta$*.*

Proof. (P3) is recognized as a convex optimization problem. The Lagrangian function of (P3) is

$$L(\bar{\beta}_j, \nu) = \sum_{j=1}^{N} \omega_j \exp\left(-\tau \frac{\bar{\beta}_j z_j \phi(\gamma^\star)}{\tilde{R}_j}\right) + \nu \left(\sum_{j=1}^{N} \bar{\beta}_j - \Delta\beta\right). \tag{2.36}$$

The solution of (P3) is then represented as the solution to $\partial L(\bar{\beta}_j, \nu)/\partial \bar{\beta}_j = 0$ where β_j's are positive. By numerically searching for the proper value of ν such that $\sum_{j=1}^{N} \bar{\beta}_j = \Delta\beta$, the solution to (P3) is obtained. □

Substituting $\bar{z}_j = \frac{z_j \phi(\gamma^\star)}{\tilde{R}_j}$ and $z_j = \frac{\pi_j(1-\zeta_j)}{\ln(1/\zeta_j)}$ to (2.35), the solution $\bar{\beta}_j$ can be rewritten as

$$\bar{\beta}_j = \left[-\frac{\tilde{\lambda}_j \ln(1/\zeta_j)}{\pi_j \phi(\gamma^\star)\tau} \ln\left(\frac{\nu\tilde{\lambda}_j \ln(1/\zeta_j)}{\omega_j \pi_j \phi(\gamma^\star)\tau}\right)\right]^+. \tag{2.37}$$

In general, the monotonicity of $\bar{\beta}_j$ over the minimum density requirement $\tilde{\lambda}_j$ and the maximum outage probability constraint ζ_j is not clear without the knowledge of other parameters such as ν, $\phi(\gamma^\star)$, ω_j, π_j and τ.

2.4.2 Numerical Results

In the simulation, we assume there are two tiers of MTCDs and compare the QoE, the network throughput, the achievable MTCD density and the resource allocation ratio under different outage probability constraints $\zeta_j \in [0.002, 0.3]$, $\forall j$ and the same minimum MTCD density constraint $\tilde{\lambda}_j = 0.08$, $\forall j$. Without loss of generality, we assume $\phi(\gamma^\star) = 1$, $\tau = 1$, $\pi_j = 1$ and $\omega_j = 1$, $\forall j$. In particular, the sum QoEs for different outage probability constraints are shown in Fig.2.7, from which we notice that the sum QoE increases with the growth of both ζ_1 and ζ_2. We can also see that the sum QoE increases more rapidly when both ζ_1 and ζ_2 are relatively small, which indicates the QoE is more sensitive to stringent outage probability constraints. A similar trend can be seen in Fig. 2.8 where the QoE of the tier-1 MTCD is shown. We also observe from Fig. 2.8 that ζ_1 has a more noticeable effect on the QoE of tier-1 than ζ_2 does. Next, Fig. 2.9 and Fig. 2.10 show the throughput

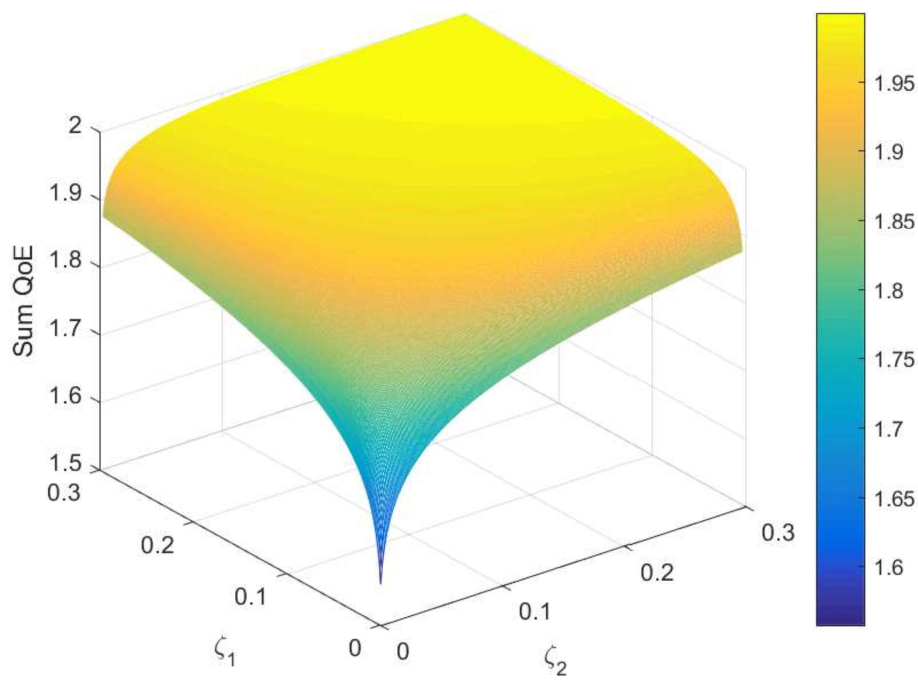

Figure 2.7: Sum QoE under different outage probability constraints.

and the corresponding MTCD density of the tier-1. In line with the relationship between the QoE and outage probability constraints, the throughput and the MTCD density increase with the growth of ζ_1 and ζ_2. Finally, the resource allocation ratio is shown in Fig. 2.11. In contrast to the resource allocation solutions to the network utility maximization problem we discussed in section III, we notice that to maximize the sum QoE, more resources are allocated to the tier with more stringent constraint. For instance, when ζ_1 is around zero and $\zeta_2 = 0.3$, the resource ratio for tier-1 is more than 0.7 as Fig.2.11 shows. This fact indicates that to achieve a satisfiable QoE under very stringent constraint, a relatively high resource ratio must be guaranteed.

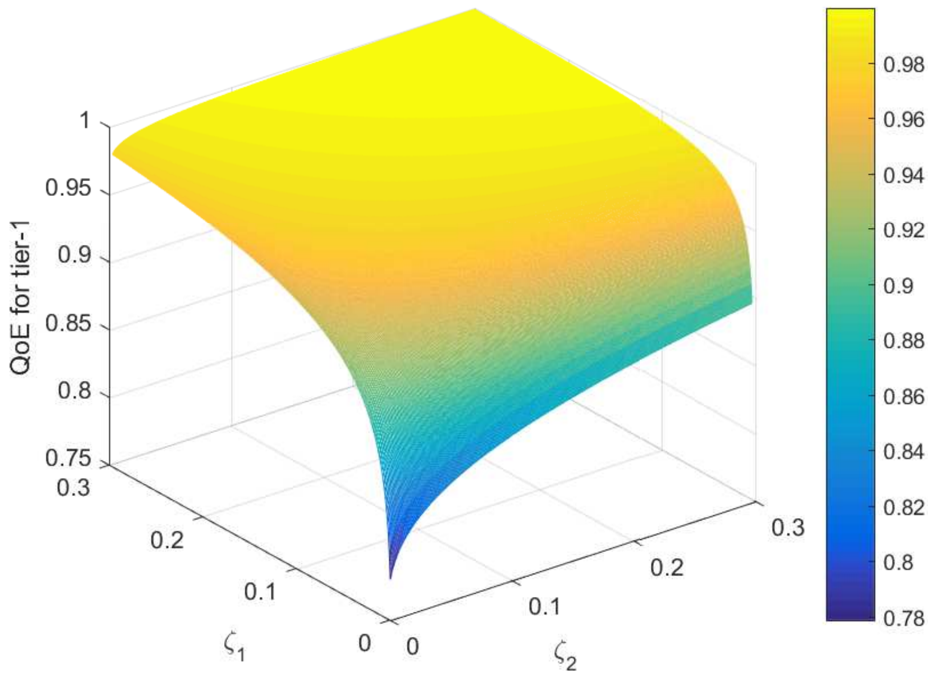

Figure 2.8: QoE of tier-1 under different outage probability constraints.

2.5 MTCG uplink power control

In the proposed MTC scheme, the successful relaying of a MTCD packet captured by a MTCG depends on two factors: 1) the amount of packets captured by the MTCG and 2) the available channels for the MTCG. We assume that an MTCG needs one channel to relay one packet so that when the amount of packets captured by a MTCG is larger than the total number of channels allocated to it, certain packets will be randomly dropped. Since the MTCDs are assumed always in active transmission mode with certain density and each packet is of the same length, the MTCG-to-BS links need to keep a constant data rate. We assume the BS locations form a PPP with density λ_B independent of the MTCG locations and each MTCG only transmits to its nearest BS. We represent the MTCG location in a two dimensional coordinate as x. Since we assume that the transmissions between MTCGs and the BS encounters both Rayleigh fading and the exponential path

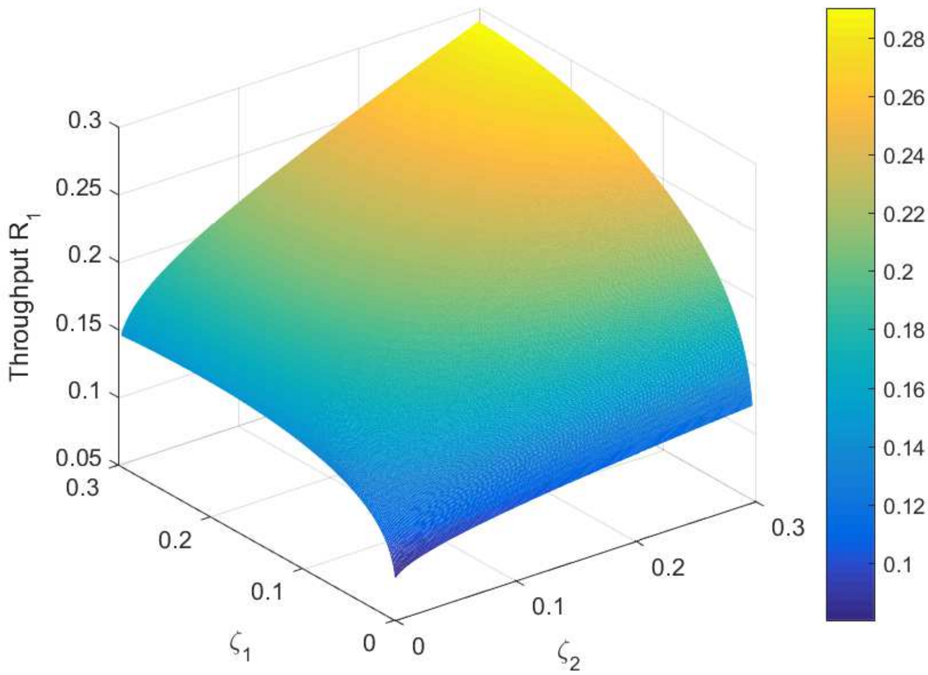

Figure 2.9: Throughput of tier-1 under different outage probability constraints.

loss, a strictly constant data rate can hardly be achieved as the random fading could be significantly deep. Alternatively, we consider to keep a constant outage capacity (spectral efficiency) with truncated channel inversion policy[19]. We denote P_x as the transmit power of a MTCG located at x, h_x and r_x as the fading power gain and the distance between the MTCG located at x and the target BS respectively. Let $L(r_x) = r_x^{-\alpha}$ represents the path loss, σ^2 to be the noise power on a MTCG-to-BS channel, and $\mathbb{P}_{\text{out}}$ to be the outage probability defined as the probability that the overall channel power gain (including both fading and path loss) is less than a certain threshold. The outage capacity (spectral efficiency) is represented as

$$C = \log_2\left(1 + \frac{h_x L(r_x) P_x}{\sigma^2}\right)(1 - \mathbb{P}_{\text{out}}), \ \forall x. \tag{2.38}$$

Recalling that we assume each MTCG has $U_2 = \lfloor Q_2/(G\delta_2) \rfloor$ channels, where $Q_2 = (1 - \gamma)Q_M$ is the number of RBs allocated for all MTCG-to-BS links, G is the number of MTCGs

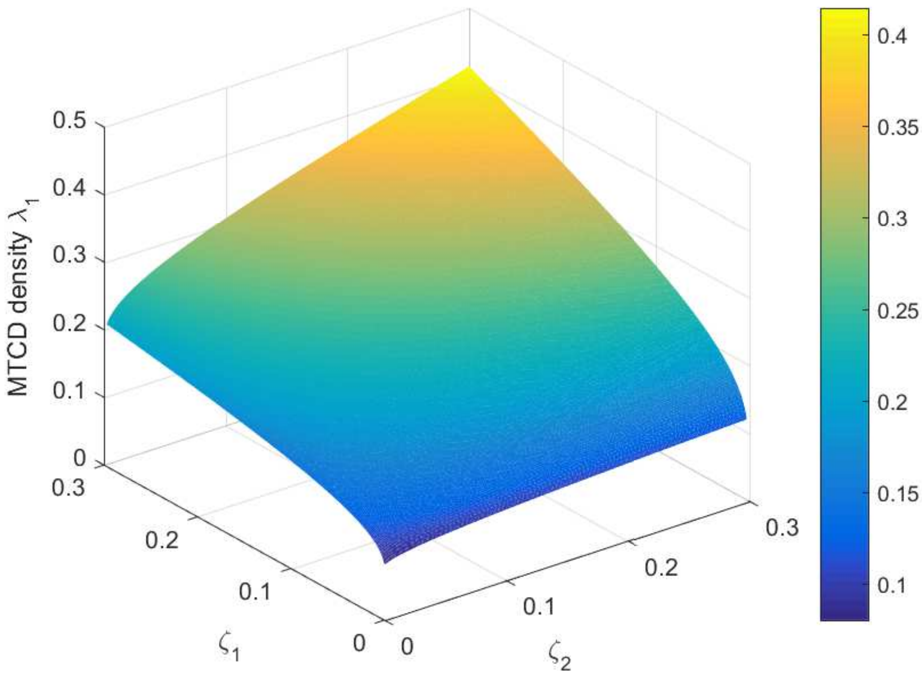

Figure 2.10: Allowable MTCD density of tier-1 under different outage probability constraints.

and δ_2 is the number of RBs needed for an MTCG to relay a packet. In general, a higher spectral efficiency indicates a larger number of MTCG-to-BS channels U_2 given the same amount of RBs and the same data rate requirement for each MTCG packet transmission. This fact connects the spectral efficiency in (2.38) to parameter $\phi(\gamma)$ in (2.6) with a common factor U_2. Thus, the network dimensioning and resource allocation problems discussed in previous sections are affected by the spectral efficiency via $\phi(\gamma)$. In particular, we can adapt the definition of U_2 as $\tilde{U}_2 = \left\lfloor \frac{Q_2 C \chi_1}{G \delta_2 \chi_2} \right\rfloor$ (i.e., in this section, we use the adapted definition $\tilde{U}_2$ as a replacement of U_2), where χ_1 (Hz/RB) is the bandwidth per RB, χ_2 (bps/RB) is the required data rate per RB and $G = \pi\rho^2\lambda_G$ is the average number of MTCGs within the region $B(\mathbf{0}, \rho)$. Thus, the numerator $Q_2 C \chi_1$ is the aggregated MTCG-to-BS data rate and the term $\delta_2 \chi_2$ indicates the required data rate to transmit one packet on a MTCG-to-BS channel for each MTCG. Then, since $\phi(\gamma)$ defined in (2.6) is a function of both γ and U_2 ($\tilde{U}_2$),

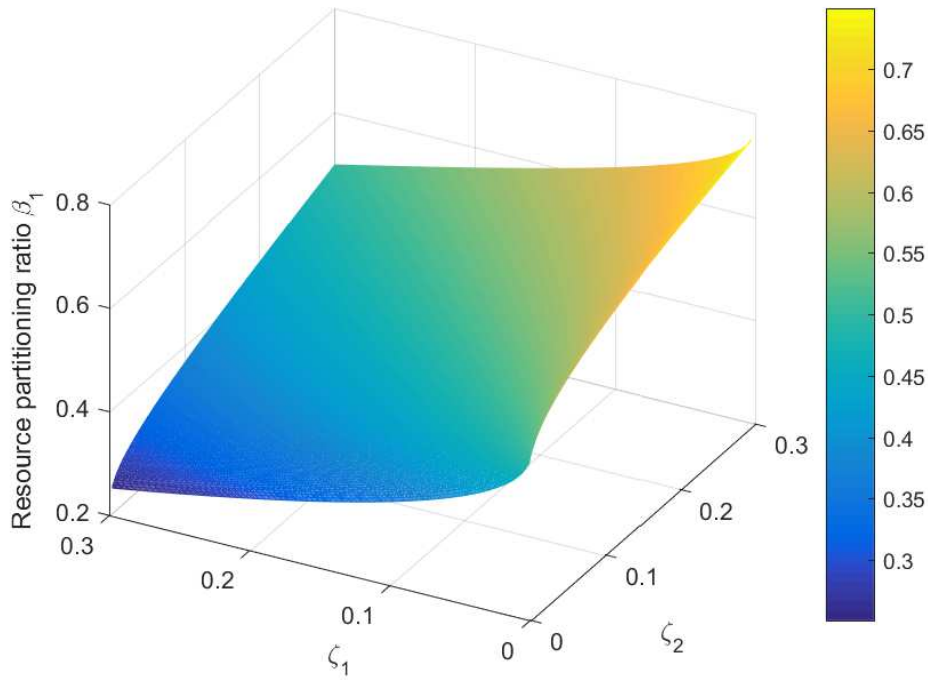

Figure 2.11: Resource allocation ratio of tier-1 under different outage probability constraints.

the optimal resource partitioning $\gamma^{\star}$ between link 1 and link 2 can be numerically computed given the MTCG-to-BS spectral efficiency C.

Provided that the channel state information (CSI) and the distance between the MTCG and BS are known to the transmitting MTCG but the average aggregated transmit power for the MTCGs is bounded, we propose a power allocation strategy for any MTCG within the coverage of the BS to realize the constant outage capacity. Remember that the BS locations and the MTCG locations form independent homogeneous spatial PPPs within $B(\mathbf{0}, \rho)$ with density λ_B and λ_G respectively. Similar to the MTCD-to-MTCG channel, we assume i.i.d. Rayleigh fading with average power gain of μ on each MTCG-to-BS channel, and path loss with exponent α over all channels. In order to maintain a constant transmission rate, each MTCG applies truncated channel inversion to adapt its transmit power. Specifically, two power control strategies based on truncated channel inversion are considered. The two strategies compensate for both fading and path loss but they differ in the criteria of when the compensation is performed. In the first proposed strategy (S1), the MTCG transmits only if the overall channel power gain (including both fading and path loss) is above a certain threshold. The second strategy (S2) allows MTCG to transmit only if the fading gain is above a certain threshold, and it is a baseline strategy proposed to compare with the first one. The expressions of the transmit power for both strategies are represented as

$$\text{(S1)}: \; P_x = \begin{cases} \frac{\bar{P}}{h_x L(r_x)}, & h_x L(r_x) \geq \tilde{h} \\ 0, & \text{otherwise} \end{cases} \tag{2.39}$$

$$\text{(S2)}: \; P_x = \begin{cases} \frac{\bar{P}}{h_x L(r_x)}, & h_x \geq h \\ 0, & \text{otherwise} \end{cases} \tag{2.40}$$

where $\bar{P}$ is the constant BS received signal power and $\tilde{h}$ and h are the thresholds of channel inversion for (S1) and (S2) respectively. Given an aggregated power constraint P_{sum}, we are interested in finding proper values of $\bar{P}$, $\tilde{h}$ and h so that the outage capacity of each MTCG-to-BS link is maximized. Therefore, the problem is formulated as

$$\text{(P4)}: \; \max_{g} \quad \log_2\left(1 + \frac{\bar{P}}{\sigma^2}\right) \mathbb{P}\left(g_x \geq g\right) \tag{2.41a}$$

$$\text{s.t.} \quad \mathbb{E}\left[\sum_{x\in\Phi_G, x\in B(\mathbf{0},\rho)} P_x\right] = P_{\text{sum}} \tag{2.41b}$$

$$P_x = \begin{cases} \frac{\bar{P}}{h_x L(r_x)}, & g_x \geq g \\ 0, & \text{otherwise} \end{cases} \tag{2.41c}$$

where $g_x = h_x L(r_x)$, $g = \tilde{h}$ when applying (S1) and $g_x = h_x$, $g = h$ for (S2). The objective function (2.41a) is obtained by substituting P_x to (2.38), while (2.41b) and (2.41c) represent the aggregated transmit power constraint and the power control strategy.

To solve (P4), both the distribution of g_x and the expectation of the aggregated MTCG transmit power, i.e., the left hand side of (2.41b) should be properly represented, in order to obtain the success probability $\mathbb{P}(g_x \geq g)$ and the received power $\bar{P}$. In the following of this section, both issues will be discussed.

2.5.1 Development of Outage Probability

Since the MTCGs only choose the closest BS to transmit, the BS's form Poisson Voronoi tessellations and each BS only receives the signals from the MTCGs within its Voronoi cell. In this case, the PDF of the distance r_x between a MTCG located at x and the corresponding BS is [4]

$$f_{r_x}(r) = 2\pi\lambda_B r e^{-\pi\lambda_B r^2}, \quad r \geq 0. \tag{2.42}$$

On the other hand, given the distance r_x, the conditional cumulative density function (CDF) of g_x can be written as

$$F_{g_x|r_x}(g) = 1 - \exp\left(-\frac{\mu g}{L(r_x)}\right), \; g \geq 0 \tag{2.43}$$

for the first strategy (S1).

Deconditioning (2.43) with the PDFs of r_x, the CDF of g_x is obtained as

$$F_{g_x}(g) = \int_0^{\rho} F_{g_x|r}(g) f_{r_x}(r) dr = 1 - 2\pi\lambda_B \int_0^{\infty} e^{-\frac{\mu g}{L(r)} - \pi\lambda_B r^2} r dr. \tag{2.44}$$

for the first strategy (S1). For the baseline strategy (S2), the CDF of g_x is

$$F_{g_x}(g) = 1 - \exp(-\mu g) \tag{2.45}$$

since $g_x = h \sim \exp(1/\mu)$.

Thus, the successful transmission probability in (2.41a) can be represented as

$$\mathbb{P}(g_x > g) = \begin{cases} 2\pi\lambda_B \int_0^{\infty} e^{-\frac{\mu g}{L(r)} - \pi\lambda_B r^2} r dr, & \text{for (S1)} \\ \exp(-\mu g), & \text{for (S2)}. \end{cases} \tag{2.46}$$

2.5.2 Development of Aggregated Transmit Power

To achieve a constant uplink transmission data rate, each MTCG varies its transmit power according to its location and the fading gain of the channels. For the first strategy (S1), given a truncated threshold $g = \tilde{h}$, the aggregated MTCG transmit power within $B(\mathbf{0}, \rho)$ is developed as

$$\begin{aligned}\mathbb{E}_{\{\Phi_G\}}\left[\sum_{x\in\Phi_G\cap B(\mathbf{0},\rho)} P_x\right] &= \mathbb{E}_{\{\Phi_G\}}\left\{\mathbb{E}_{\{h_x,r_x\}}\left[\sum_{x\in\Phi_G\cap B(\mathbf{0},\rho),\ h_x\ge\tilde{h}/L(r_x)} \frac{\bar{P}}{h_x L(r_x)}\right]\right\}\\ &\overset{(a)}{=} \mathbb{E}_{\{\Phi_G\}}\left\{\sum_{x\in\Phi_G\cap B(\mathbf{0},\rho)} \mathbb{E}_{\{r_x\}}\left[\frac{\bar{P}}{L(r_x)}\left(-\mu\mathrm{Ei}\left(-\frac{\mu\tilde{h}}{L(r_x)}\right)\right)\right]\right\}\\ &\overset{(b)}{=} \mathbb{E}_{\{\Phi_G\}}\left\{\sum_{x\in\Phi_G\cap B(\mathbf{0},\rho)} \int_0^\infty \frac{\bar{P}}{L(r)}\left[-\mu\mathrm{Ei}\left(-\frac{\mu\tilde{h}}{L(r)}\right)\right] f_{r_x}(r)dr\right\}\\ &\overset{(c)}{=} -2\pi^2\rho^2\lambda_B\lambda_G\mu\bar{P}\int_0^\rho \frac{r}{L(r)}\mathrm{Ei}\left(-\frac{\mu\tilde{h}}{L(r)}\right) e^{-\pi\lambda_B r^2}dr\end{aligned} \tag{2.47}$$

where $\mathrm{Ei}(x) = \int_{-x}^{\infty} \frac{1}{t}e^{-t}dt$ is the incomplete exponential integral function, (a) follows from deriving the expectation of $1/h_x$ conditioning on $h_x \geq g/L(r_x)$ and (b) holds because the set of distances $\{r_x\}$ is mutually independent. Then (c) follows from the Campbell's theorem [23]. Similarly, for the baseline strategy (S2), we have

$$\begin{aligned}\mathbb{E}\left\{\sum_{x\in\Phi_G\cap B(\mathbf{0},\rho)} P_x\right\} &= \mathbb{E}_{\{\Phi_G\}}\left\{\mathbb{E}_{\{h_x,r_x\}}\left[\sum_{x\in\Phi_G\cap B(\mathbf{0},\rho),\ h_x\ge h} \frac{\bar{P}}{h_x L(r_x)}\right]\right\}\\ &= -2\pi^2\rho^2\lambda_B\lambda_G\mu\bar{P}\int_0^\rho \frac{\mathrm{Ei}(-\mu h)}{L(r)} e^{-\pi\lambda_B r^2} r dr.\end{aligned} \tag{2.48}$$

Thus, given the average aggregated MTCG power constraint P_{sum}, the received constant signal power $\bar{P}$ at the BS is

$$\bar{P} = \begin{cases} -P_{\text{sum}}\left[2\pi^2\rho^2\lambda_B\lambda_G\mu\int_0^\rho \frac{r}{L(r)}\mathrm{Ei}\left(-\frac{\mu\tilde{h}}{L(r)}\right)e^{-\pi\lambda_B r^2}dr\right]^{-1}, & \text{for (S1)}\\ -P_{\text{sum}}\left[2\pi^2\rho^2\lambda_B\lambda_G\mu\int_0^\rho \frac{r}{L(r)}\mathrm{Ei}(-\mu h)e^{-\pi\lambda_B r^2}dr\right]^{-1}, & \text{for (S2).}\end{cases} \tag{2.49}$$

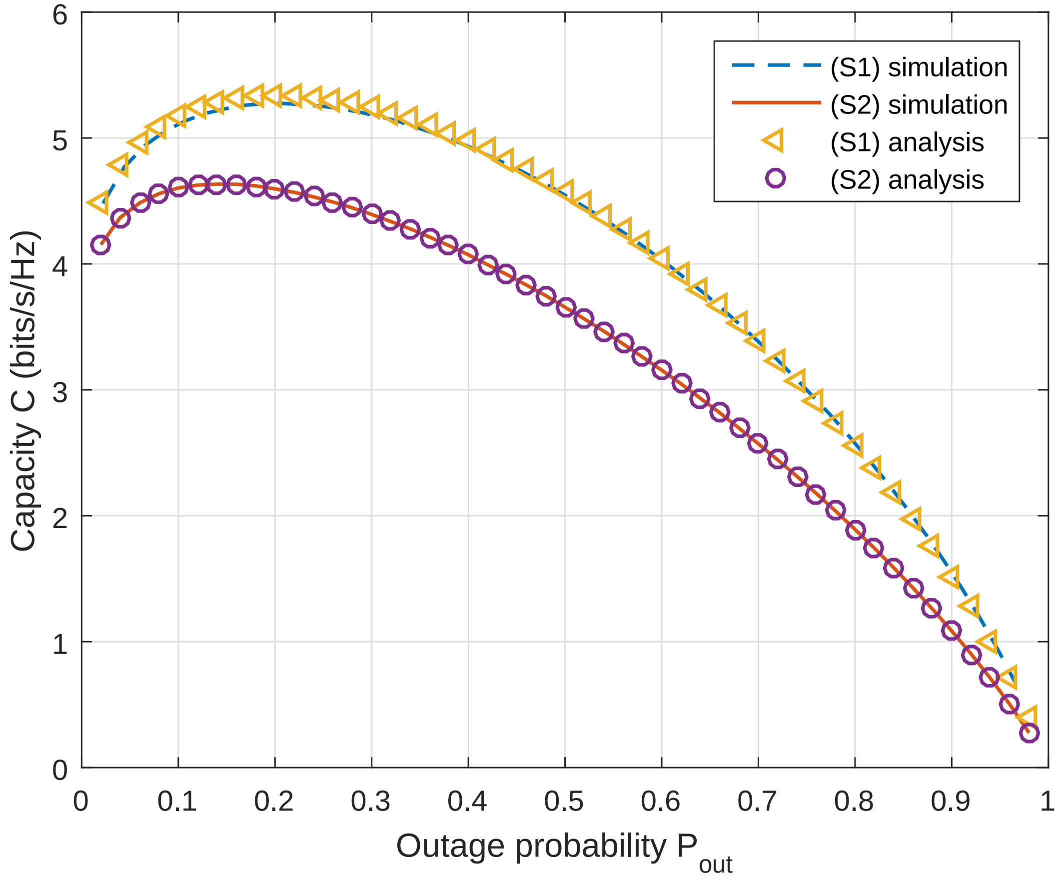

Figure 2.12: Comparison of outage capacities at different outage probabilities. (P_{sum} = 65 dBW)

Therefore, with (2.46) and (2.49), the objective function (2.41a) can be maximized by numerically searching for the optimal threshold $\tilde{h}$ for (S1) or h for (S2).

2.5.3 Numerical Results and Discussions

In the simulation, we use the following default settings for Fig. 2.12 - Fig. 2.14, $\rho = 100$, $\lambda_B = 0.008$, $\lambda_G = 0.005$, $\alpha = 3$, $\sigma^2 = 1$ and $\mu = 1$. Other specific settings are mentioned below the corresponding figures. Fig. 2.12 compares our proposed MTCG power control strategy (S1) and the baseline strategy (S2) in terms of the achievable outage capacity

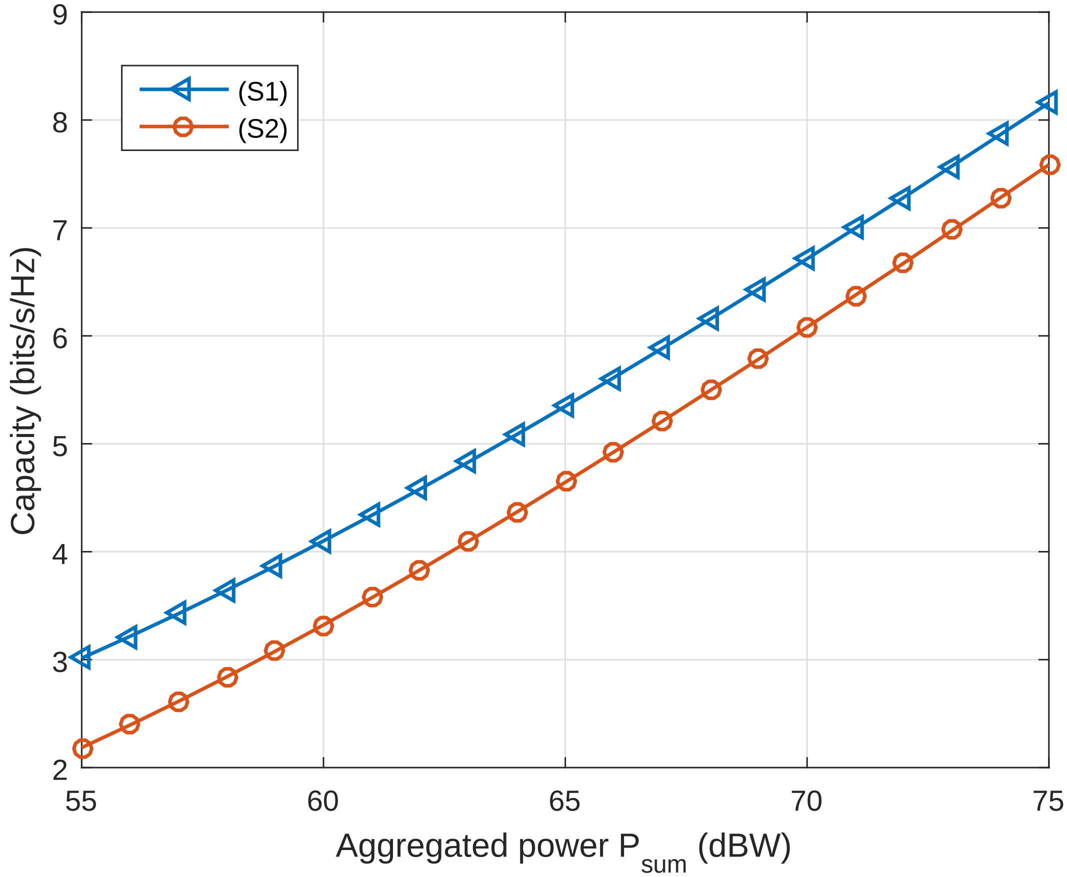

Figure 2.13: Comparison of outage capacities at different aggregated power levels.

under different outage probabilities. It can be observed that the (S1) outperforms (S2) for all possible outage probabilities and that the outage probability of (S1) is slightly larger than the outage probability of (S2) when maximum outage capacity is achieved. For instance, (S1) achieves the maximum capacity when $P_{\text{out}} = 0.20$, while the maximum capacity of (S2) is obtained when $P_{\text{out}} = 0.14$. Next, Fig. 2.13 shows that (S1) achieves higher outage capacity than that of (S2) for different aggregated powers. We also notice that the difference between the two capacities is proportionally more obvious when the aggregated power is small, which indicates that (S1) can allocate power more efficiently in a power-limit condition.

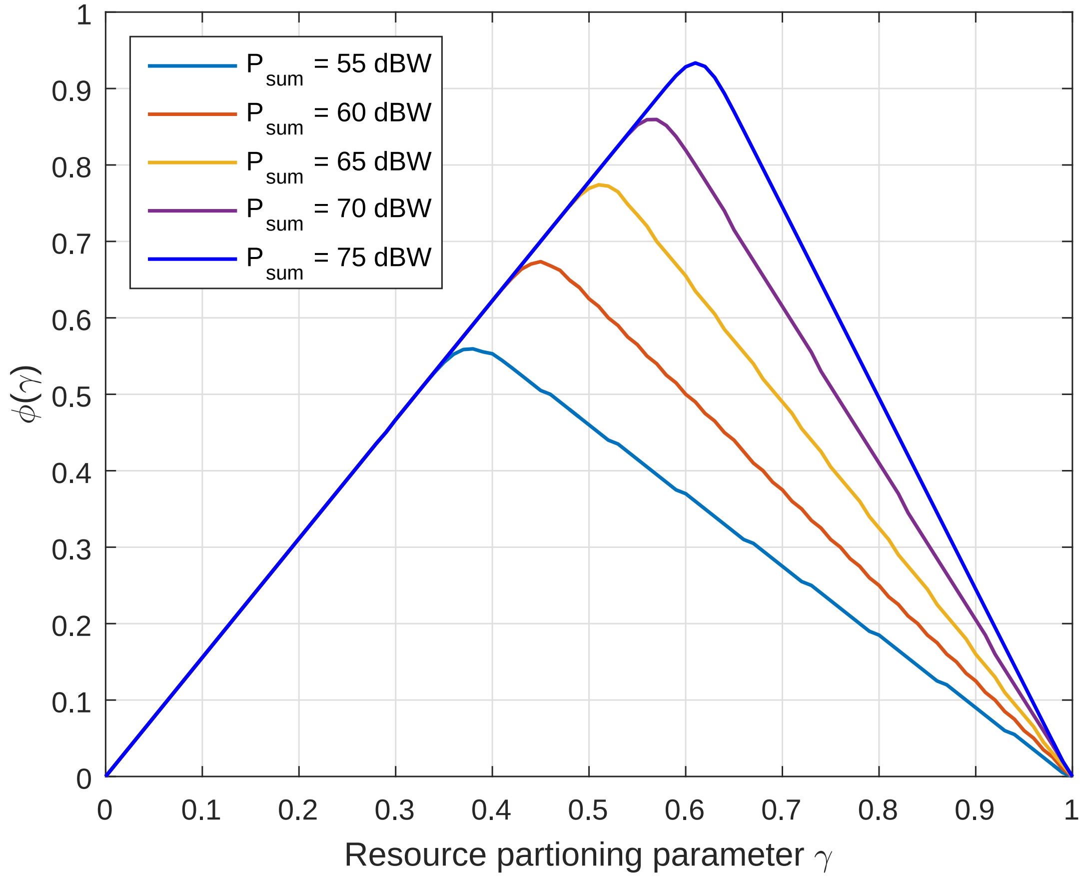

Figure 2.14: Comparison of $\phi(\gamma)$ at different γ and aggregated power levels using (S1). ($Q_M = 48000,\ \delta_1 = 30,\ \delta_2 = 5,\ \eta = 3,\ \chi_1/\chi_2 = 1$)

With strategy (S1), the effect of aggregated power constraints on the resource partitioning between MTCGs and MTCDs is shown in Fig, 2.14, where the values of $\phi(\gamma)$ are compared. In Fig. 2.14, we can see that a greater aggregated power results in a larger $\phi(\gamma^\star)$. Additionally, a greater aggregated power also corresponds to a greater $\gamma^\star$. Since the spectral efficiency of the MTCG-to-BS link increases with P_{sum} and if the MTCG-to-BS links have higher spectral efficiency, more resources can be allocated the MTCD-to-MTCG links (i.e., $\gamma^\star$ will be greater).

2.6 Conclusion

We proposed network dimensioning and resource allocation approaches for the multi-tier MTC data aggregation scheme to trade off between the network utility and the fair resource allocation. First, we analyzed three specific scenarios of resource partitioning by means of the utility-optimal method, the GM-based method, and the CS-based method, under maximum transmission outage probability constraints. Then, we developed a generalized resource partitioning for various levels of fairness. Next, considering both the maximum outage probability constraint and the minimum MTCD density requirements, we investigated the overall QoE maximization problem. In contrast to the resource allocation solution to the network utility maximization problem, we found it is preferable to allocate more resource to the tier with more stringent outage probability constraint. Finally, we investigated two different truncated channel inversion power control strategies (S1 and S2) for the MTCG. Our proposed strategy (S1) outperforms the baseline strategy (S2) in terms of achievable outage capacity since it takes both the randomnesses of location and the fading factor into account.

CHAPTER 3

COVERAGE PROBABILITY ANALYSIS UNDER CLUSTERED AMBIENT BACKSCATTER NODES

3.1 Introduction

This chapter investigates the coverage probability of a AmBC-embedded wireless communication network. Recent studies about AmBC mainly focus on the signal detection perspective and most of them consider a single BT-BR pair and a primary transmitter (PT, which emits the ambient RF signal) although multiple antennas are involved[83, 77, 61]. Concerning the rapid growth of IoT devices, we believe investigating the scalability of AmBC is also a crucial issue. Thus, this chapter considers to include the AmBC nodes in conventional large-scale wireless communication networks, resulting in a heterogeneous network (HetNet).

Stochastic geometry based approaches have been realized to be efficient and tractable for analyzing complex HetNets [16]. With some assumptions to the distribution (such as Poisson point process (PPP)) of the node locations, the system performance of a HetNet can be expressed by quickly computable integrals with a small number of parameters [4]. Recent studies have found that simply using a PPP based geometric model is not rich enough to analyze the increasingly complex HetNet, yet the Poisson cluster process (PCP) based analysis is more capable [66].

So far, most analyses on large-scale backscatter communication networks are about WPBC networks [27, 37, 60]. For instance, [27] proposed a large-scale WPBC network and derived the network coverage probability and capacity. A hybrid transmission scheme that integrates AmBC and wireless powered communications was proposed in [48]. The achievable rate region for a single-tag backscatter multiple-access channel was derived in [44].

However, to the best of our knowledge, none of the existing studies have considered to apply a PCP model to an AmBC system, of which the analysis is different from those proposed in the references. Specifically, in an existing large-scale wireless network, newly deployed AmBC nodes will change the effective channel response between a PT and a primary receiver (PR). In this scenario, the backscattered signals can be regarded as either decodable signals or interference at a typical PR, which will affect the coverage probability of a typical PT. Therefore, we derive an analysis of the signal-to-interference-plus-noise ratio (SINR) and signal-to-interference ratio (SIR) based coverage probability at a typical PR.

This chapter is organized as follows. The system model and signal representations are described in Section 3.2. Then, we derive the coverage probabilities in Section 3.3. Numerical simulation results and conclusions are provided in Section 3.4 and Section 3.5, respectively.

3.2 System Model

3.2.1 Spatial Distribution Models

The system we consider consists of two tiers (layers), where the first tier includes all the PTs and PRs, and the second tier includes all the BTs and BRs. Under such system, we study two BT deployment scenarios. For scenario-1, each PT is surrounded by a cluster of BTs, shown in Fig. 3.1. For scenario-2, only the typical PT is surrounded by a cluster of BTs. Since the SINR and SIR based coverage probability derivations of both scenarios are similar, we mainly focus on the SINR-based derivation of scenario-1 in the following. Without loss of generality, we set a typical PR at the origin and its corresponding PT (i.e., the closest PT to the typical PR) at coordinate $Y_0 = (r_0, 0)$[1]. The locations of other PTs which cause interference to the typical PR form a PPP $\Phi_{\mathrm{P}} = \{Y_j\}$, where $Y_j \in \mathbb{R}^2,\ j = 1, 2, \ldots, M$,

[1]For a homogeneous PPP with density λ, the distance between an arbitrary (typical) point and its closest point is Rayleigh distributed with the scale parameter $1/\sqrt{2\pi\lambda}$ [4]. Thus, coverage probabilities based on a fixed distance r_0 can be extended to a general coverage probability by de-conditioning them with the distribution of r_0.

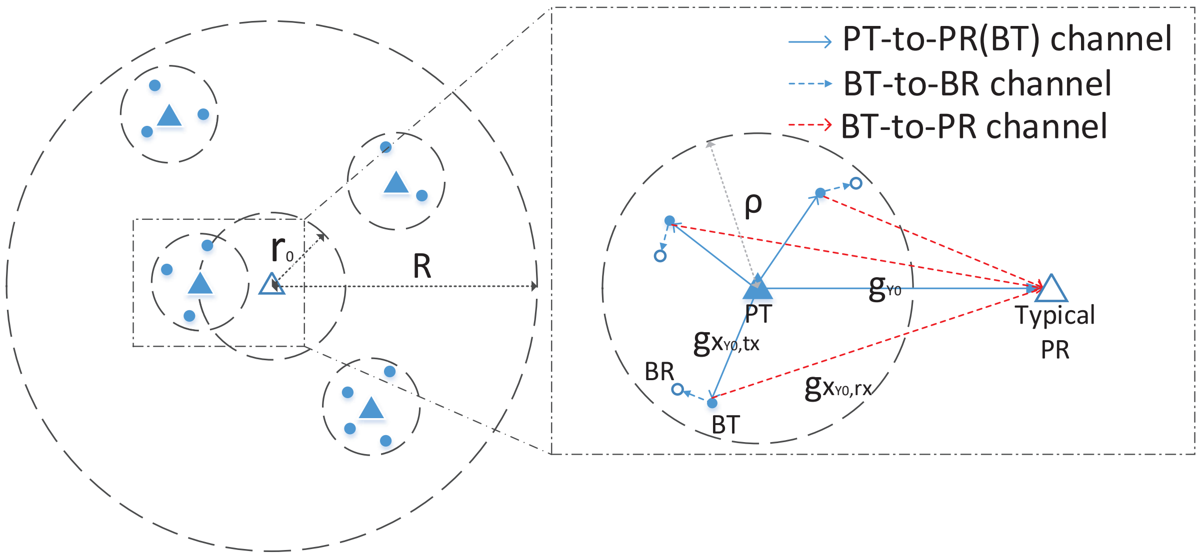

Figure 3.1: Topology of the considered system (scenario-1)

represents the coordinate of the jth PT, with a constant density λ_{P} in the ring-shape region $B(\mathbf{0}, R) - B(\mathbf{0}, r_0)$. The locations of the BTs[2] form a Matérn cluster process[1] represented by $\bigcap_{j=0}^{M} \Phi_{\mathrm{B}}(Y_j)$ in scenario-1 (where $\Phi_{\mathrm{B}}(Y_j) = \{X_{Y_j}\}$, with $X_{Y_j} \in \mathbb{R}^2$ representing the coordinate of a BT in the disk $B(Y_j, \rho)$) and a PPP represented by $\Phi_{\mathrm{B}}(Y_0)$ in scenario-2. For a compact expression, the distance between a PT at Y and the typical PR at the origin is denoted by r_Y. Similarly, we use $r_{X_Y,\mathrm{tx}}$ ($r_{X_Y,\mathrm{rx}}$) to represent the distance between the PT at Y (the typical PR at the origin) and the offspring BT at X_Y.

In addition, we assume that the density of PTs is much smaller than the BTs' density, i.e., $\lambda_{\mathrm{P}} \ll \lambda_{\mathrm{B}}$, such that the distances between BTs and their non-parent PTs are relatively large in average sense, resulting in much severer path losses than those between BTs and their parent PTs. Thus, we further assume that the information signals sent from the parent PT is the only RF power source of its offspring BTs and leave the analysis of multiple power sources for future study.

[2]The distribution of BRs is not considered since it does not affect the coverage probability.

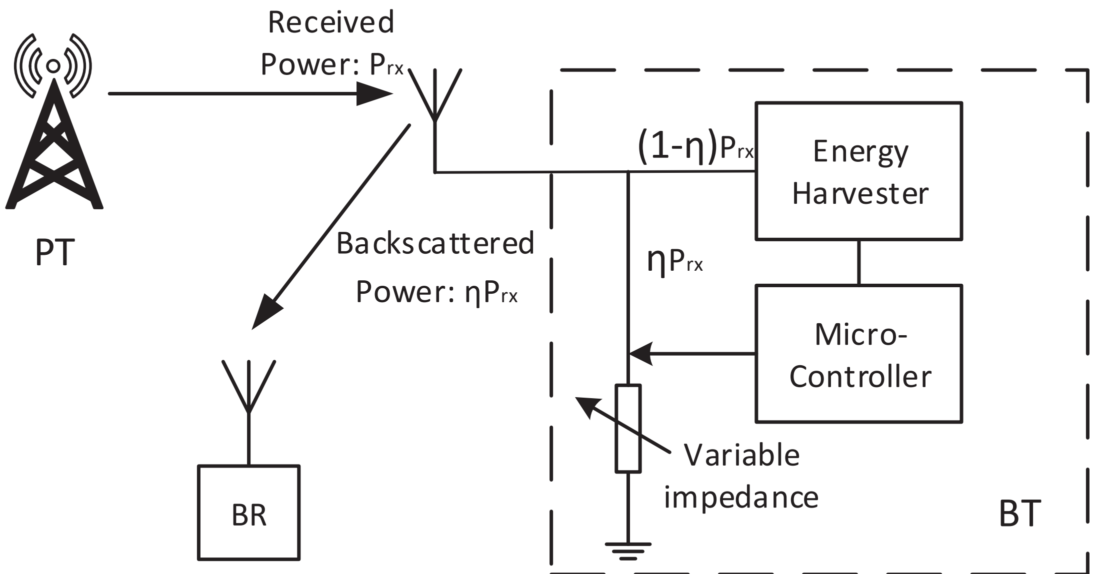

Figure 3.2: Ambient backscatter scheme

3.2.2 Signal Communication Model

We denote the transmit symbol of the PT located at Y at time t by $\sqrt{P_{\text{tx}}}s_Y(t)$, where P_{tx} is the constant transmit power and $s_Y(t) \sim \mathcal{CN}(0,1)$ is the normalized complex Gaussian distributed symbol. The backscatter symbol of the BT located at X_Y at time t is denoted by $b_{X_Y}(t)$. Since a BT only reflects the ambient signal using two impedance levels, we assume that the BTs' symbols are independent and Bernoulli-distributed with equal probability, i.e., $b_{X_Y}(t) \sim \text{Bernoulli}\left(\frac{1}{2}\right)$, $\forall X_Y$. As shown in Fig. 3.2, the reflection coefficient is $\eta \in [0,1]$, which means ηP_{rx} of the received power P_{rx} is backscattered by the BT and $(1-\eta)P_{\text{rx}}$ of the power is harvested by the BT for modulation and control purpose. Besides, we simply assume backlogged transmissions for both tiers so that the BTs and BRs can always be active based on the harvested energy. The AmBC throughput maximization problem regarding to mode switching policy has been investigated in [79].

Furthermore, we assume independent and identically distributed (i.i.d.) Rayleigh fading with average power gain of $1/\mu$ and path loss with exponent α over all channels. In particular, suppose the Rayleigh fading channel power gains between the PT at Y and the typical PR at the origin, the PT at Y and the BT at X_Y, and the BT at X_Y and the typical PR are g_Y, $g_{X_Y,\mathrm{tx}}$ and $g_{X_Y,\mathrm{rx}}$, respectively, each with exponential distribution with parameter μ, denoted by $\exp(\mu)$. Then, the channel response can be written as $h_Y = \sqrt{g_Y} e^{j\theta_Y}$, $h_{X_Y,\mathrm{tx}} = \sqrt{g_{X_Y,\mathrm{tx}}} e^{j\theta_{X_Y,\mathrm{tx}}}$ and $h_{X_Y,\mathrm{rx}} = \sqrt{g_{X_Y,\mathrm{rx}}} e^{j\theta_{X_Y,\mathrm{rx}}}$, respectively, each with zero-mean-complex-Gaussian distribution, where θ_Y, $\theta_{X_Y,\mathrm{tx}}$ and $\theta_{X_Y,\mathrm{rx}}$ represent the zero-mean uniformly distributed channel phases. To avoid the singularity at the origin, the path loss is expressed as $L(r) = (1 + r^\alpha)^{-1}$ for a distance r. Thus, we denote the received signal at the typical PR as the summation of several signals:

$$y(t) = s_{\mathrm{PT}}(t) + s_{\mathrm{BT}}(t) + I_{\mathrm{PT}}(t) + I_{\mathrm{BT}}(t) + n(t) \tag{3.1}$$

where $n(t) \sim \mathcal{CN}(0, \sigma^2)$ is the complex Gaussian noise at PR, $s_{\mathrm{PT}}(t)$, $s_{\mathrm{BT}}(t)$, $I_{\mathrm{PT}}(t)$, and $I_{\mathrm{BT}}(t)$ represent the signals from the typical PT at Y_0, from the offspring BTs of the typical PT, from the atypical PTs, and from the offspring BTs of the atypical PTs, respectively. Particularly, we have

$$s_{\mathrm{PT}}(t) = h_{Y_0} \sqrt{L(r_0) P_{\mathrm{tx}}}\, s_{Y_0}(t - \tau_{Y_0}), \tag{3.2}$$

$$s_{\mathrm{BT}}(t) = \sum_{X_{Y_0} \in \Phi_{\mathrm{B}}(Y_0)} z_{X_{Y_0}} \sqrt{\eta P_{\mathrm{tx}}}\, s_{Y_0}(t - \tau_{X_{Y_0}}) b_{X_{Y_0}} \tag{3.3}$$

$$I_{\mathrm{PT}}(t) = \sum_{Y \in \Phi_{\mathrm{P}}} h_Y \sqrt{L(r_Y) P_{\mathrm{tx}}}\, s_Y(t - \tau_Y), \tag{3.4}$$

$$I_{\mathrm{BT}}(t) = \sum_{Y \in \Phi_{\mathrm{P}}} \sum_{X_Y \in \Phi_{\mathrm{B}}(Y)} z_{X_Y} \sqrt{\eta P_{\mathrm{tx}}}\, s_Y(t - \tau_{X_Y}) b_{X_Y} \tag{3.5}$$

where $z_{X_Y} \triangleq h_{X_Y,\mathrm{tx}} h_{X_Y,\mathrm{rx}} \sqrt{L(r_{X_Y,\mathrm{tx}}) L(r_{X_Y,\mathrm{rx}})}$, τ_Y and τ_{X_Y} are the time delays of the PT to PR path (direct path) and the PT-BT-PR path (backscatter path), respectively, and the subscripts Y and X_Y indicate the locations of the PT and BT. We note that since the backscatter symbol $b_{X_Y}(t)$ has a much larger symbol duration than the primary symbol $s_Y(t)$ (i.e., $b_{X_Y}(t)$ is constant in many successive symbols of $s_Y(t)$) [43], the time index of and the time delay encountered by $b_{X_Y}(t)$ are neglected.

3.3 Analysis of Coverage Probability

3.3.1 Signal and Interference Power

For a compact expression, we use vectors $\boldsymbol{z}_Y = [\ldots, z_{X_Y}, \ldots]^{\mathrm{T}}$ and $\boldsymbol{b}_Y = [\ldots, b_{X_Y}, \ldots]^{\mathrm{T}}$ to represent the z_{X_Y}'s and the b_{X_Y}'s in the cluster centered at Y, respectively. Given $\boldsymbol{z}_Y$ and $\boldsymbol{b}_Y$, we can write the power of $I_{\mathrm{BT}}(t)$ as

$$\tilde{\mathcal{I}}_{\mathrm{BT}} = \mathbb{E}_{s_Y}\left[|I_{\mathrm{BT}}(t)|^2\right] = \eta P_{\mathrm{tx}} \sum_{Y \in \Phi_{\mathrm{P}}} \left|\boldsymbol{z}_Y^{\mathrm{T}} \boldsymbol{b}_Y\right|^2. \tag{3.6}$$

Next, deconditioning $\tilde{\mathcal{I}}_{\mathrm{BT}}$ on the channel phases[3] and backscattered symbols, we obtain

$$\mathcal{I}_{\mathrm{BT}} = \sum_{Y \in \Phi_{\mathrm{P}}} \mathbb{E}_{\boldsymbol{b}_Y, \theta}\left[\tilde{\mathcal{I}}_{\mathrm{BT}}\right] = \eta P_{\mathrm{tx}} \sum_{Y \in \Phi_{\mathrm{P}}} \mathbb{E}_{\boldsymbol{b}_Y}\left[\boldsymbol{b}_Y^{\mathrm{T}} \mathbb{E}_{\theta}\left[\boldsymbol{z}_Y \boldsymbol{z}_Y^{\mathrm{H}}\right] \boldsymbol{b}_Y\right] = \frac{\eta P_{\mathrm{tx}}}{2} \sum_{Y \in \Phi_{\mathrm{P}}} \sum_{X_Y \in \Phi_{\mathrm{B}}} \mathcal{Z}_{X_Y} \tag{3.7}$$

where $\mathcal{Z}_{X_Y} \triangleq g_{X_Y,\mathrm{tx}} g_{X_Y,\mathrm{rx}} L(r_{X_Y,\mathrm{tx}}) L(r_{X_Y,\mathrm{rx}})$ and the last equation follows from the facts that $\mathbb{E}_{\theta}\left[\boldsymbol{z}_Y \boldsymbol{z}_Y^{\mathrm{H}}\right]$ is a diagonal matrix and $\mathbb{E}[b_{X_Y}^2(n)] = 1/2,\ \forall X_Y$. Similarly, the powers of $s_{\mathrm{PT}}(t),\ s_{\mathrm{BT}}(t),$ and $I_{\mathrm{PT}}(t)$ can be represented as

$$\mathcal{S}_{\mathrm{PT}} = g_{Y_0} L(r_0) P_{\mathrm{tx}}, \tag{3.8}$$

$$\mathcal{S}_{\mathrm{BT}} = \frac{\eta P_{\mathrm{tx}}}{2} \sum_{X_{Y_0} \in \Phi_{\mathrm{B}}(Y_0)} \mathcal{Z}_{X_{Y_0}}, \tag{3.9}$$

$$\mathcal{I}_{\mathrm{PT}} = \sum_{Y \in \Phi_{\mathrm{P}}} g_Y L(r_Y) P_{\mathrm{tx}}, \tag{3.10}$$

[3]assuming that the channel phases change faster than amplitudes.

respectively. We note that the mutual correlations among the signals $s_{\mathrm{PT}}(t)$, $s_{\mathrm{BT}}(t)$, $I_{\mathrm{PT}}(t)$, and $I_{\mathrm{BT}}(t)$, can be neglected if we decondition the correlations on the channel phases and use the fact that $s_{Y}(t)$'s are i.i.d. zero mean Gaussian.

The typical PR aims to receive the typical PT's signal $s_{Y_0}(t)$, which is contained in $s_{\mathrm{PT}}(t)$ and $s_{\mathrm{BT}}(t)$. However, the time delays of the PT-BT-PR paths are larger than the time delay of the direct PT-PR path and are random due to the PPP formed by the BT locations, which may introduce different levels of inter symbol interference (ISI) at the typical PR. Therefore, $s_{\mathrm{BT}}(t)$ has a two-side effect, i.e., causing interference or enhancing the detection at the PR. Particularly, [65] concludes that AmBC causes little interference to legacy systems in some deployment scenarios, and [83] indicates that detection performance can be enhanced with the cooperation of AmBC nodes. In this chapter, we parameterize the two-side effect with $\beta \in [0,1]$, which denotes the fraction of the backscattered signal power that is not regarded as interference[4]. Next, given $\beta \in [0,1]$, we can represent the SINR at the typical PR as

$$\mathrm{SINR} = \frac{\mathcal{S}_{\mathrm{PT}} + \beta \mathcal{S}_{\mathrm{BT}}}{(1-\beta)\mathcal{S}_{\mathrm{BT}} + \mathcal{I}_{\mathrm{PT}} + \mathcal{I}_{\mathrm{BT}} \cdot \mathbb{1}(\mathcal{I}_{\mathrm{BT}}) + \sigma^2}, \tag{3.11}$$

where $\mathbb{1}(\mathcal{I}_{\mathrm{BT}}) = 1$ for scenario-1, and $\mathbb{1}(\mathcal{I}_{\mathrm{BT}}) = 0$ for scenario-2. We note that both scenarios can be interference-limited if the transmit signal-to-receive-noise ratio (TSRNR) P_{tx}/σ^2 is large enough.

3.3.2 Coverage Probability Expression

Denoting the SINR or SIR threshold at the typical PR as Γ, the SINR-based coverage probability is defined as the probability that the SINR is no less than the threshold:

$$\mathbb{P}_c = \mathbb{P}(\mathrm{SINR} \geq \Gamma) = \mathbb{P}(\mathcal{S}_{\mathrm{PT}} \geq [\Gamma(1-\beta) - \beta]\,\mathcal{S}_{\mathrm{BT}} + \Gamma \mathcal{I}_{\mathrm{PT}} + \Gamma \mathcal{I}_{\mathrm{BT}} \mathbb{1}(\mathcal{I}_{\mathrm{BT}}) + \Gamma \sigma^2), \tag{3.12}$$

[4]We note β can be estimated with several system parameters. For instance, with the distance between the typical PT and PR, the distribution range of the BTs, the symbol rate of a PT, and the maximum tolerable delay for the typical PR, we can compute the region where the active BTs cause interference. Then we can calculate the ratio between the expected aggregate signal power from the BTs within and out of that area.

By setting $\sigma^2 = 0$ in (3.12), the SIR-based coverage probability can be found. To calculate the coverage probabilities, we will need the following lemmas.

Lemma 2. *To analyze the aggregate signal power at the typical PR, the clustered BTs can be approximately regarded as a virtual transmitter (VT) located at the center of the cluster. The VT's transmit power is the sum of backscattered signal powers* $\tilde{P}_{\rm tx}$ *of all BTs in the cluster, which is derived as*

$$\begin{aligned}\tilde{P}_{\rm tx} = \mathbb{E}\left[\sum_{X_Y \in \Phi_{\rm B}(Y)} g_{X_Y,{\rm tx}} L(r_{X_Y,{\rm tx}}) P_{\rm tx}\right] &\overset{(a)}{=} \lambda_{\rm B} \int_{B(Y,\rho)} \mathbb{E}\left[g_{{\rm X_Y},{\rm tx}}\right] L(r_{{\rm X_Y},{\rm tx}}) dX_Y P_{\rm tx} \\ &\overset{(b)}{=} \frac{2\pi}{\mu}\lambda_{\rm B}\left(\int_0^{\rho} \frac{r}{r^{\alpha}+1} dr\right) P_{\rm tx} = \gamma P_{\rm tx}\end{aligned} \tag{3.13}$$

where (a) is from the Campbell Theorem, (b) is by changing Cartesian coordinates to polar coordinates, and the last equality is achieved by defining $\gamma \triangleq \frac{2\pi}{\mu}\lambda_{\rm B}\int_0^{\rho}\frac{r}{r^{\alpha}+1}dr$.

Lemma 3. *The Laplace transform of the probability density function (PDF) of the double fading random variable* $g = g_1 g_2$*, where* $g_1, g_2 \sim \exp(\mu)$ *is*

$$\mathcal{L}_g(s) = \mathbb{E}\left[\exp(-sg)\right] = \int_0^{\infty} e^{-sg} \int_0^{\infty} \frac{\mu^2}{t} e^{-\mu\left(t+\frac{g}{t}\right)} dt dg = \int_0^{\infty} \frac{\mu^2 e^{-\mu t}}{st+\mu} dt \tag{3.14}$$

where we use the fact that the PDF of g *is*

$$f_g(g) = \int_0^{\infty} \frac{\mu^2}{t} e^{-\mu\left(t+\frac{g}{t}\right)} dt \tag{3.15}$$

which can be derived according to the PDF of the product of two random variables.

Lemma 4. *Denoting* $G = \omega_1 g_1 + \omega_2 g_2$ *as the nonnegative weighted sum of two independent exponential random variables,* $g_i \sim \exp(\mu_i),\ i = 1, 2,$ *where* $\omega_i \geq 0$*, the cumulative distribution function (CDF) of* G *is*

$$F_G(g) = 1 - \frac{\tilde{\mu}_1}{\tilde{\mu}_1 - \tilde{\mu}_2} e^{-\tilde{\mu}_2 g} + \frac{\tilde{\mu}_2}{\tilde{\mu}_1 - \tilde{\mu}_2} e^{-\tilde{\mu}_1 g},\ g \geq 0 \tag{3.16}$$

where $\tilde{\mu}_i = \mu_i/\omega_i, i = 1, 2.$

Proof. Please see Appendix 3.6.1. □

According to whether $\Gamma(1-\beta)-\beta$ is negative or not, the coverage probabilities are shown in the following theorems.

Theorem 1. *When* $0 \leq \beta \leq \frac{\Gamma}{\Gamma+1}$*, i.e.,* $\Gamma(1-\beta)-\beta \geq 0$*, the SINR based coverage probabilities for the two scenarios are*

$$\mathbb{P}_c \approx \begin{cases} \xi_1 \xi_2 \zeta_1, & \textit{for scenario-1} \\ \xi_1 \xi_{2,\mathrm{u}} \zeta_1, & \textit{for scenario-2}, \end{cases} \tag{3.17}$$

where

$$\xi_1 = \exp\left\{-\lambda_{\mathrm{B}} \int_{X_{Y_0} \in B(Y_0,\rho)} \left(1 - \int_0^{\infty} \frac{\mu^2 e^{-\mu t}}{a_{X_{Y_0}} t + \mu} dt\right) dX_{Y_0}\right\},$$

$$\xi_2 = \exp\left\{-2\pi\lambda_{\mathrm{P}} \int_{r_0}^{R} \left(1 - \frac{1}{1+\Gamma\frac{L(r)}{L(r_0)}} \frac{1}{1+\gamma\Gamma\frac{L(r)}{L(r_0)}}\right) rdr\right\},$$

$$\xi_{2,\mathrm{u}} = \exp\left\{-2\pi\lambda_{\mathrm{P}} \int_{r_0}^{R} \left(1 - \frac{1}{1+\Gamma\frac{L(r)}{L(r_0)}}\right) rdr\right\},$$

$$\zeta_1 = \exp\left(-\frac{\mu\sigma^2\Gamma}{L(r_0)P_{\mathrm{tx}}}\right),$$

and $a_{X_{Y_0}} = \frac{\mu\eta[\Gamma(1-\beta)-\beta]}{2L(r_0)} L(r_{X_{Y_0},\mathrm{tx}}) L(r_{X_{Y_0},\mathrm{rx}})$.

Proof. Please see Appendix 3.6.2. □

Theorem 1 indicates that the coverage probabilities are the multiplications of two or three specific terms when β is not greater than the threshold $\frac{\Gamma}{\Gamma+1}$. In particular, ξ_1 corresponds to the effect of BTs around the typical PT, ξ_2 corresponds to the interference effect of atypical PTs and their surrounding BTs for scenario-1, $\xi_{2,\mathrm{u}}$ corresponds to the interference effect of atypical PTs for scenario-2, and ζ_1 corresponds to the noise effect. Furthermore, the coverage probabilities in scenario-1 are upper bounded by the coverage probabilities in scenario-2 since $\xi_2 < \xi_{2,\mathrm{u}}$.

Theorem 2. *When* $\frac{\Gamma}{\Gamma+1} < \beta \leq 1$*, i.e.,* $\Gamma(1-\beta)-\beta < 0$*, the SINR based coverage probabilities of the two scenarios are*

$$\mathbb{P}_c \approx \begin{cases} \frac{\tilde{\gamma}}{\tilde{\gamma}-1}\xi_3\zeta_2 - \frac{1}{\tilde{\gamma}-1}\xi_2\zeta_1, & \textit{for scenario-1} \\ \frac{\tilde{\gamma}}{\tilde{\gamma}-1}\xi_{3,\mathrm{u}}\zeta_2 - \frac{1}{\tilde{\gamma}-1}\xi_{2,\mathrm{u}}\zeta_1, & \textit{for scenario-2,} \end{cases} \tag{3.18}$$

where

$$\xi_3 = \exp\left\{ -2\pi\lambda_{\mathrm{P}} \int_{r_0}^{R} \left(1 - \frac{1}{1+\frac{\Gamma L(r)}{\tilde{\gamma}L(r_0)}} \frac{1}{1+\frac{\gamma\Gamma L(r)}{\tilde{\gamma}L(r_0)}}\right) rdr \right\},$$

$$\xi_{3,\mathrm{u}} = \exp\left\{ -2\pi\lambda_{\mathrm{P}} \int_{r_0}^{R} \left(1 - \frac{1}{1+\frac{\Gamma L(r)}{\tilde{\gamma}L(r_0)}}\right) rdr \right\},$$

$\zeta_2 = \exp\left(-\frac{\mu\sigma^2\Gamma}{\tilde{\gamma}L(r_0)P_{\mathrm{tx}}}\right), \tilde{\gamma} = -\left[\Gamma(1-\beta)-\beta\right]\gamma > 0$*, and* γ *is defined in Lemma 2.*

Proof. Please see Appendix 3.6.3. □

Different from the simple multiplication forms of Theorem 1 where each term in the multiplication corresponds to a specific effect, the coverage probabilities for β greater than the threshold $\frac{\Gamma}{\Gamma+1}$ are more complicated. Specifically, the coverage probabilities in Theorem 2 are expressed by weighted sums of the multiplications among ξ_2, $\xi_{2,\mathrm{u}}$, ξ_3, $\xi_{3,\mathrm{u}}$, ζ_1, and ζ_2 since we use a VT to approximate the BTs around the typical PT. In this case, the VT's effect is embodied by $\tilde{\gamma}$, ξ_3, $\xi_{3,\mathrm{u}}$, and ζ_2. Furthermore, as P_{tx}/σ^2 increases toward infinity, ζ_1 and ζ_2 approach 1, so that the SINR based coverage probabilities will converge to the SIR based coverage probabilities for an arbitrary β.

3.4 Numerical Results and Discussions

The simulation results of both scenarios are shown in Fig. 3.4-3.7 where we use Monte Carlo simulations with 50000 independent system realizations to verify the analytical results. We set $\lambda_{\mathrm{P}} = 2 \times 10^{-4}, \lambda_{\mathrm{B}} = 0.1, \rho = 10, R = 100, \eta = 0.5, \alpha = 3.5$ by default. Other system

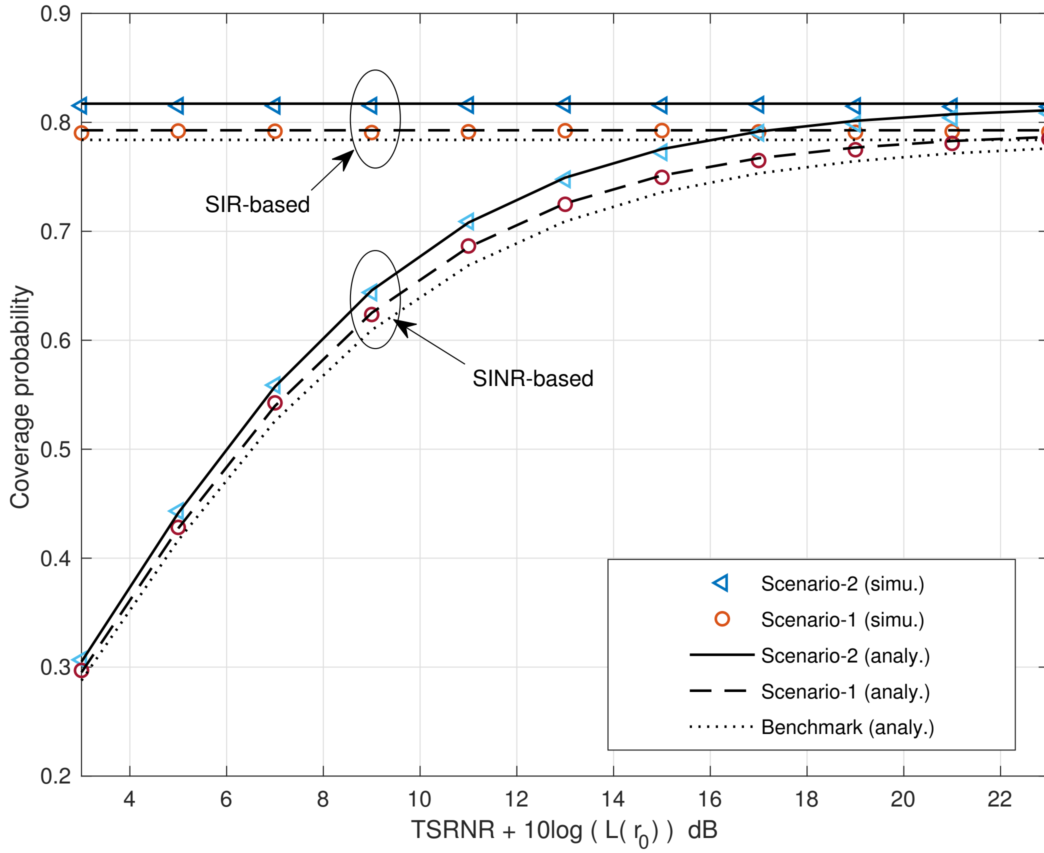

Figure 3.3: Coverage probability versus TSRNR deducting the absolute value of path loss. ($r_0 = 15, \Gamma = 3\text{dB}, \mu = 1, \beta = 0.8$)

settings are illustrated in the captions of figures. Additionally, we also compare our results with the classic scenario (as a benchmark) where no BT exists (i.e., the interference received by the typical PR is only from atypical PTs).

The effect of TSRNR on the coverage probabilities is shown in Fig. 3.3, where the horizontal axis represents the TSRNR after deducting the absolute value of path loss (which is $10\log_{10}(L(r_0)^{-1}) = 41$ dB). Clearly, the SIR based coverage probabilities are not affected by the TSRNR. However, the SINR based coverage probabilities gradually increase with the growth of TSRNR, finally converge to the SIR curves. With the listed system parameters,

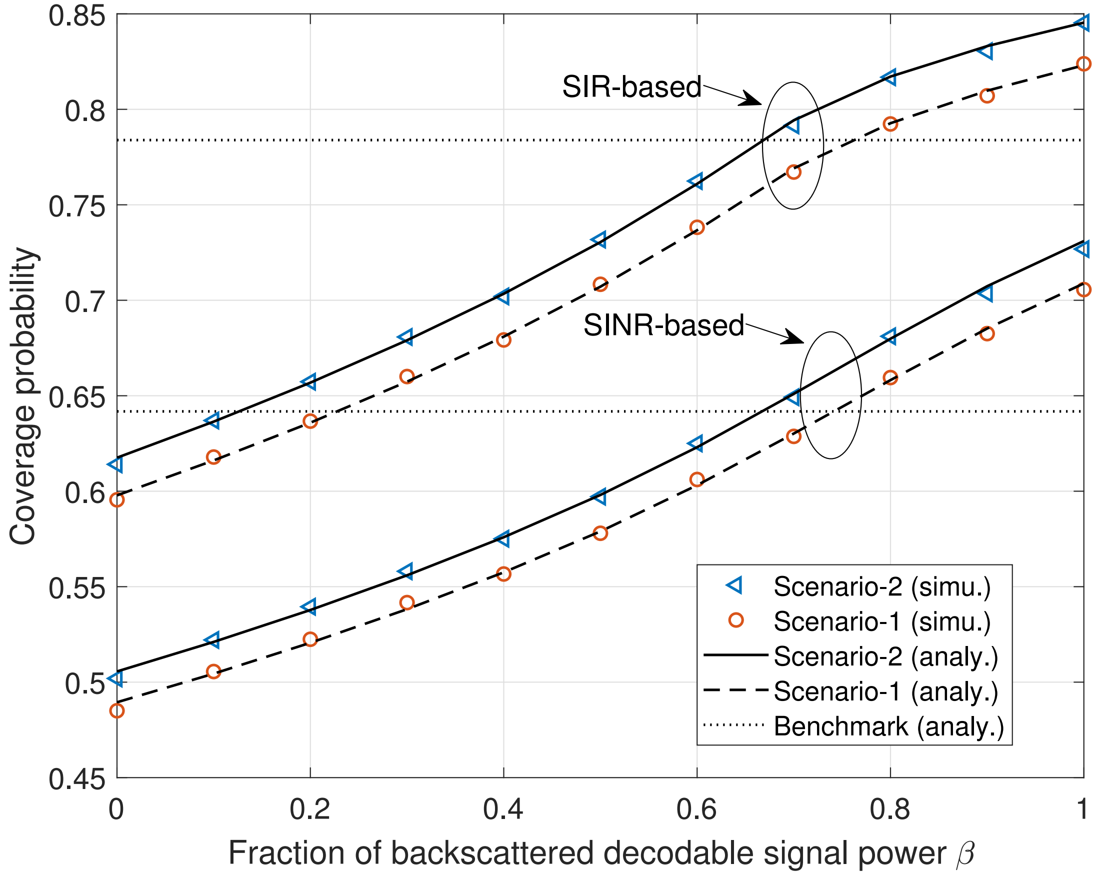

Figure 3.4: Coverage probability versus useful signal power ratio β. ($r_0 = 15, \Gamma = 3\text{dB}, \mu = 1, \text{TSRNR} = 51\text{dB}$)

we observe that the TSRNR should be no less than 23 dB to make the SIR based coverage probabilities as accurate as the SINR based results. We set $r_0 = 15$ as a standard value for comparison and use TSRNR = 51 dB, i.e., the TSRNR after deducting the absolute value of path loss is 10 dB (except for Fig. 3.6 where r_0 is a variable).

Fig. 3.4 shows the coverage probabilities for different values of β. From 0 to 1, the value of β indicates the fraction of backscattered signal power from the typical PT that can enhance the SINR and SIR at the typical PR. With the growth of β, the coverage probabilities of both scenario-1 and scenario-2 increase. In addition, when β is larger than

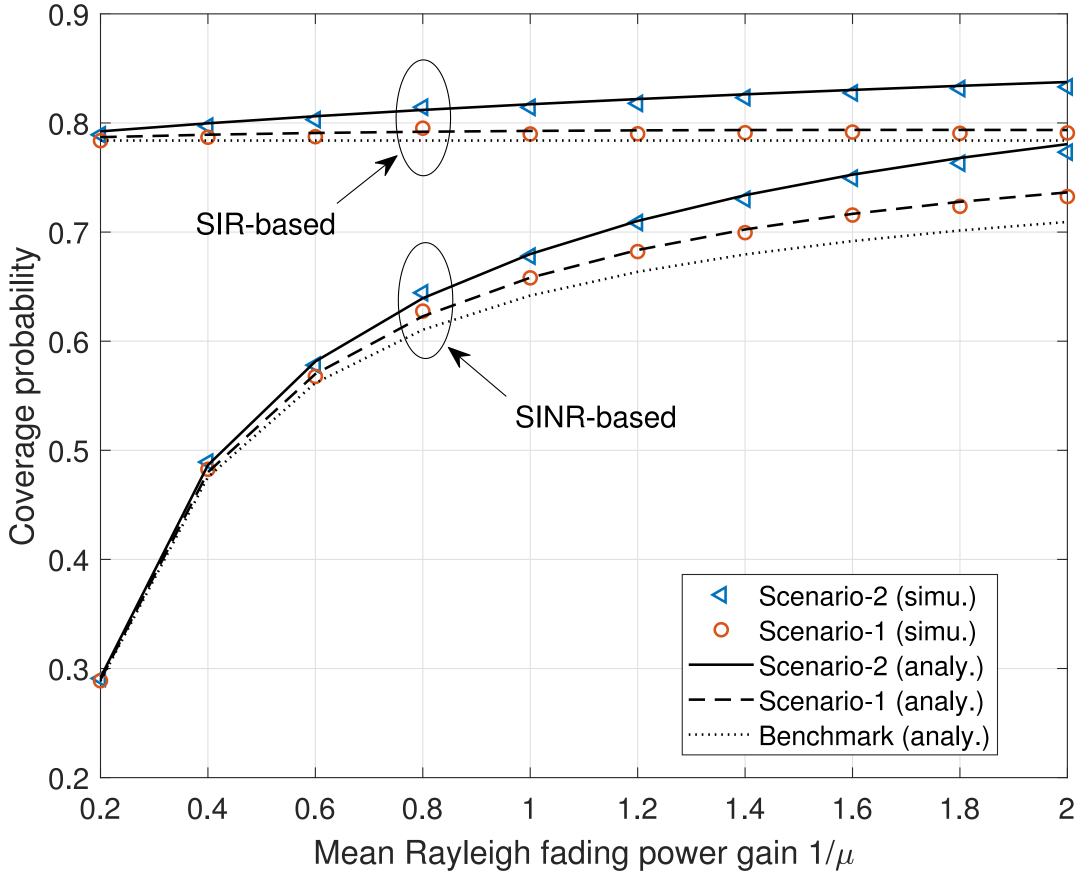

Figure 3.5: Coverage probability versus mean fading power gain. ($r_0 = 15, \Gamma = 3\text{dB}, \beta = 0.8, \text{TSRNR} = 51\text{dB}$)

a certain value, the coverage probabilities of scenario-1 and scenario-2 exceeds the coverage probability of the benchmark scenario. These results correspond to the fact that the effect of backscattered signals has two sides: interference inducing and signal enhancing, i.e., the interference dominates when β is less than the specific value, while the decodable signals dominate when β is greater than that value.

Typically, the mean power gain $1/\mu$ can be canceled in deriving the SIR based coverage probabilities for most of the network models (e.g., the benchmark scenario), if the channels are described as i.i.d. Rayleigh fading. However, in the considered two AmBC network

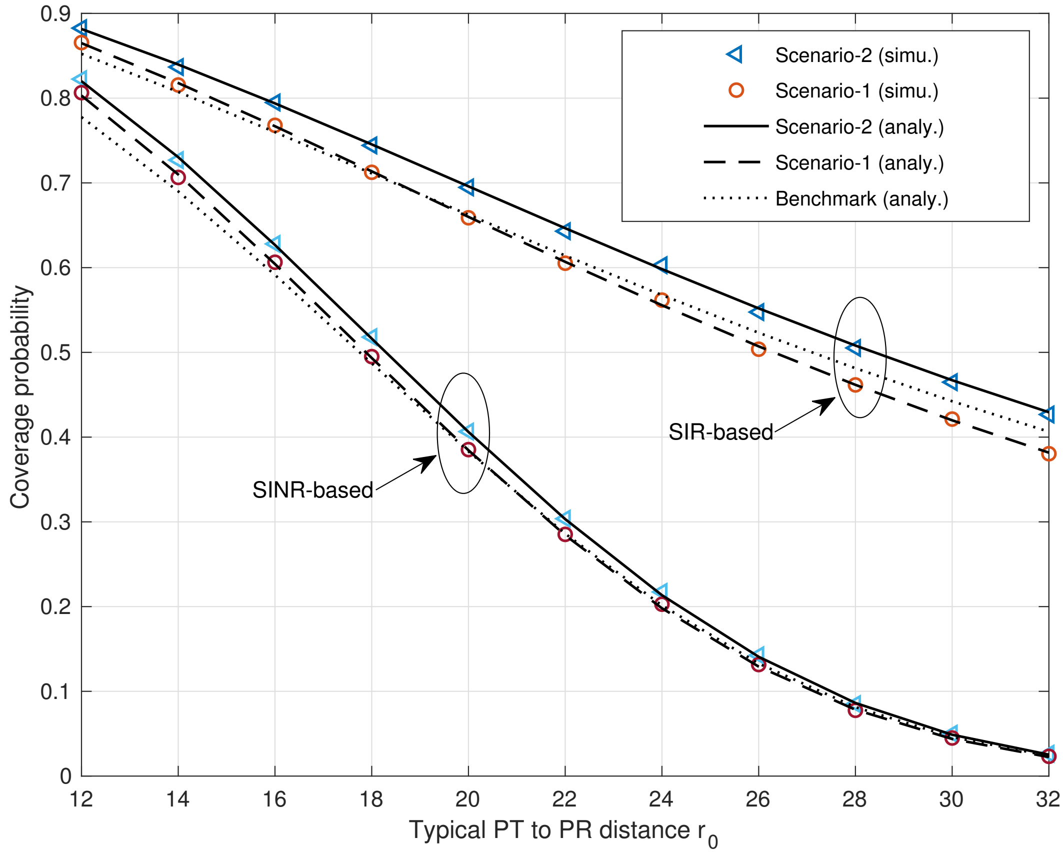

Figure 3.6: Coverage probability versus typical PT to PR distance r_0. ($\Gamma = 3\text{dB}, \beta = 0.8, \mu = 1, \text{TSRNR} = 51\text{dB}$)

scenarios, the channel power gains of the PT-BT path and the BT-PR path are multiplied due to the double fading effect, making the coverage probabilities more sensitive to the channel fading gain. As shown in Fig. 3.5, the SIR based coverage probability of the benchmark scenario does not change with the fading power gain, but the SIR based probabilities for scenario-1 and scenario-2 increase with the growth of $1/\mu$. As the fading power gain grows, the SINR based coverage probabilities of all three scenarios increase, and tend to converge to the SIR based results since the noise becomes less significant.

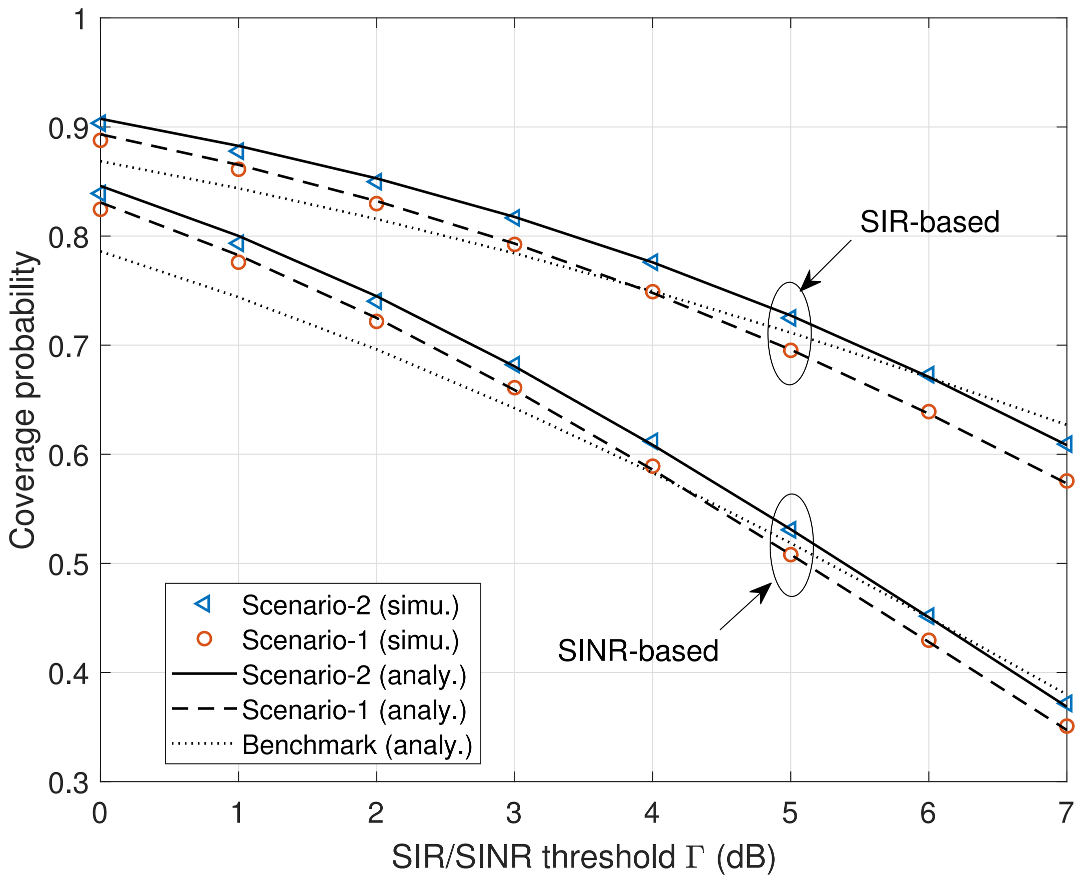

Figure 3.7: Coverage probability versus SIR threshold Γ. ($r_0 = 15, \beta = 0.8, \mu = 1, \mathrm{TSRNR} = 51\mathrm{dB}$)

Fig. 3.6 shows that the coverage probabilities decrease with the increase of the typical PT to PR distance r_0. Moreover, as r_0 increases, BTs' signal enhancing effect becomes less significant than their interference effect, leading to the coverage probability of the benchmark scenario exceeds the coverage probability of scenario-1. Besides, the SINR based curves have steeper inclinations than the SIR based curves do for $r_0 < 26$, but gentler inclinations for $r_0 > 28$. This is because as the distance r_0 increases, the signal power from the typical PT and its surrounding BTs decreases exponentially, resulting in the SINR being dominated by noise.

It is observed in Fig. 3.7 that the coverage probabilities decrease as the SINR/SIR threshold Γ increases. Moreover, with the growth of Γ, BTs' signal enhancing effect becomes less significant than their interference effect, leading to the coverage probabilities of the benchmark scenario exceed the coverage probabilities of scenario-1 and scenario-2. Besides, the SINR based curves always have greater inclinations than the SIR based curves do, due to the noise effect formulated by ζ_1 and ζ_2 in Theorem 2.

3.5 Conclusion

Our considered scheme enables a branch of novel communication devices where randomly distributed ambient backscatter nodes are involved as secondary users which have no or little self power supply. Considering the double-fading effect, we derive the SINR and SIR based coverage probabilities for two network configuration scenarios with two ranges of β values. The coverage probabilities of the considered scheme lie in a wide range around the coverage probability of the conventional model, depending on the system settings. Numerical results indicate the possibility and advantages to involve a large amount of AmBC nodes in existing wireless networks.

3.6 Appendix

3.6.1 Proof of Lemma 4

Let $\tilde{g}_i = \omega_i g_i, i = 1, 2$. Then, we recognize $\tilde{g}_i$ is exponentially distributed with mean $1/\tilde{\mu}_i = \omega_i/\mu_i$ and have

$$\begin{aligned} F_G(g) = \mathbb{P}\left(\tilde{g}_1 \leq g - \tilde{g}_2\right) &= \int_0^g \int_0^{g-t_2} \tilde{\mu}_1 e^{-\tilde{\mu}_1 t_1} \tilde{\mu}_2 e^{-\tilde{\mu}_2 t_2} dt_1 dt_2 \\ &= 1 - \frac{\tilde{\mu}_1}{\tilde{\mu}_1 - \tilde{\mu}_2} e^{-\tilde{\mu}_2 g} + \frac{\tilde{\mu}_2}{\tilde{\mu}_1 - \tilde{\mu}_2} e^{-\tilde{\mu}_1 g} \end{aligned} \tag{3.19}$$

for $g \geq 0$.

3.6.2 Proof of Theorem 1

For scenario-1, substituting (3.7)-(3.10) to (3.12), we obtain (a) in (3.20).

$$
\begin{aligned}
&\mathbb{P}(\mathrm{SINR} \geq \Gamma) \\
&\overset{(a)}{=} \mathbb{P}\Bigg\{ g_{Y_0} \geq \frac{1}{L(r_0)} \Big[(\Gamma(1-\beta)-\beta)\frac{\eta}{2} \sum_{X_{Y_0} \in \Phi_{\mathrm{B}}(Y_0)} \mathcal{Z}_{X_{Y_0}} + \Gamma \sum_{Y \in \Phi_{\mathrm{P}}} g_Y L(r_Y) + \frac{\sigma^2 \Gamma}{P_{\mathrm{tx}}} \\
&\qquad + \Gamma \frac{\eta}{2} \sum_{Y \in \Phi_{\mathrm{P}}} \sum_{X_Y \in \Phi_{\mathrm{B}}(Y)} \mathcal{Z}_{X_Y} \Big] \Bigg\} \\
&\overset{(b)}{\approx} \mathbb{P}\Bigg\{ g_{Y_0} \geq \frac{1}{L(r_0)} \Big[(\Gamma(1-\beta)-\beta)\frac{\eta}{2} \sum_{X_{Y_0} \in \Phi_{\mathrm{B}}(Y_0)} \mathcal{Z}_{X_{Y_0}} + \Gamma \sum_{Y \in \Phi_{\mathrm{P}}} (g_Y + \gamma \tilde{g}_Y) L(r_Y) + \frac{\sigma^2 \Gamma}{P_{\mathrm{tx}}} \Big] \Bigg\} \\
&\overset{(c)}{=} \mathbb{E}\Bigg\{ \exp\Bigg(\frac{-\mu}{L(r_0)} \Big[(\Gamma(1-\beta)-\beta)\frac{\eta}{2} \sum_{X_{Y_0} \in \Phi_{\mathrm{B}}(Y_0)} \mathcal{Z}_{X_{Y_0}} + \Gamma \sum_{Y \in \Phi_{\mathrm{P}}} (g_Y + \gamma \tilde{g}_Y) L(r_Y) + \frac{\sigma^2 \Gamma}{P_{\mathrm{tx}}} \Big] \Bigg) \Bigg\} \\
&\overset{(d)}{=} \mathbb{E}\Bigg\{ \exp\Bigg(- \sum_{X_{Y_0} \in \Phi_{\mathrm{B}}(Y_0)} a_{X_{Y_0}} g_{X_{Y_0},\mathrm{tx}} g_{X_{Y_0},\mathrm{rx}} - \frac{\mu \Gamma}{L(r_0)} \sum_{Y \in \Phi_{\mathrm{P}}} (g_Y + \gamma \tilde{g}_Y) L(r_Y) \Bigg) \Bigg\} \exp\Bigg(\frac{-\mu \sigma^2 \Gamma}{L(r_0) P_{\mathrm{tx}}} \Bigg) \\
&\overset{(e)}{=} \mathbb{E}\Bigg\{ \exp\Bigg(- \sum_{X_{Y_0} \in \Phi_{\mathrm{B}}(Y_0)} a_{X_{Y_0}} g_{X_{Y_0},\mathrm{tx}} g_{X_{Y_0},\mathrm{rx}} \Bigg) \Bigg\} \times \mathbb{E}\Bigg\{ \exp\Bigg(- \frac{\mu \Gamma}{L(r_0)} \sum_{Y \in \Phi_{\mathrm{P}}} (g_Y + \gamma \tilde{g}_Y) L(r_Y) \Bigg) \Bigg\} \zeta_1
\end{aligned}
\tag{3.20}
$$

Then, (b) results from using Lemma 2 to replace the clustered BTs around atypical PTs with VTs, where $\tilde{g}_{\mathrm{Y}} \sim \exp(\mu)$ (with $Y \in \Phi_{\mathrm{P}}$) is the mean fading power gain of the channel between the VT at Y (co-located with the PT) and the typical PR. (c) is from the complementary cumulative distribution function (CCDF) of exponential random variable g_{Y_0}. Substituting $a_{X_{Y_0}} = \frac{\mu\eta[\Gamma(1-\beta)-\beta]}{2L(r_0)} L(r_{X_{Y_0},\mathrm{tx}}) L(r_{X_{Y_0},\mathrm{rx}})$ to (c), we obtain (d). Next, (d) is written as the product of two expectations in (e) due to the independence between X_{Y_0} and Y.

Furthermore, we derive (3.21) and (3.22) as follows,

$$\begin{aligned}
&\mathbb{E}\Bigg\{\exp\Bigg(-\sum_{X_{Y_0}\in\Phi_B(Y_0)} a_{X_{Y_0}} g_{X_{Y_0},\mathrm{tx}} g_{X_{Y_0},\mathrm{rx}}\Bigg)\Bigg\}\\
&= \mathop{\mathbb{E}}_{\Phi_B(Y_0)}\Bigg\{\prod_{X_{Y_0}\in\Phi_B(Y_0)} \mathop{\mathbb{E}}_{g_{X_{Y_0}}}\left[\exp\left(-a_{X_{Y_0}} g_{X_{Y_0}}\right)\right]\Bigg\}\\
&\overset{(a)}{=} \exp\left\{-\lambda_B \int_{B(Y_0,\rho)}\left(1-\mathop{\mathbb{E}}_{g_{X_{Y_0}}}\left[e^{-a_{X_{Y_0}} g_{X_{Y_0}}}\right]\right) dX_{Y_0}\right\}\\
&\overset{(b)}{=} \exp\left\{-\lambda_B \int_{B(Y_0,\rho)}\left(1-\int_0^\infty \frac{\mu^2 e^{-\mu t}}{a_{X_{Y_0}} t+\mu} dt\right) dX_{Y_0}\right\}\\
&= \xi_1
\end{aligned} \tag{3.21}$$

$$\begin{aligned}
&\mathbb{E}\Bigg\{\exp\Bigg(-\frac{\mu\Gamma}{L(r_0)}\sum_{Y\in\Phi_P}(g_Y+\gamma\tilde{g}_Y)L(r_Y)\Bigg)\Bigg\}\\
&= \mathbb{E}\Bigg\{\prod_{Y\in\Phi_P}\exp\Bigg(-\frac{\mu\Gamma}{L(r_0)}(g_Y+\gamma\tilde{g}_Y)L(r_Y)\Bigg)\Bigg\}\\
&\overset{(a)}{=} \exp\left\{-\lambda_P\int_{\mathbb{D}}\left(1-\mathop{\mathbb{E}}_{g_Y,\tilde{g}_Y}\left[e^{\frac{-\mu\Gamma}{L(r_0)}(g_Y+\gamma\tilde{g}_Y)L(r_Y)}\right]\right)dY\right\}\\
&\overset{(b)}{=} \exp\left\{-\lambda_P\int_0^{2\pi}\int_{r_0}^{R}\left(1-\mathbb{E}\left[e^{\frac{-\mu\Gamma L(r)}{L(r_0)}(g_Y+\gamma\tilde{g}_Y)}\right]\right)rdrd\theta\right\}\\
&\overset{(c)}{=} \exp\left\{-2\pi\lambda_P\int_{r_0}^{R}\left(1-\frac{1}{1+\Gamma\frac{r_0^\alpha+1}{r^\alpha+1}}\frac{1}{1+\gamma\Gamma\frac{r_0^\alpha+1}{r^\alpha+1}}\right)rdr\right\}\\
&= \xi_2
\end{aligned} \tag{3.22}$$

where $g_{X_{Y_0}} \triangleq g_{X_{Y_0},\mathrm{tx}} g_{X_{Y_0},\mathrm{rx}}$, and $\mathbb{D} = B(\mathbf{0}, r_0) - B(\mathbf{0}, R)$ is the distribution range of Y. (a) in (3.21) and (3.22) is from the probability generating functional (PGFL) of PPP [23]. Then, we obtain (b) in (3.21) by Lemma 3. By changing Cartesian coordinates to polar coordinates and calculating the expectation, (b) and (c) in (3.22) are obtained in sequence. Thus, we obtain $\mathbb{P}(\mathrm{SINR} \geq \Gamma) \approx \xi_1\xi_2\zeta_1$ by substituting (3.21) and (3.22) to (3.20). Setting $\frac{\sigma^2}{P_{\mathrm{tx}}} = 0$ (i.e., $\zeta_1 = 1$), we can obtain the SIR based coverage probabilities. We omit the similar derivation for scenario-2.

3.6.3 Proof of Theorem 2

When $\Gamma(1-\beta)-\beta < 0$, the right-hand-side term of $\geq$ in (a) of (3.20) is not guaranteed to be non-negative. In this case, we further approximate the sum power from the clustered BTs around the typical PT as the power from a VT located at Y_0. Then, from (b) in (3.20), the coverage probability is written as

$$\begin{aligned}\mathbb{P}_c &\overset{(a)}{\approx} \mathbb{P}\left\{ g_{Y_0} + \tilde{\gamma}\tilde{g}_{Y_0} \geq \frac{\Gamma}{L(r_0)} \sum_{Y\in\Phi_{\mathrm{P}}} (g_Y + \gamma\tilde{g}_Y)L(r_Y) + \frac{\sigma^2\Gamma}{P_{\mathrm{tx}}} \right\} \\ &\overset{(b)}{=} \frac{\mu}{\mu-\mu/\tilde{\gamma}} \mathbb{E}\Big[\exp\Big(\frac{-\mu\Gamma}{\tilde{\gamma}L(r_{Y_0})} \sum_{Y\in\Phi_{\mathrm{P}}} (g_Y + \gamma\tilde{g}_Y)L(r_Y) \Big)\Big]\zeta_2 \\ &\quad - \frac{\mu/\tilde{\gamma}}{\mu-\mu/\tilde{\gamma}} \mathbb{E}\Big[\exp\Big(\frac{-\mu\Gamma}{L(r_{Y_0})} \sum_{Y\in\Phi_{\mathrm{P}}} (g_Y + \gamma\tilde{g}_Y)L(r_Y) \Big)\Big]\zeta_1 \\ &\overset{(c)}{=} \frac{\tilde{\gamma}}{\tilde{\gamma}-1}\xi_3\zeta_2 - \frac{1}{\tilde{\gamma}-1}\xi_2\zeta_1\end{aligned} \tag{3.23}$$

where $\tilde{\gamma} = -\left[\Gamma(1-\beta)-\beta\right]\gamma > 0$. (a) results from using Lemma 2 to replace the clustered BTs around the typical PT with a VT, where $\tilde{g}_{Y_0} \sim \exp(\mu)$ is the mean power gain of the channel between the VT at Y_0 and the typical PR. Then, (b) is obtained by calculating the CCDF of $g_{Y_0} + \tilde{\gamma}\tilde{g}_{Y_0}$ with Lemma 4. Finally, we have (c) using PGFL of PPP, changing coordinates and calculating the expectation (with the same steps as in (3.22)). Setting $\frac{\sigma^2}{P_{\mathrm{tx}}} = 0$, we can obtain the SIR based coverage probabilities. We omit the similar derivation for scenario-2.

CHAPTER 4

PERFORMANCE ANALYSIS OF DISTRIBUTED AUXILIARY RADIO TELESCOPES UNDER SHARED SPECTRUM ACCESS PARADIGM AND COOLING POWER CONSTRAINT

4.1 Introduction

This chapter proposes a DART system which can geographically and spectrally coexist with CWC while offering additional capability or performance enhancement to RAS. Currently, there are two types of RAS, namely single-dish telescope and telescope array. Single-dish telescope has unique advantages such as good potential sensitivity to large scale structure, building and maintaining simplicity and upgrading flexibility [17]. Numerous single-dish telescopes have been built, e.g., the 305-meter Arecibo Observatory built in 1963 and the Five hundred meter Aperture Spherical Telescope (FAST) completed in last year. Nevertheless, the single-dish telescope also has shortcomings in spatial frequency response and mechanical complexity perspectives [17] compared with the radio telescope array. Processing the signals received by a telescope array can mitigate the interference and increase the observation range and resolution. Therefore, we have also seen the prosperity of radio telescope arrays such as the Very Large Array (VLA) and the Square Kilometer Array (SKA) and a trend of combination among single-dish telescopes and telescope arrays. Nevertheless, these existing RAS sites are protected by radio quiet zones and cannot coexist with CWC.

To accommodate expansions of both CWC and RAS, we embrace the shared spectrum access paradigm of [52] and propose a DART system which can coexist with CWC and conventional single-dish RAS. Our DART system can either work independently as a radio telescope array or cooperate with an existing single-dish RAS to increase the overall performance accuracy. We derive analytical performance expressions for signal power estimation of the DART system with different quantization resolutions, and then obtain approximate closed-form expressions. We observe that a larger resolution of analog-to-digital converter (ADC) yields a smaller bias but a larger variance to the RAS signal power estimation. These biases remain relatively constant within the typical range of RAS signal-to-noise ratio (SNR), thus the bias can be compensated. However, after the bias compensation, the resulting variance of the RAS signal power estimate is also changed and a higher ADC resolution provides better performance in terms of estimation variance (after the bias compensation). Next, we also obtain an analytical expression for the DART system parameters under the shared spectrum access paradigm to achieve the same performance as the existing single-dish RAS with a radio quiet zone. This provides guidance in the DART system design. These contributions are reported in our conference paper [25]. Additional contributions with respect to [25] are described below. We develop efficient combination of astronomical source power estimations between the single dish RAS and the DART system. Furthermore, cooling is a major source of operation cost for RAS. Given finite cooling power, we propose a dynamic cooling temperature approach to allocate the cooling power according to ambient temperatures and CWC traffic statistics. We investigate both perfect and imperfect temperature information scenarios for the cooling power allocation problem and a neat solution is found by using an alternating optimization approach. The numerical and simulation results illustrate performance of the proposed DART system as well as effects of ADC resolution on the RAS signal power estimation performance.

This chapter is organized as follows. Section 4.2 introduces the RAS signal power estimation method and the system structure for both single-dish RAS and the DART system. We investigate the performance statistics of the astronomical signal power estimation under various ADC resolutions in Section 4.3. Then in Section 4.4, we provide their closed-form

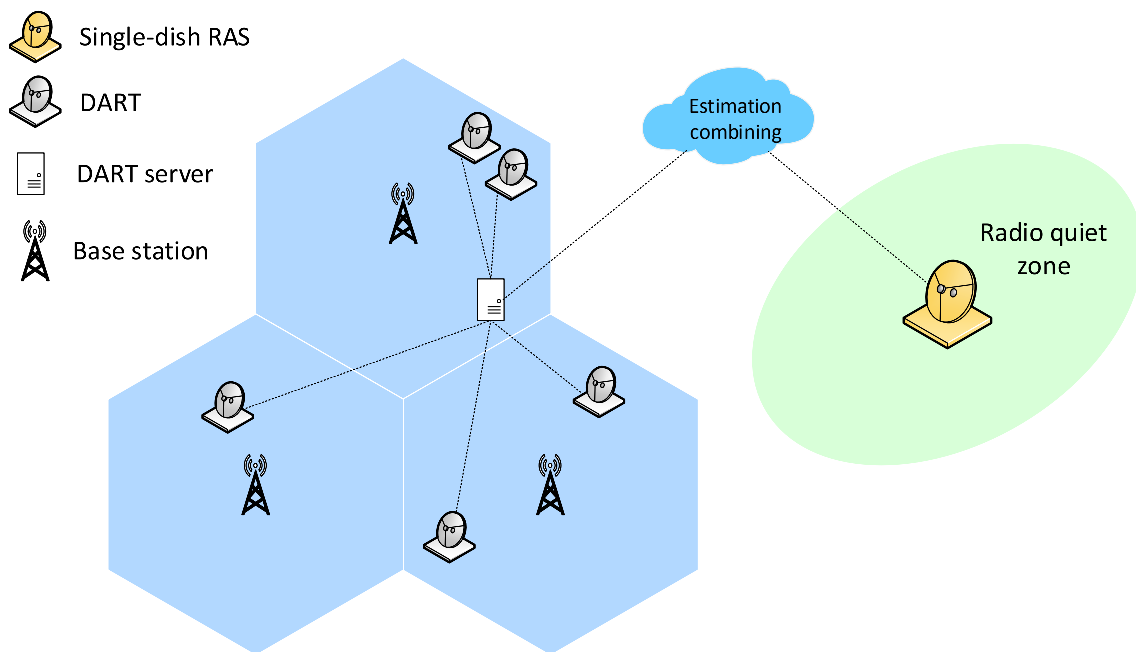

Figure 4.1: Geometric structure of the DART system and the single-dish RAS

approximations and investigate their relationships to the accurate (non-closed-form) expressions derived in the previous section. Next, Section 4.5 presents performance of the DART system under the three-phase spectrum sharing paradigm of [52] with reference to that of the single-dish RAS in a radio quiet zone. In Section 4.6, the cooling power allocation problem is proposed and investigated. Finally, Section 4.7 concludes this chapter.

4.2 System Model

To enable growth in both CWC and RAS services, we consider the shared spectrum access paradigm proposed in [52] where CWC and RAS can coexist geographically and spectrally. Such coexistence paradigm removes the need of a radio quiet zone around each radio telescope and hence we propose to exploit it by introducing several radio telescopes within the radio coverage zones of CWC, which we term distributed auxiliary radio telescopes (DARTs). An illustration of the proposed system is shown in Fig. 4.1. The RAS data from each DART are saved at a central station or a cloud database center and hence cross-processing of data from different DARTs can be easily done. This coexistence paradigm could also promote emergence of DARTs set up by public institutions, private groups or individuals with strong interest in RAS.

In the shared spectrum access approach of [52], a time frame of duration τ_{f}, which consists of n_{f} subframes of duration τ_{sf} each, is divided into three phases, namely CWC only phase of duration τ_{CWC} (n_{CWC} subframes), CWC+RAS phase of duration $\tau_{\mathrm{CWC+RAS}}$ ($n_{\mathrm{CWC+RAS}}$ subframes) and RAS only phase of duration τ_{RAS} (n_{RAS} subframes), as is shown in Fig. 4.2. The first phase is only for CWC while the last phase is only for RAS, thus providing RFI-free spectrum access to both systems. The second phase is used to absorb different propagation delays of CWC cells, and it could allow transmissions in some CWC cells, some practical testing of RFI cancellation schemes, or fine tuning of the shared spectral access paradigm [64]. The durations of the three phases can be adjusted based on the spectrum access needs, the CWC traffic statistics, and practical fine tuning results of the shared spectrum access parameters. An example of spectrum access duration adaptation on an hourly basis[1] based on the CWC traffic statistics was presented in [52]. For our DART deployment, to guarantee RFI-free observation, we only use the RAS only phase for the DART. The implication of this shared spectrum access is the reduction of the RAS observation time of a DART if compared to the RAS in a radio quiet zone. However, more DARTs can be used to recover the loss in the RAS observation time or to get even a larger effective observation time. In the following, we will develop signal model, estimator, and performance analysis in a general sense based on the number of observation samples and the noise variance. By substituting appropriate values for those parameters, one can obtain the results for the the considered scenario or paradigm.

[1]computed and designed in advance, thus no online adaptation is needed.

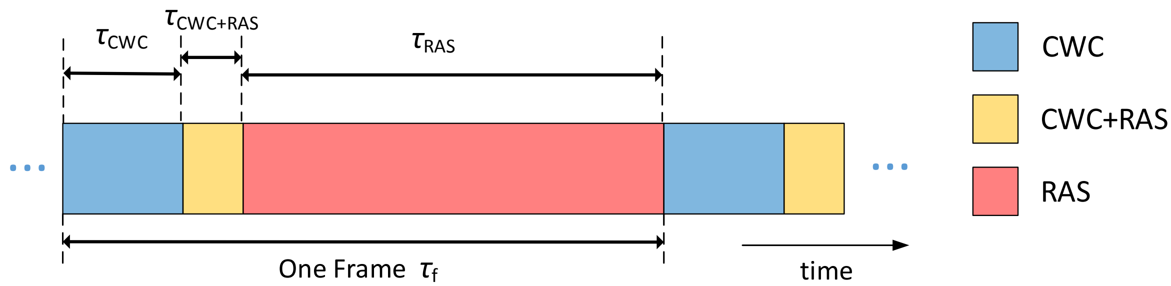

Figure 4.2: Frame structure of the three-phase spectrum sharing paradigm where the durations of the phases could be different at different hours[52]

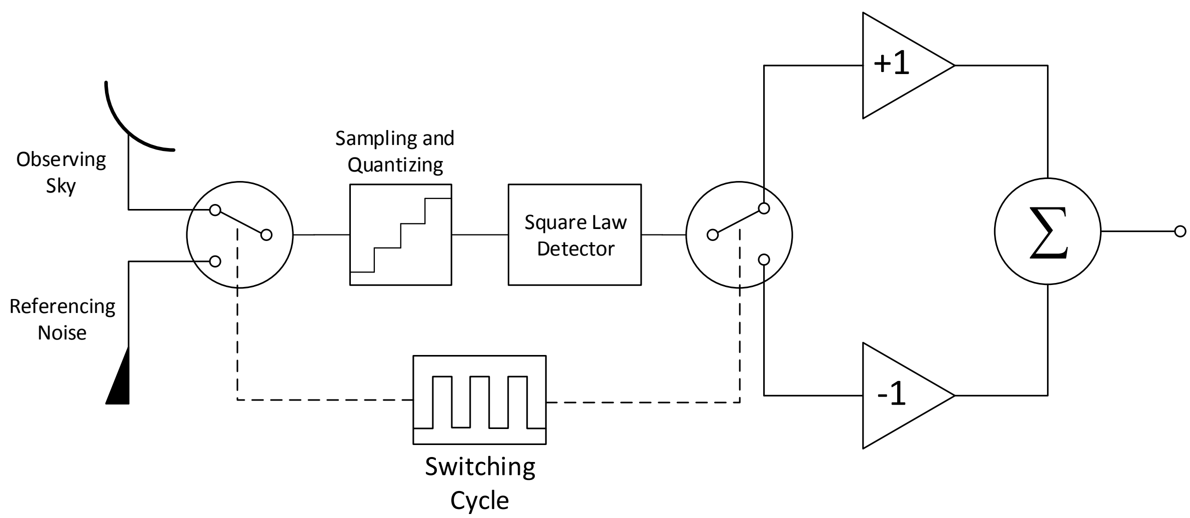

Figure 4.3: RAS receiver structure with noise referencing

The DART system aims to receive the radio waves of the astronomical radio sources, which are commonly modeled to be zero mean complex Gaussian distributed[8, 29, 34, 68], and then estimate the power of the source in terms of the radiation power. However, the received radio wave sent from the source is significantly weaker than the additive thermal noise at the receiver. To mitigate the noise impact and achieve unbiased power estimation as accurate as possible, we apply a noise referring approach called Dicke switching (see [81, Fig.4.8] and [13]) where the receivers switch the observations between astronomical source and the inner noise generating source[2]. The simplified receiver structure is shown in Fig. 4.3. Each antenna element samples and quantizes the astronomical radio signal corrupted with additive thermal noise and the reference thermal noise in a time-division manner. Next, the quantized samples are squared by the detector to obtain the signal power. Subtracting the averaged reference samples' power from the averaged noise corrupted astronomical samples' power, the power of astronomical radio signal is estimated. To be specific, for the DART system with M antenna elements (telescopes), we assume the received astronomical source signal at each antenna is circular symmetric complex Gaussian (CSCG) distributed with zero mean and variance σ_{s}^2. We also assume the additive thermal noise at each antenna is distributed as zero mean CSCG with the same variance σ_{n}^2. Therefore, the nth samples of the received astronomical source signal, the noise involved in astronomical observation and the referencing noise at the ith antenna are represented as $s_{\mathrm{t}}^i(n)$, $n_{\mathrm{t}}^i(n)$ and $n_{\mathrm{r}}^i(n)$, respectively, where $i \in \{1, ..., M\}$. We assume that the received signals are independent over different samples. Besides, the quantization errors of the nth sample at the ith antenna are $e_{\mathrm{t}}^i(n)$ and $e_{\mathrm{r}}^i(n)$ for astronomical observation and noise referencing, respectively. Correspondingly, the quantized samples are represented as

$$y_{\mathrm{t}}^i(n) \triangleq s_{\mathrm{t}}^i(n) + n_{\mathrm{t}}^i(n) + e_{\mathrm{t}}^i(n) \tag{4.1}$$

$$y_{\mathrm{r}}^i(n) \triangleq n_{\mathrm{r}}^i(n) + e_{\mathrm{r}}^i(n) \tag{4.2}$$

where $s_{\mathrm{t}}^i(n) \sim \mathcal{CN}(0, \sigma_{\mathrm{s}}^2)$ and $n_{\mathrm{t}}^i(n), n_{\mathrm{r}}^i(n) \sim \mathcal{CN}(0, \sigma_{\mathrm{n}}^2)$. Assuming we have a fixed observation time with a fixed sampling frequency, which corresponds to $2L$ samples, it can be shown that the most accurate power estimation is achieved asymptotically if we allocate L samples for astronomical observation and L samples for referencing when the following two criteria are satisfied, 1) negligible quantization error and 2) $\frac{\sigma_{\mathrm{s}}^2}{\sigma_{\mathrm{n}}^2} \to 0$. The proof is provided

[2]Other noise referencing approaches can also be applied.

in Section IV. By applying this result, the output estimated source power is

$$\rho_{\text{array}} = \frac{1}{ML} \sum_{i=1}^{M} \sum_{n=1}^{L} \left\{ |y_{\text{t}}^{i}(n)|^2 - |y_{\text{r}}^{i}(n)|^2 \right\}. \tag{4.3}$$

Since there is only one antenna element in the single-dish system, it can be regarded as a special case of the array system. Assuming we have in total $2N$ samples and allocate N samples for astronomical observation and another N samples for noise referencing, the output estimated source power is

$$\rho_{\text{single}} = \frac{1}{N} \sum_{n=1}^{N} \left\{ |y_{\text{t}}(n)|^2 - |y_{\text{r}}(n)|^2 \right\} \tag{4.4}$$

where $y_{\text{t}}(n)$ and $y_{\text{r}}(n)$ represent the quantized samples for astronomical observation and noise referencing of single-dish RAS, respectively.

Suppose the hourly based resource adaptation of [52] is applied and the three phases (see Fig. 4.2) at hour l have per-frame durations $\tau_{\text{CWC},l}$ ($n_{\text{CWC},l}$ subframes), $\tau_{\text{CWC+RAS},l}$ ($n_{\text{CWC+RAS},l}$ subframes) and $\tau_{\text{RAS},l}$ ($n_{\text{RAS},l}$ subframes), respectively, and $\tau_{\text{CWC},l}+\tau_{\text{CWC+RAS},l}+\tau_{\text{RAS},l} = \tau_{\text{f}}$. The total number of frames per hour is $N_{\text{f/hour}} = 3600/\tau_{\text{f}}$. Suppose the sampling frequency is $2B$ for RAS and the RAS signal power estimation is done based on K hours $\{l_k : k = 1, \cdots, K\}$. Then the number of samples available for a single DART is $2L = 2B \sum_{k=1}^{K} \tau_{\text{RAS},l_k} N_{\text{f/hour}}$ while that for the conventional single-dish RAS, since the spectrum is not shared, is $2N = 2BK\tau_{\text{f}} N_{\text{f/hour}}$. Obviously, as $\sum_{k=1}^{K} \tau_{\text{RAS},l_k} < K\tau_{\text{f}}$, the RAS observation time for DARTs is smaller than that for the single-dish RAS with radio quiet zones. However, under the spectrum sharing paradigm, several (M) telescopes can coexist with CWC and the total number of samples available is increased by M as can be seen in (4.3) for the DART system.

4.3 Performance Analysis of RAS Signal Power Estimation under Finite ADC Resolutions

In this section, we analyze the mean and variance of the estimated astronomical source power for both systems. We mainly focus on the DART system since the results are naturally applicable to the single-dish RAS by setting $M = 1$. Since the in-phase component and the quadrature-phase component of the signals are independently and identically distributed (i.i.d.), we represent the estimated power ρ_{array} as the sum of two i.i.d. parts, namely the in-phase estimated power ρ_{in} and the quadrature-phase estimated power ρ_{quad}, i.e., $\rho_{\text{array}} = \rho_{\text{in}} + \rho_{\text{quad}}$ where

$$\rho_{\text{in}} = \frac{1}{ML}\sum_{i=1}^{M}\sum_{n=1}^{L}\left(\mathfrak{Re}\{y_{\text{t}}^{i}(n)\}^2 - \mathfrak{Re}\{y_{\text{r}}^{i}(n)\}^2\right) \tag{4.5}$$

$$\rho_{\text{quad}} = \frac{1}{ML}\sum_{i=1}^{M}\sum_{n=1}^{L}\left(\mathfrak{Im}\{y_{\text{t}}^{i}(n)\}^2 - \mathfrak{Im}\{y_{\text{r}}^{i}(n)\}^2\right). \tag{4.6}$$

Given a b-bit quantizer with the quantization thresholds and quantized values being represented as $\nu_k,\ k \in \{1, \ldots, 2^b + 1\}$, and $c_k,\ k \in \{1, \ldots, 2^b\}$, respectively, the second moment of the real-part quantized sample is

$$\mathbb{E}\left[\mathfrak{Re}\{y_{\text{p}}^{i}(n)\}^2\right] = \sum_{k=1}^{2^b}\int_{\nu_k}^{\nu_{k+1}} c_k^2 f_{\text{p}}(x)dx = \sum_{k=1}^{2^b} c_k^2\left[Q(\nu_k/\sigma_{\text{p}}) - Q(\nu_{k+1}/\sigma_{\text{p}})\right] \tag{4.7}$$

where $\text{p} \in \{\text{t}, \text{r}\}$, $\sigma_{\text{t}}^2 = \frac{\sigma_{\text{s}}^2+\sigma_{\text{n}}^2}{2}$, $\sigma_{\text{r}}^2 = \frac{\sigma_{\text{n}}^2}{2}$, $f_{\text{p}}(x)$ is the Gaussian probability density function with zero mean and variance σ_{p}^2, and $Q(x) = \frac{1}{\sqrt{2\pi}}\int_x^\infty e^{-u^2/2}du$. And we have $\mathbb{E}\left[\mathfrak{Re}\{y_{\text{p}}^{i}(n)\}^2\right] = \mathbb{E}\left[\mathfrak{Im}\{y_{\text{p}}^{i}(n)\}^2\right]$. Define

$$\varphi_{\text{p}} \triangleq \sum_{k=1}^{2^b} c_k^2\left[Q(\nu_k/\sigma_{\text{p}}) - Q(\nu_{k+1}/\sigma_{\text{p}})\right], \quad \text{p} \in \{\text{t}, \text{r}\} \tag{4.8}$$

$$\phi_{\text{p}} \triangleq \sum_{k=1}^{2^b} c_k^4\left[Q(\nu_k/\sigma_{\text{p}}) - Q(\nu_{k+1}/\sigma_{\text{p}})\right], \quad \text{p} \in \{\text{t}, \text{r}\}. \tag{4.9}$$

Then, from (4.5)-(4.7), we can represent the first moment of the in-phase and quadrature-phase estimated powers as

$$\mathbb{E}[\rho_{\mathrm{in}}] = \mathbb{E}[\rho_{\mathrm{quad}}] = \varphi_{\mathrm{t}} - \varphi_{\mathrm{r}}. \tag{4.10}$$

We can also obtain their second moments $\mathbb{E}\left[\rho_{\mathrm{in}}^2\right] = \mathbb{E}\left[\rho_{\mathrm{quad}}^2\right]$ as

$$\begin{aligned}
\mathbb{E}\left[\rho_{\mathrm{in}}^2\right] = &\frac{1}{M^2L^2}\sum_{i,j=1}^{M}\sum_{n,m=1}^{L}\mathbb{E}\Big[\mathfrak{Re}\{y_{\mathrm{t}}^i(n)\}^2\mathfrak{Re}\{y_{\mathrm{t}}^j(m)\}^2 + \mathfrak{Re}\{y_{\mathrm{r}}^i(n)\}^2\mathfrak{Re}\{y_{\mathrm{r}}^j(m)\}^2 \\
&- 2\mathfrak{Re}\{y_{\mathrm{t}}^i(n)\}^2\mathfrak{Re}\{y_{\mathrm{r}}^j(m)\}^2\Big] \\
\overset{(a)}{\approx} &\frac{1}{ML}\left\{\mathbb{E}[\mathfrak{Re}\{y_{\mathrm{t}}^i(n)\}^4] + \mathbb{E}[\mathfrak{Re}\{y_{\mathrm{r}}^i(n)\}^4] - 2\mathbb{E}[\mathfrak{Re}\{y_{\mathrm{t}}^i(n)\}^2]\mathbb{E}[\mathfrak{Re}\{y_{\mathrm{r}}^i(n)\}^2]\right\} \\
&+ \frac{ML-1}{ML}\left\{\mathbb{E}\left[\mathfrak{Re}\{y_{\mathrm{t}}^i(n)\}^2\right] - \mathbb{E}\left[\mathfrak{Re}\{y_{\mathrm{r}}^i(n)\}^2\right]\right\}^2 \\
= &\frac{1}{ML}(\phi_{\mathrm{t}} + \phi_{\mathrm{r}} - 2\varphi_{\mathrm{t}}\varphi_{\mathrm{r}}) + \frac{ML-1}{ML}(\varphi_{\mathrm{t}} - \varphi_{\mathrm{r}})^2.
\end{aligned} \tag{4.11}$$

where the approximation (a) is due to the independence assumption between $y_{\mathrm{t}}^i(n)$ and $y_{\mathrm{t}}^j(n)$, $\forall i \neq j$. As the power of astronomical source is significantly less than the power of noise, the approximated expression in (4.11) is asymptotically accurate when the received SNR approaches zero. According to (4.10) and (4.11), the variance of the in-phase estimated power and that of the quadrature-phase estimate power are

$$\mathrm{Var}(\rho_{\mathrm{in}}) = \mathrm{Var}(\rho_{\mathrm{quad}}) \approx \frac{1}{ML}(\phi_{\mathrm{t}} + \phi_{\mathrm{r}} - \varphi_{\mathrm{t}}^2 - \varphi_{\mathrm{r}}^2). \tag{4.12}$$

Then, we obtain the mean and variance of the power estimation of the DART system as

$$\mathbb{E}[\rho_{\mathrm{array}}] = \mathbb{E}[\rho_{\mathrm{in}}] + \mathbb{E}[\rho_{\mathrm{quad}}] = 2(\varphi_{\mathrm{t}} - \varphi_{\mathrm{r}}) \tag{4.13}$$

$$\begin{aligned}
\mathrm{Var}(\rho_{\mathrm{array}}) &= \mathrm{Var}(\rho_{\mathrm{in}}) + \mathrm{Var}(\rho_{\mathrm{quad}}) \\
&\approx \frac{2}{ML}(\phi_{\mathrm{t}} + \phi_{\mathrm{r}} - \varphi_{\mathrm{t}}^2 - \varphi_{\mathrm{r}}^2).
\end{aligned} \tag{4.14}$$

Next, by seting $M = 1$ and substituting L with N, we also obtain the counterparts for the single-dish RAS as

$$\mathbb{E}[\rho_{\mathrm{single}}] = 2(\varphi_{\mathrm{t}} - \varphi_{\mathrm{r}}) \tag{4.15}$$

$$\mathrm{Var}(\rho_{\mathrm{single}}) = \frac{2}{N}(\phi_{\mathrm{t}} + \phi_{\mathrm{r}} - \varphi_{\mathrm{t}}^2 - \varphi_{\mathrm{r}}^2). \tag{4.16}$$

Note that (4.16) is an accurate expression since for $M = 1$, (4.11) involves no approximation. Besides, as the effect of the noise variance is embedded in $\varphi_{\rm t}$, $\varphi_{\rm r}$, $\phi_{\rm t}$, and $\phi_{\rm r}$, a different noise variance could affect the mean and variance of the RAS power estimate. We also notice that for both the DART system and the single-dish RAS, the mean values of the output power estimates are the same as long as they have identical quantizer settings and the same noise variance. However, the variances of the output power estimates have different factors ML versus N. This clearly shows that although $L < N$, the DART system can improve its performance by increasing the number of antennas, M.

4.4 Approximate Closed-Form Analysis

The means and variances of the estimated powers derived in (4.13) - (4.16) are not in closed forms. To have better insights, in this section, we develop approximated closed-form representations, assuming the received sample is independent from the quantization error.

For the DART system, conditioning on the quantization errors, the received signals are regarded as being i.i.d. CSCG distributed over all the antennas, i.e.,

$$\begin{aligned} y_{\rm t}^i(n)|e_{\rm t}^i(n) &\sim \mathcal{CN}(e_{\rm t}^i(n), \sigma_{\rm n}^2 + \sigma_{\rm s}^2) \\ y_{\rm r}^i(n)|e_{\rm r}^i(n) &\sim \mathcal{CN}(e_{\rm r}^i(n), \sigma_{\rm n}^2). \end{aligned} \tag{4.17}$$

To prove the asymptotically optimal sample partitioning mentioned in Section II, we start the analysis by using different numbers of samples for source observation and noise referencing, namely, L_1 and L_2. Then, the estimated source power is rewritten as

$$\rho_{\rm array} = \frac{1}{ML_1} \sum_{i=1}^{M} \sum_{n=1}^{L_1} |y_{\rm t}^i(n)|^2 - \frac{1}{ML_2} \sum_{i=1}^{M} \sum_{n=1}^{L_2} |y_{\rm r}^i(n)|^2 \tag{4.18}$$

where $L_1 + L_2 = 2L$. For compactness, we define conditional terms $Z_{\rm t}^i \triangleq \sum_{n=1}^{L_1} |y_{\rm t}^i(n)|e_{\rm t}^i(n)|^2$ and $Z_{\rm r}^i \triangleq \sum_{n=1}^{L_2} |y_{\rm r}^i(n)|e_{\rm r}^i(n)|^2$ and note that both terms, $Z_{\rm t}^i$ and $Z_{\rm r}^i$, are non-central chi-square random variables with the means and variances being represented as

$$\mathbb{E}(Z_{\mathrm{t}}^i) = L_1(\sigma_{\mathrm{n}}^2 + \sigma_{\mathrm{s}}^2) + \sum_{n=1}^{L_1} |e_{\mathrm{t}}^i(n)|^2 \tag{4.19}$$

$$\mathbb{E}(Z_{\mathrm{r}}^i) = L_2\sigma_{\mathrm{n}}^2 + \sum_{n=1}^{L_2} |e_{\mathrm{r}}^i(n)|^2 \tag{4.20}$$

$$\mathrm{Var}(Z_{\mathrm{t}}^i) = L_1(\sigma_{\mathrm{n}}^2 + \sigma_{\mathrm{s}}^2)^2 + 2(\sigma_{\mathrm{n}}^2 + \sigma_{\mathrm{s}}^2) \sum_{n=1}^{L_1} |e_{\mathrm{t}}^i(n)|^2 \tag{4.21}$$

$$\mathrm{Var}(Z_{\mathrm{r}}^i) = L_2\sigma_{\mathrm{n}}^4 + 2\sigma_{\mathrm{n}}^2 \sum_{n=1}^{L_2} |e_{\mathrm{r}}^i(n)|^2. \tag{4.22}$$

Therefore, conditioning on the quantization error set $\mathcal{E} = \{(e_{\mathrm{t}}^i(n), e_{\mathrm{r}}^i(m)) : i = 1, ..., M,\ n = 1, ..., L_1,\ m = 1, ..., L_2\}$, the estimated power is

$$\rho_{\mathrm{array}}|\mathcal{E} = \frac{1}{ML_1} \sum_{i=1}^{M} Z_{\mathrm{t}}^i - \frac{1}{ML_2} \sum_{i=1}^{M} Z_{\mathrm{r}}^i. \tag{4.23}$$

From (4.19) to (4.22), the mean and variance of $\rho_{\mathrm{array}}|\mathcal{E}$ are

$$\mu_{\rho|\mathcal{E}} = \mathbb{E}[\rho_{\mathrm{array}}|\mathcal{E}] = \sigma_{\mathrm{s}}^2 + \frac{\mathrm{MSE_t}(L_1)}{ML_1} - \frac{\mathrm{MSE_r}(L_2)}{ML_2} \tag{4.24}$$

$$\mathrm{Var}(\rho_{\mathrm{array}}|\mathcal{E}) = \frac{1}{ML_1}(\sigma_{\mathrm{n}}^2 + \sigma_{\mathrm{s}}^2)^2 + \frac{1}{ML_2}\sigma_{\mathrm{n}}^4 + \frac{2(\sigma_{\mathrm{n}}^2 + \sigma_{\mathrm{s}}^2)}{M^2L_1^2}\mathrm{MSE_t}(L_1) + \frac{2\sigma_{\mathrm{n}}^2}{M^2L_2^2}\mathrm{MSE_r}(L_2) \tag{4.25}$$

where $\mathrm{MSE_p}(L) \triangleq \sum_{i=1}^{M} \sum_{n=1}^{L} |e_{\mathrm{p}}^i(n)|^2,\ \mathrm{p} \in \{\mathrm{t}, \mathrm{r}\}$.

Now, we are able to find the asymptotically optimal sample numbers L_1 and L_2 based on the conditional variance in (4.25). Under the condition that the quantization error is negligible and $\frac{\sigma_{\mathrm{s}}^2}{\sigma_{\mathrm{n}}^2} \to 0$, we have

$$\lim_{e_{\mathrm{t}}^i, e_{\mathrm{r}}^i, \frac{\sigma_{\mathrm{s}}^2}{\sigma_{\mathrm{n}}^2} \to 0} \mathrm{Var}(\rho_{\mathrm{array}}) = \lim_{e_{\mathrm{t}}^i, e_{\mathrm{r}}^i, \frac{\sigma_{\mathrm{s}}^2}{\sigma_{\mathrm{n}}^2} \to 0} \mathrm{Var}(\rho_{\mathrm{array}}|\mathcal{E}) = \frac{\sigma_{\mathrm{n}}^4}{ML_1} + \frac{\sigma_{\mathrm{n}}^4}{ML_2}. \tag{4.26}$$

With the fact that $L_1 + L_2 = 2L$, the minimum variance, i.e., the minimum of (4.26), is achieved when

$$L_1 = L_2 = L. \tag{4.27}$$

This solution also applies to the single-dish RAS. Next, substituting (4.27) to (4.24), the approximated mean μ_ρ of the estimated astronomical source power is

$$\mu_\rho = \mathbb{E}[\mu_{\rho|\mathcal{E}}] \approx \sigma_{\mathrm{s}}^2 \tag{4.28}$$

where the approximation is due to the assumption $\mathbb{E}\left[|e_{\mathrm{t}}^i(n)|^2\right] = \mathbb{E}\left[|e_{\mathrm{r}}^i(n)|^2\right]$ since $\sigma_{\mathrm{s}}^2 \ll \sigma_{\mathrm{n}}^2$. Substituting (4.27) to (4.25), we obtain the variance $\sigma_{\mathrm{array}}^2$ of the estimated astronomical source power as

$$\begin{aligned}\sigma_{\mathrm{array}}^2 &= \mathbb{E}\left[\mathrm{Var}(\rho_{\mathrm{array}}|\mathcal{E})\right] + \mathrm{Var}(\mathbb{E}[\rho_{\mathrm{array}}|\mathcal{E}]) \\ &\approx \frac{2}{ML}\sigma_{\mathrm{n}}^4 + \frac{1}{ML}(2\sigma_s^2\sigma_{\mathrm{n}}^2 + \sigma_{\mathrm{s}}^4) + \frac{2}{ML}(\sigma_{\mathrm{n}}^2 + \sigma_{\mathrm{s}}^2)\mathbb{E}\left[|e_{\mathrm{t}}^i(n)|^2\right] + \frac{2}{ML}\sigma_{\mathrm{n}}^2\mathbb{E}\left[|e_{\mathrm{r}}^i(n)|^2\right] \approx \frac{2\sigma_{\mathrm{n}}^4}{ML}.\end{aligned} \tag{4.29}$$

The first approximation in (4.29) holds because

$$\mathrm{Var}(\mathbb{E}[\rho_{\mathrm{array}}|\mathcal{E}]) = \mathbb{E}\left[\sigma_{\mathrm{s}}^2 + \frac{\mathrm{MSE_t}(L)}{ML} - \frac{\mathrm{MSE_r}(L)}{ML}\right]^2 - \sigma_{\mathrm{s}}^4 \approx 0. \tag{4.30}$$

The second approximation in (4.29) is due to $\sigma_{\mathrm{s}}^2 \ll \sigma_{\mathrm{n}}^2$ and $\mathbb{E}\left[|e_{\mathrm{t}}^i(n)|^2\right] \ll \sigma_{\mathrm{n}}^2$.

Similarly, we can also obtain approximate results for the single-dish RAS. The mean value of the estimated source power is the same as (4.28) while the variance is

$$\sigma_{\mathrm{single}}^2 \approx \frac{2\sigma_{\mathrm{n}}^4}{N}. \tag{4.31}$$

Note that the approximate closed-form results correspond to the scenario with very low SNR (relevant for RAS) and negligible quantization error. Thus, comparison between the exact expressions from the previous section and the approximate ones will reveal the effect of quantization errors on the RAS power estimation performance. To observe this, we define their ratios as the normalized performance metrics as

$$\gamma_\mu \triangleq \frac{\mathbb{E}[\rho_{\mathrm{single}}]}{\mu_\rho} = \frac{\mathbb{E}[\rho_{\mathrm{array}}]}{\mu_\rho} \tag{4.32}$$

$$\gamma_\sigma \triangleq \frac{\mathrm{Var}(\rho_{\mathrm{single}})}{\sigma_{\mathrm{single}}^2} = \frac{\mathrm{Var}(\rho_{\mathrm{array}})}{\sigma_{\mathrm{array}}^2}. \tag{4.33}$$

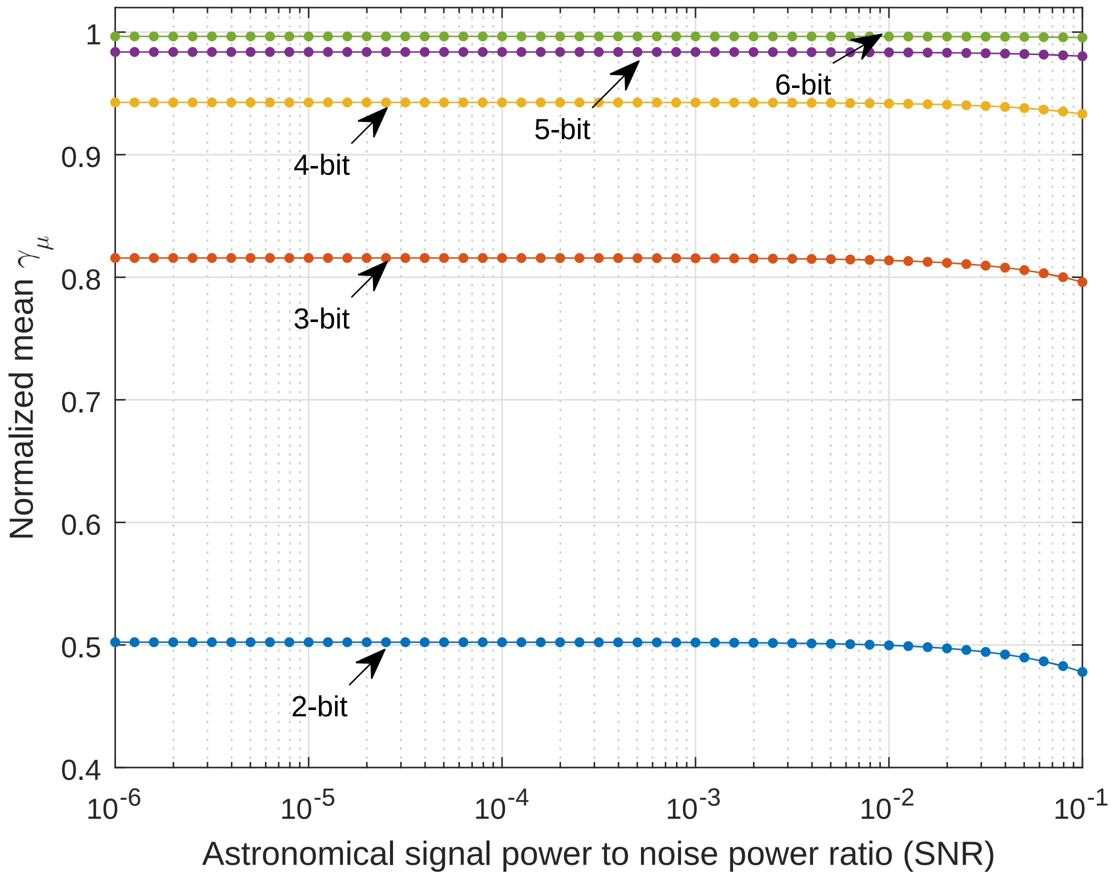

Figure 4.4: The normalized mean of RAS signal power estimation under various ADC resolutions ($\sigma_s^2 = 1,\ N$ or $L = 10^4$)

We note that the single-dish RAS and the DART system share the same term of each normalized performance metric and hence we can use variables γ_μ and γ_σ for both systems.

We present the effect of ADC resolution on the RAS power estimation performance by plotting γ_μ and γ_σ under various ADC resolutions in Fig. 4.4 and Fig. 4.5 respectively, where we apply trained Lloyd-Max quantizers corresponding to the noise variance. To verify the analytical results, we conducted Monte Carlo simulations using $\sigma_s^2 = 1$ and SNR $= -20$ dB. Table 4.1 shows the corresponding simulation results which match with the analytical

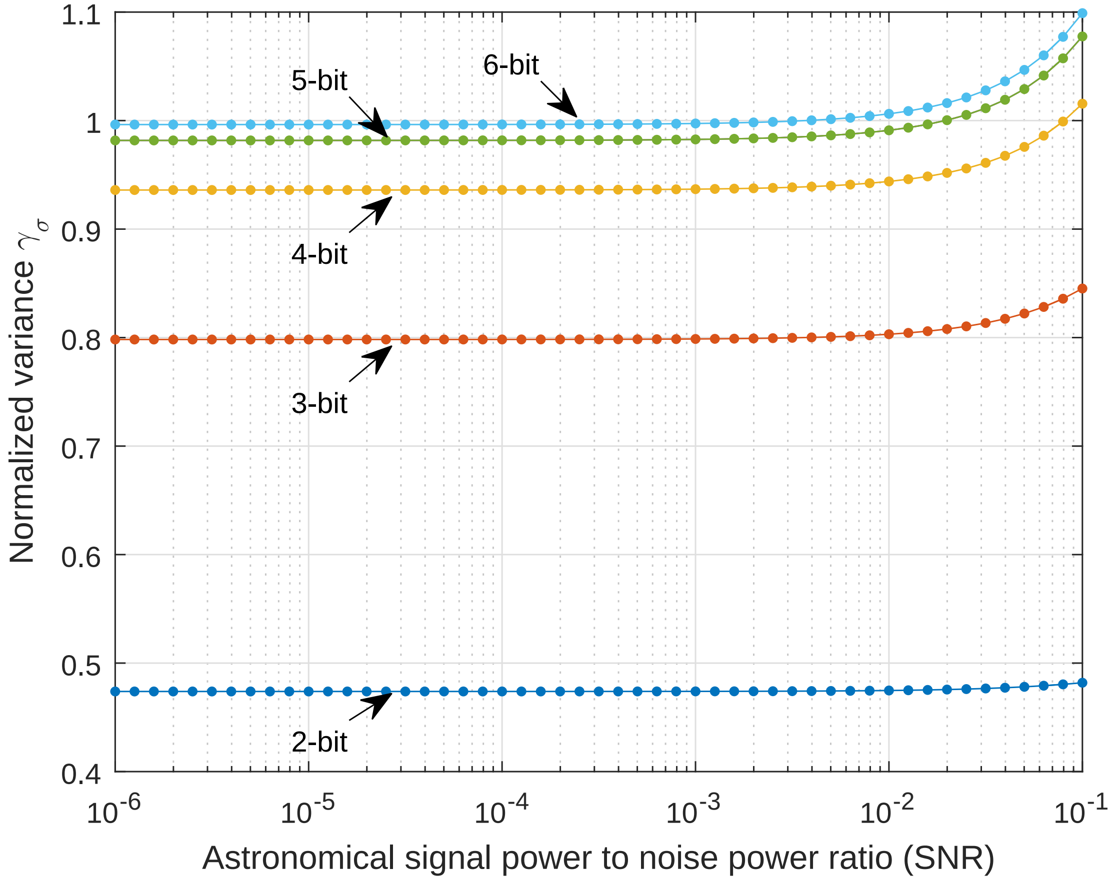

Figure 4.5: The normalized variance of RAS signal power estimation under various ADC resolutions ($\sigma_s^2 = 1,\ N$ or $L = 10^4$)

results in Fig. 4.4 and Fig. 4.5. From the results in the figures, the following observations are in order:

1. A smaller ADC resolution introduces a larger bias to the mean of the RAS power estimation.

2. To obtain approximately unbiased estimates without additional bias compensation, an ADC resolution of at least 6 bits is needed.

3. The variance of the RAS power estimation reduces with decreasing ADC resolution.

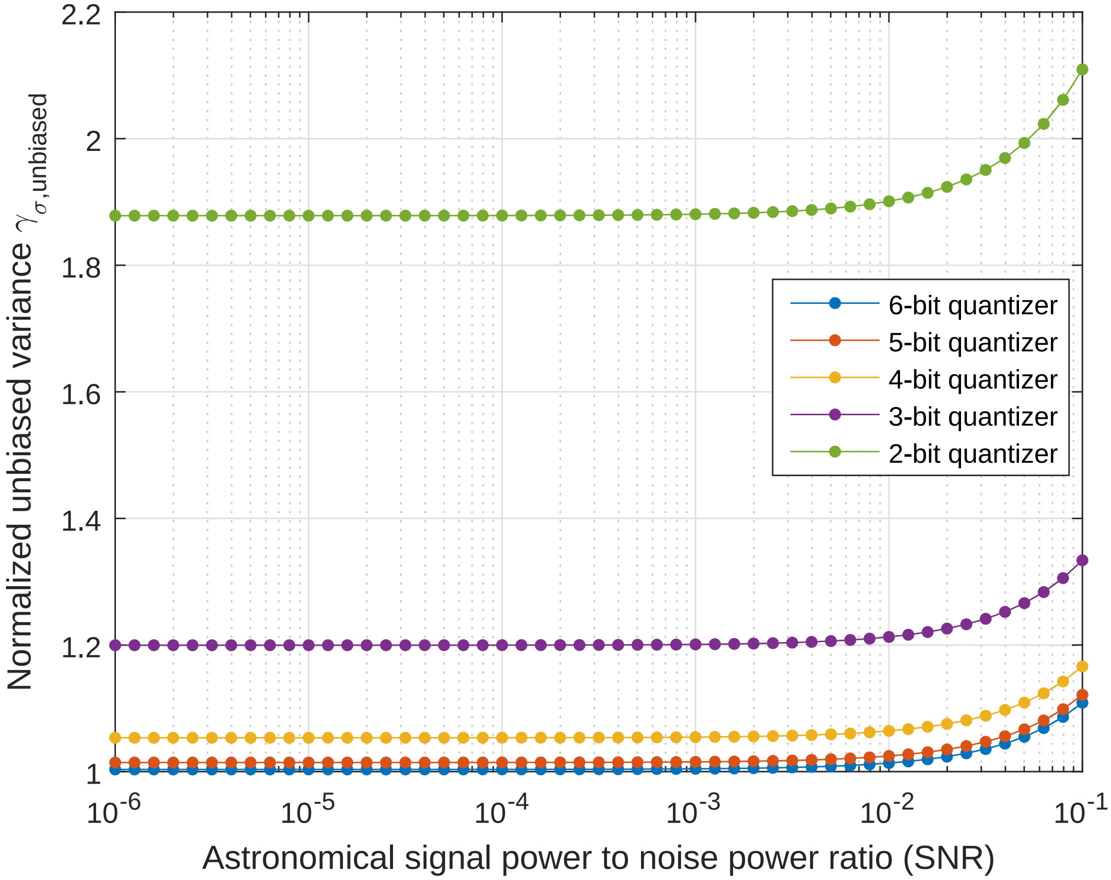

Figure 4.6: The normalized variance of RAS signal power estimation after the bias compensation ($\sigma_s^2 = 1,\ N$ or $L = 10^4$)

4. The effects of ADC resolution in terms of the estimation mean and variance are approximately constant within the typical SNR range of interest for RAS (< -20 dB). This also allows us to use a small ADC resolution (causing a bias) and then compensate the precomputed bias.

After the bias compensation (i.e., multiplying with $1/\gamma_\mu$), the variance of the unbiased RAS power estimation is given by

$$\gamma_{\sigma,\text{unbiased}} \triangleq \frac{\text{Var}(\rho_{\text{single}}/\gamma_\mu)}{\sigma^2_{\text{single}}} = \frac{\text{Var}(\rho_{\text{array}}/\gamma_\mu)}{\sigma^2_{\text{array}}} = \frac{\gamma_\sigma}{\gamma_\mu^2}. \tag{4.34}$$

It is crucial for the RAS power estimator to be unbiased and hence, (4.34) is a more meaningful metric than (4.33).

Given the two facts, first, the ADC resolution is approximately constant within the typical low SNR range, second, the mean $\mathbb{E}[\rho_{\text{single}}]$ (or $\mathbb{E}[\rho_{\text{array}}]$) and variance $\text{Var}(\rho_{\text{single}})$ (or $\text{Var}(\rho_{\text{array}})$) are proportional to their closed-form approximations μ_ρ and σ^2_{single} (or σ^2_{array}) by factor γ_μ and γ_σ respectively according to (4.32) and (4.33), we will mainly use the closed form results σ^2_{single} and σ^2_{array} in the following analysis for representation simplicity.

Fig. 4.6 presents the variance of the unbiased RAS power estimator for different ADC resolutions. We can observe that a higher ADC resolution yield a smaller variance. However, the performance saturates for ADC resolution of 6 bits or more. We also simulated 7 and 8 bits ADC resolutions and the results are indistinguishable from that of 6 bits ADC and hence they are not plotted in Fig. 4.6 for the sake of clarity of the other curves. And $\gamma_{\sigma,\text{unbiased}}$ converges to 1 as the resolution increases. As a larger ADC resolution yield a higher data rate, trade-offs can be made between data rates and estimation performance. A good choice is 6 bits ADC resolution as more bits do not yield noticeable performance improvement.

Next, we evaluate the effect of the number of antennas. With the settings that $\sigma_s^2 = 1$ and $N = 10^4$, table 4.2 shows the Monte Carlo simulation results for a 4-bit quantizer at $\text{SNR} = -20$ dB when the number of antenna elements varies. Comparing the multi-antenna results to the single antenna result in this table, we observe the following.

1. The variance of estimated power decreases by a factor around M when more antennas are combined. This illustrates a benefit of the DART system.

2. The corresponding normalized metric γ_σ, which in its approximate form in (4.14) is independent of M, slightly increases with M. This is due to the mismatch between the assumption of independence among the received signals at different antennas in the analysis and the correlation of the received signals across antennas due to the same

Table 4.1: Comparison of Different Quantization Resolutions

Bits	2	3	4	5	6
Simulated Mean (or γ_μ)	0.4967	0.8106	0.9447	0.9746	0.9986
Simulated Variance	0.9528	1.6165	1.8896	1.9871	2.0089
Corresponding γ_σ	0.4764	0.8082	0.9448	0.9936	1.0044

astronomical signal in the simulation. In other words, the difference between γ_σ for $M > 1$ and γ_σ for $M = 1$ implies how accurate the approximation in (4.14) is, and the results show good accuracy.

3. The simulation result of γ_μ does not grow with M (thus, maintaining unbiased estimation for different values of M) since the signal correlation does not affect the mean of the estimated power.

4.5 Combination and Performance Comparison between DART and the Single-Dish RAS

Here, we evaluate the performance of the DART by incorporating specifics of the coexistence paradigm and then compare it with the performance of the single-dish RAS (the isolation paradigm). Recall the system parameters for the shared spectrum access described in Section II. Suppose the hourly allocation of the number of subframes per frame to the three phases is pre-designed according to the CWC traffic statistics as in [52]. Let $n_{\text{array},l}$ denote the number of subframes per frame allocated to the DARTs for the lth hour. An example of available observation intervals of DART in terms of $n_{\text{array},l}$ is shown by a line curve in Fig. 4.8 based on the system setting in [52]. DART is allocated with longer (shorter) observation intervals during hours with lower (higher) CWC average traffic loads. Thus, the hourly estimation performance of DART would vary as well.

The number of samples at hour l for DART is given by $2L_l = 2Bn_{\text{array},l}\tau_{\text{sf}}N_{\text{f/hour}}$ while that for the single-dish RAS is $2N = 2Bn_{\text{f}}\tau_{\text{sf}}N_{\text{f/hour}}$ at any hour. Then, the variances of the

Table 4.2: Comparison of Different Numbers of Antenna Elements

M	1	10	50
Simulated Mean (or γ_μ)	0.9447	0.9421	0.9402
Simulated Variance	1.8896	0.1896	0.0386
Corresponding γ_σ	0.9448	0.9481	0.9640

estimated powers in (4.29) and (4.31) for hour l are

$$\sigma^2_{\text{array},l} \approx \frac{2\sigma^4_{\text{n}}}{MBn_{\text{array},l}\tau_{\text{sf}}N_{\text{f/hour}}}, \quad l = 1, \ldots, 24 \tag{4.35}$$

$$\sigma^2_{\text{single},l} = \frac{2\sigma^4_{\text{n}}}{Bn_{\text{f}}\tau_{\text{sf}}N_{\text{f/hour}}}, \quad l = 1, \ldots, 24. \tag{4.36}$$

As hourly based signal power estimates denoted by $\{\rho_{\text{array},l}\}$ have different accuracies, if the desired power estimation needs to be computed over K hours $(l_1, \ldots, l_K)$, we can apply the best linear unbiased estimation [35] to combine the K estimates as

$$\rho_{\text{array}} = \sum_{k=1}^{K} \beta_k \rho_{\text{array},l_k} \tag{4.37}$$

where

$$\beta_k = \frac{1/\sigma^2_{\text{array},l_k}}{\sum_{n=1}^{K} 1/\sigma^2_{\text{array},l_n}} \tag{4.38}$$

minimizes the variance of combined estimation $\sigma^2_{\text{array}} \approx \sum_{k=1}^{K} \beta_k^2 \sigma^2_{\text{array},l_k}$, under the unbiased constraint $\sum_{k=1}^{K} \beta_k = 1$. The approximation is due to the assumption that observations in different hours are regarded to be independent since noise is the dominant received signal. Thus, the corresponding estimator variance for the DART system is given by

$$\sigma^2_{\text{array}} \approx \frac{2\sigma^4_{\text{n}}}{MB\tau_{\text{sf}}N_{\text{f/hour}}\sum_{k=1}^{K} n_{\text{array},l_k}}. \tag{4.39}$$

We notice that (4.39) indicates this estimator variance is equivalent to the variance achieved by averaging all the samples in K hours. Meanwhile, we denote r as the ratio of the total resources allocated over the above K hours between CWC and RAS, i.e., $r = \frac{\sum_{k=1}^{K} n_{\text{CWC},l_k}}{\sum_{k=1}^{K} n_{\text{RAS},l_k}}$. A comparison between the variance achieved by the BLUE approach and the variance achieved

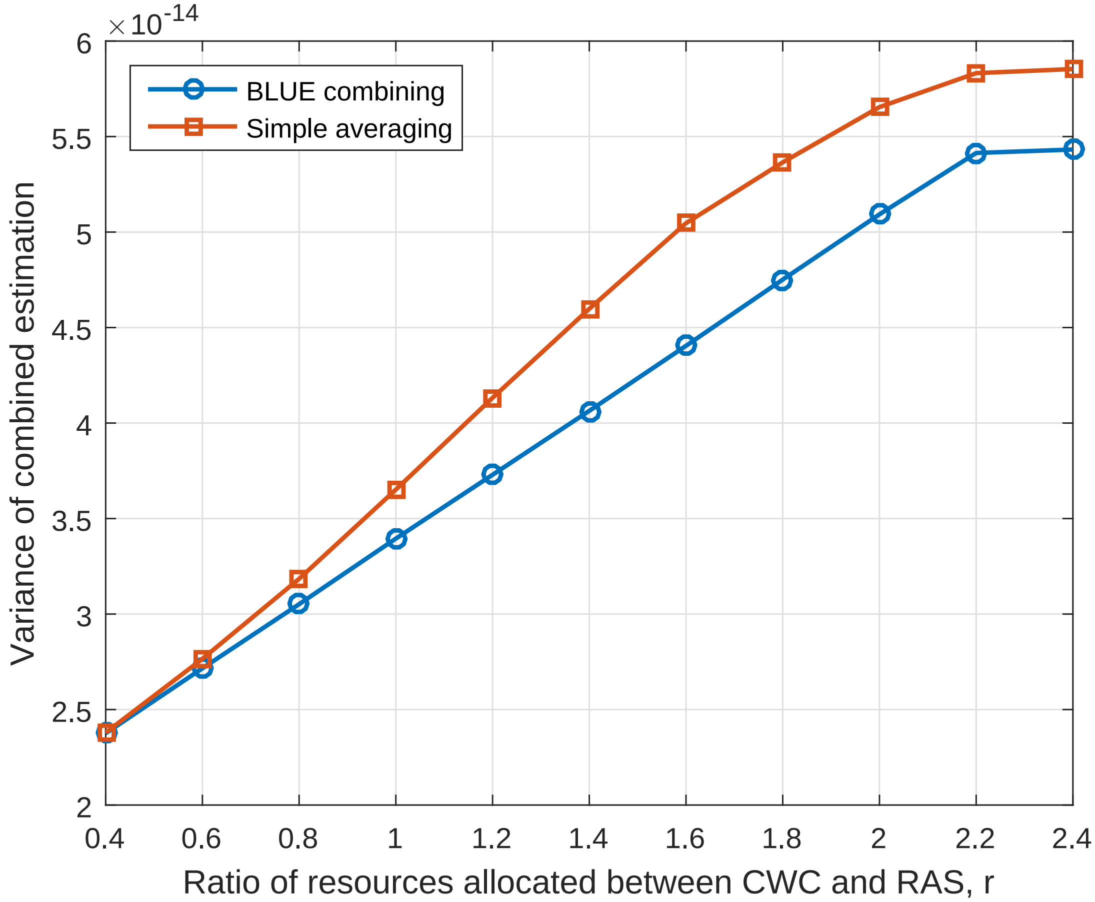

Figure 4.7: Comparison between BLUE and simple averaging

by simply averaging $\sigma^2_{\text{array},l}, l = 1, \ldots, K$ for different values of the resource ratio r is shown in Fig. 4.7. It can be observed that in a feasible range of the ratio r, the BLUE combining approach always outperforms the simple averaging method in terms of the variance of the estimated power.

For the single-dish RAS, we can simply average the K estimates as $\rho_{\text{single}} = \sum_{k=1}^{K} \frac{\rho_{\text{single},l_k}}{K}$ and the corresponding variance is

$$\sigma^2_{\text{single}} = \frac{2\sigma^4_{\text{n}}}{KBn_{\text{f}}\tau_{\text{sf}}N_{\text{f/hour}}}. \tag{4.40}$$

In a typical deployment of the shared spectrum access, a fixed minimum subframe value of $n_{\text{CWC+RAS},l} = n_{\text{CWC+RAS}}$ would be used across time to maximize the spectrum utilization.

Then, with $\eta \triangleq (n_\mathrm{f} - n_\mathrm{CWC+RAS})/n_\mathrm{f}$, we have

$$\sum_{k=1}^{K} n_{\mathrm{array},l_k} = \frac{\eta K}{1+r} n_\mathrm{f}. \tag{4.41}$$

Next, from (4.39), (4.40) and (4.41), we obtain

$$\sigma^2_\mathrm{array} \approx \frac{1+r}{M\eta} \sigma^2_\mathrm{single}. \tag{4.42}$$

The above equation shows the relationship between the estimation accuracy of the DART system and that of the single-dish RAS. For example, to achieve the same or better estimation performance than the single-dish RAS with a radio quiet zone, the DART system needs at least $M = \lceil \frac{1+r}{\eta} \rceil$ antenna elements coexisting with CWC.

To compare the estimation accuracy of different systems, we assume that $\sigma^2_\mathrm{n} = 1,\ K = 24,\ B = 500\mathrm{MHz},\ \tau_\mathrm{sf} = 38.5\mu s,\ n_\mathrm{f} = 44,\ n_\mathrm{CWC+RAS} = 4$ and $r = 1.25$. Then, we have $M = \lceil \frac{1+r}{\eta} \rceil = 3$. Next, according to the $n_{\mathrm{array},l}$ curve shown in Fig. 4.8, the variances of estimated power in each hour are computed and also presented in Fig. 4.8. Clearly, the variance of estimated power of the DART system is inversely proportional to the number of allocated subframes while the single-dish RAS's variance remains a constant value. Combining all the estimates by the best linear unbiased estimation, we find the corresponding variances for the DART system and the single-dish RAS are $\sigma^2_\mathrm{array} = 3.82 \times 10^{-14}$ and $\sigma^2_\mathrm{single} = 4.63 \times 10^{-14}$, respectively. Therefore, with enough numbers of DARTs, the DART system can outperform the single-dish RAS in terms of overall estimation accuracy even though it may have worse performance in some estimation periods.

Furthermore, instead of using the single-dish RAS and the DART system separately, we combine the DART system with the single-dish RAS so that the overall performance can be enhanced. In this scenario, the two systems observe the same astronomical source from different locations and the DART is regarded as an auxiliary system which provides additional observation samples. In particular, since the astronomical signal is significantly

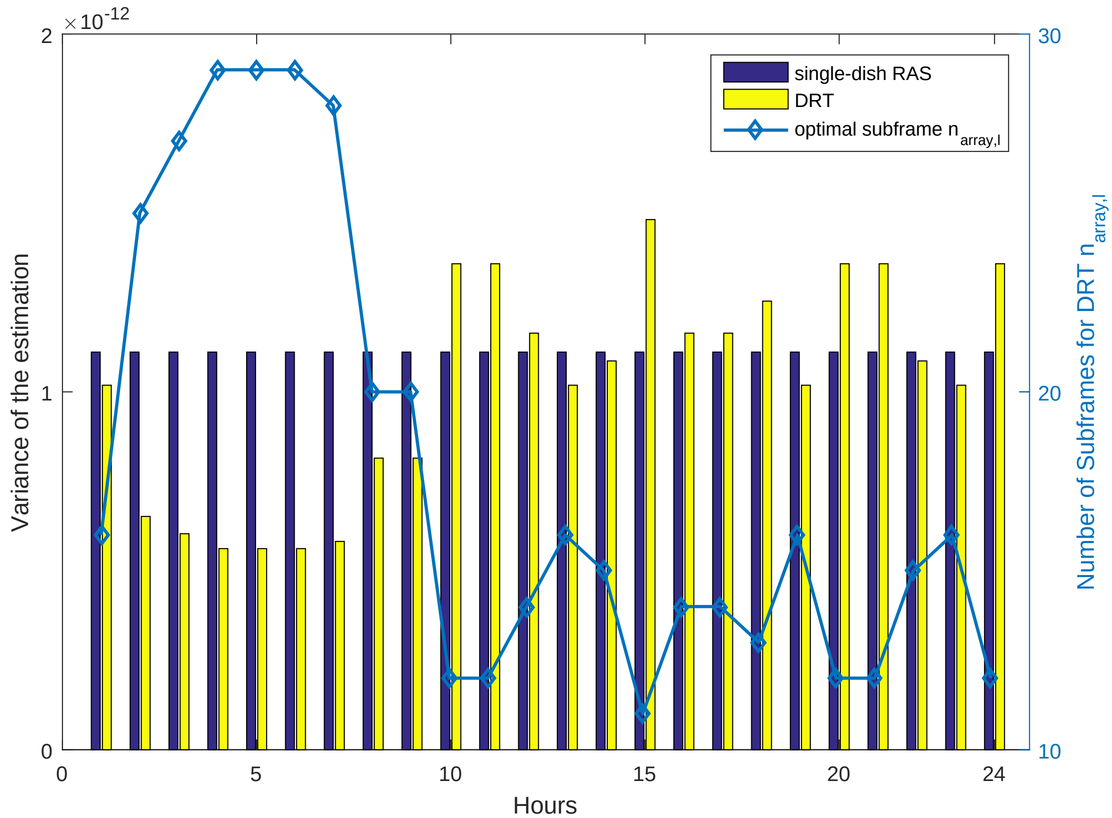

Figure 4.8: Accuracy performance comparison and optimal subframe numbers

weaker than the noise, we assume the estimated astronomical powers of both systems are uncorrelated, i.e., ρ_{single} and ρ_{array} are uncorrelated. According to the BLUE approach, the combined estimation is

$$\bar{\rho} = \theta\rho_{\text{single}} + (1-\theta)\rho_{\text{array}} \tag{4.43}$$

where $\theta = \frac{\sigma^2_{\text{array}}}{\sigma^2_{\text{single}}+\sigma^2_{\text{array}}}$. Therefore, the variance of combined estimation is

$$\bar{\sigma}^2 = \frac{\sigma^2_{\text{single}}\sigma^2_{\text{array}}}{\sigma^2_{\text{single}}+\sigma^2_{\text{array}}}. \tag{4.44}$$

Specifically, applying previous system settings, $\sigma^2_{\text{array}} = 3.82\times10^{-14}$ and $\sigma^2_{\text{single}} = 4.63\times10^{-14}$, we have $\bar{\sigma}^2 = 2.09\times10^{-14}$, which implies with the assistance of a 3-DART system, the single-dish RAS estimation variance can be reduced by more than half.

4.6 Average Performance Under Cooling Power Constraint

The accuracy of radio astronomical observation is largely dependent on the noise level of the receiver. To achieve higher observation accuracy, noise should be mitigated as much as possible. A common physical method is cooling the hardware down to an acceptable low temperature since thermal noise is the most dominant noise in the receiver. The cooling process consumes a significant part of energy of the whole radio astronomy telescope [24] which motivates us to investigate the power efficiency of the DART system.

4.6.1 DART Performance Analysis

In this section, we consider that K astronomical observations to the same object are conducted hourly and aim to minimize the estimation variance based on the K observation periods. Since the cooling process consumes a substantial part of energy, we propose an dynamic cooling power allocation approach to optimize the cooling temperature under a total cooling power constraint.

The noise variance at hour l_k can be represented in terms of noise temperature T_{l_k} as

$$\sigma^2_{\mathrm{n},l_k} = \kappa T_{l_k} B \tag{4.45}$$

where $\kappa = 1.3807 \times 10^{-23}$ is the Boltzmann constant and B is the noise bandwidth. With (4.35) and (4.45), the variances of estimated power are given as

$$\sigma^2_{\mathrm{array},l_k} = \frac{2(\kappa T_{l_k} B)^2}{M B n_{\mathrm{array},l_k} \tau_{\mathrm{sf}} N_{\mathrm{f/hour}}} = \frac{\alpha T^2_{l_k}}{M n_{\mathrm{array},l_k}} \tag{4.46}$$

where constant $\alpha = \frac{2\kappa^2 B}{\tau_{\mathrm{sf}} N_{\mathrm{f/hour}}}$. Furthermore, the average variance of the estimated powers in K hours is $\frac{1}{K}\sum_{k=1}^{K} \frac{\alpha T^2_{l_k}}{M n_{\mathrm{array},l_k}}$.

According to (4.46), in order to achieve a desired variance of the estimation, radio astronomical receivers should be cooled down to certain low temperatures to mitigate the thermal noise. Lower temperature results in higher estimation accuracy but also indicates higher power consumption. Thus, given a certain amount of power and the time varying nature of the ambient temperature, dynamically allocating the power to optimize the cooling temperature will be more preferable than the conventional approach which maintains a fixed temperature.

Assuming an idealized scenario where there is no thermodynamic loss, the second law of thermodynamics connects the minimum required power P_{MIN} to cool down a surface from ambient temperature T_{amb} to a desired temperature T_0 in the form of Carnot equation [3],

$$P_{\mathrm{MIN}} = \frac{T_{\mathrm{amb}} - T_0}{T_0} \cdot Q_0 \tag{4.47}$$

where Q_0 is called cooling capacity[3] [3].

In the following parts of this section, we assume that 1) the DARTs observes the same astronomical source signal for K hours, 2) both the CWC traffic statistics and the ambient temperature (statistics) vary hourly and are known in advance, 3) the receiver's temperature can be cooled down from ambient temperature T_{amb,l_k} to any achievable temperature T_{l_k} in hour l_k, 4) the system has a constant cooling capacity Q_0, and 5) all the K observations are combined linearly with weighting parameter β_k to improve the estimation performance. Thus, the variance of the combined estimation is written as

$$\sigma^2_{\mathrm{array}} = \sum_{k=1}^{K} \beta_k^2 \sigma^2_{\mathrm{array},l_k}. \tag{4.48}$$

Then, our problem is formulated as a joint optimization problem over the weighting parameters $\{\beta_k\}$ and the feasible cooling temperatures $\{T_{l_k}\}$ under the total cooling power

[3] Cooling capacity is the measure of a cooling system's ability to remove heat [11].

constraint,

$$
\begin{aligned}
\text{(P0):} \quad & \min_{\{T_{l_k}\},\ \{\beta_k\}} && \sum_{k=1}^{K} \beta_k^2 \frac{\alpha T_{l_k}^2}{M n_{\text{array},l_k}} \\
& \text{s.t.} && \sum_{k=1}^{K} \left(\frac{T_{\text{amb},l_k}}{T_{l_k}} - 1 \right) Q_0 \le P \\
& && T_{\min} \le T_{l_k} \le T_{\text{amb},l_k} \\
& && \sum_{k=1}^{K} \beta_k = 1, \quad \beta_k \ge 0
\end{aligned}
\tag{4.49}
$$

where $T_{\min}$ is the minimum achievable receiver temperature of the cooling system and P is the sum of available cooling powers over K hours for an antenna. We also note that in the second constraint of (4.49), the upper bound T_{amb,l_k} can be replaced by any feasible maximum temperature constraint smaller than the ambient temperature.

(P0) is convex over either $\{T_{l_k}\}$ or $\{\beta_k\}$ if the other optimization variable is fixed. Therefore, we apply an alternating optimization approach to iteratively find the optimal values of $\{T_{l_k}\}$ and $\{\beta_k\}$. Specifically, let $\left(T_{l_k}^{(n)}, \beta_k^{(n)}\right)$ denote the solutions at the nth iteration, the solution of (P0) can be obtained by alternatively solving the following two convex optimization problems,

$$
\begin{aligned}
\text{(P1-1):} \quad \{T_{l_k}^{(n)}\} = \arg & \min_{\{T_{l_k}\}} && \sum_{k=1}^{K} \left(\beta_k^{(n-1)}\right)^2 \frac{\alpha T_{l_k}^2}{M n_{\text{array},l_k}} \\
& \text{s.t.} && \sum_{k=1}^{K} \left(\frac{T_{\text{amb},l_k}}{T_{l_k}} - 1 \right) Q_0 \le P \\
& && T_{\min} \le T_{l_k} \le T_{\text{amb},l_k}
\end{aligned}
\tag{4.50}
$$

and

$$
\begin{aligned}
\text{(P1-2):} \quad \{\beta_k^{(n)}\} = \arg & \min_{\{\beta_k \ge 0\}} && \sum_{k=1}^{K} \beta_k^2 \frac{\alpha \left(T_{l_k}^{(n)}\right)^2}{M n_{\text{array},l_k}} \\
& \text{s.t.} && \sum_{k=1}^{K} \beta_k = 1.
\end{aligned}
\tag{4.51}
$$

The solution to (P1-2) can be easily obtained as

$$\beta_k^{(n)} = \frac{1/\pi_k^{(n)}}{\sum_{l=1}^{K} 1/\pi_l^{(n)}} \tag{4.52}$$

where $\pi_k^{(n)} \triangleq \frac{\alpha(T_{l_k}^{(n)})^2}{M n_{\text{array},l_k}}$. Next, we can state the following propositions.

Proposition 3. *The approach of alternatively solving (P1-1) and (P1-2) is convergent.*

Proof. Since both (P1-1) and (P1-2) are convex optimization problems, this approach can be regarded as a special case of the two-block Gauss-Seidel method whose convergence is proved in [21]. □

Proposition 4. *Defining $\omega_{l_k} \triangleq \frac{T_{\text{amb},l_k}}{T_{l_k}}$, the following two optimization problems have the same solution in terms of the cooling temperatures $\{T_{l_k}\}$: i) Alternatively solving (P1-1) and (P1-2), and ii) (P2) which is constructed as*

$$\begin{aligned} \text{(P2):} \quad \max_{\{\omega_{l_k}\}} \quad & \sum_{k=1}^{K} \frac{n_{\text{array},l_k}}{T_{\text{amb},l_k}^2} \omega_{l_k}^2 \\ \text{s.t.} \quad & \sum_{k=1}^{K} \omega_{l_k} \leq \tilde{P} \\ & 1 \leq \omega_{l_k} \leq \frac{T_{\text{amb},l_k}}{T_{\min}} \end{aligned} \tag{4.53}$$

where $\tilde{P} = \frac{P}{Q_0} + K$.

Proof. The proof is in Appendix 4.8. □

With the above two propositions, the solution to (P2) in terms of cooling temperature $\{T_{l_k}\}$ can also be a near-optimal solution to the original problem (P0). Besides, the corresponding weighting parameter $\{\beta_k\}$ can be computed by (4.52).

Remark 1. We can verify that (P2) is not a convex optimization problem since it aims to maximize a convex objective function. However, the two linear constraints fortunately allow us to use simple power allocation algorithms to find the optimal solution. Specifically, the first constraint of (P2) bounds the sum of ω_{l_k}'s while the second constraint provides the lower and upper bounds for individual ω_{l_k}'s. On the other hand, the objective function is a weighted sum of $\omega_{l_k}^2$ where the non-negative weighting parameter is known. Therefore, it is always preferable to allocate as much power[4] to the l_ith element ω_{l_i} where $i = \arg\max_k \frac{n_{\text{array},l_k}}{T_{\text{amb},l_k}^2}$. Thus the optimal solution to (P2) for the kth hour can only be chosen from three values, the minimum value 1, the maximum value $\frac{T_{\text{amb},l_k}}{T_{\text{min}}}$ or a certain value between the minimum and maximum. Likewise, only one of the three cooling temperatures at the kth hour can be selected as the solution to alternatively solving (P1-1) and (P1-2), and they are the minimum achievable cooling temperature T_{min}, the ambient temperature T_{amb,l_k} (i.e., the cooling system is off) and a certain temperature between these two (i.e., when the residual cooling power is not enough to cool the receiver down to T_{min}).

Now, we summarize the above analysis for solving (P2) in Algorithm 1.

Algorithm 1 Cooling Power Allocation Algorithm for Problem (P2)

Initialize residual power $\tilde{P}' = \tilde{P}$, index set $\mathcal{K} = \{1, \ldots, K\}$, and $\omega_{l_k} = 0,\ \forall k \in \mathcal{K}$,
Allocate 1 unit of power to satisfy the lower bound constraint of $\{\omega_{l_k}\}$ in the second constraint of (P2), renew the residual power $\tilde{P}' = \tilde{P} - K$;
while $\tilde{P}' > 0$ **do**
    Next power allocation index $i = \arg\max_{k\in\mathcal{K}} \frac{n_{\text{array},l_k}}{T_{\text{amb},l_k}^2}$, renew $\mathcal{K} = \mathcal{K}\backslash i$;
    if $\tilde{P}' \geq \frac{n_{\text{array},l_i}}{T_{\text{amb},l_i}^2} - 1$ **then**
        $\omega_{l_i} = \frac{n_{\text{array},l_i}}{T_{\text{amb},l_i}^2}$, renew $\tilde{P}' = \tilde{P}' - (\frac{n_{\text{array},l_i}}{T_{\text{amb},l_i}^2} - 1)$;
    else
        $\omega_{l_i} = \tilde{P}' + 1$, renew $\tilde{P}' = 0$;
    end if
end while
Output $\{\omega_{l_k}\}_{k=1}^K$.

Adopting previous simulation settings together with $Q_0 = 100W$, $T_{\text{min}} = 60$ Kelvin, T_{amb,l_k} = 286, 285, 283, 282, 279, 282, 285, 289, 292, 295, 297, 298, 299, 300, 301, 302, 301, 300, 297,

[4]Here we regard $\tilde{P}$ as power for convenience since $\tilde{P}$ is a power related factor.

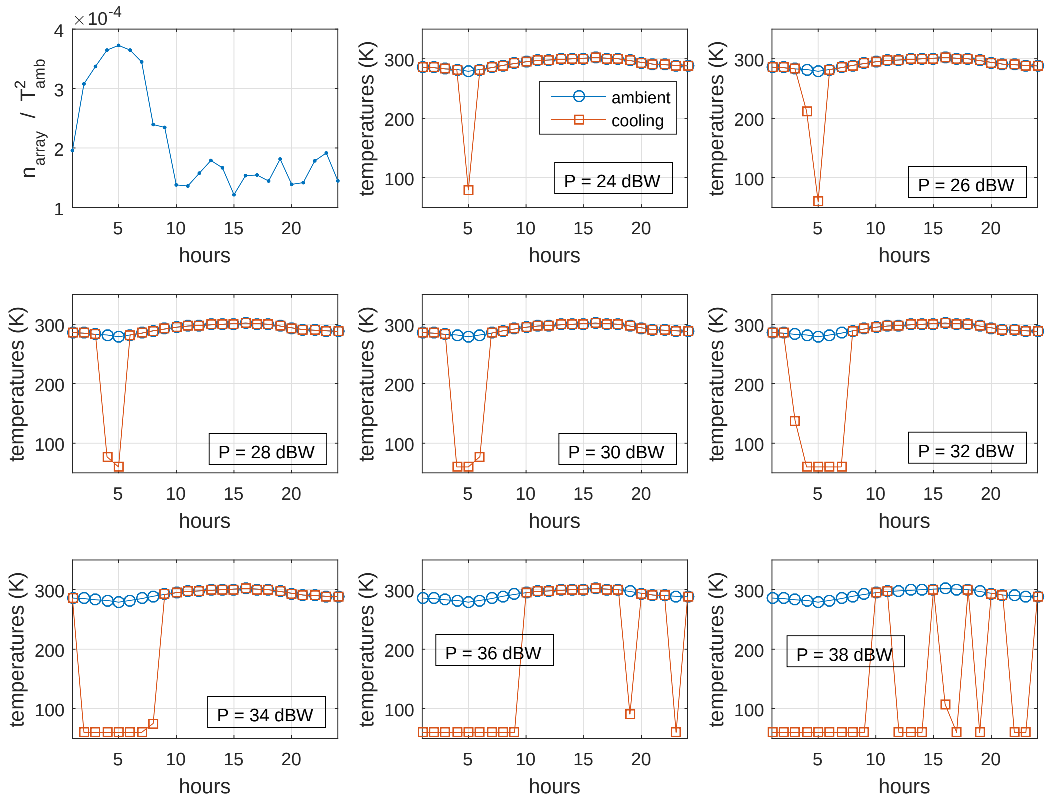

Figure 4.9: Solutions of cooling power allocation in terms of cooling temperatures.

294, 291, 290, 289, 288 Kelvin for $k = 1, \ldots, 24$, the cooling temperatures solutions under different cooling power constraints are shown in Fig. 4.9. To be specific, the first figure in Fig. 4.9 shows the value of $\frac{n_{\text{array},l_k}}{T^2_{\text{amb},l_k}}$ for $k = 1, \ldots, 24$. We can see as the total cooling power P increases from 24dBW to 38dBW, the number of times the minimum cooling temperature is achieved increases. And the cooling power allocation priority corresponds to the increasing order of $\frac{n_{\text{array},l_k}}{T^2_{\text{amb},l_k}}$.

To evaluate the power saving of this approach, we can consider the scenario where the DART system always maintains a fixed cooling temperature T_{array} no less than $T_{\min}$ by default setting and has the same cooling power constraint P at each antenna. Then, similar to the first constraint of (4.49), we have

$$\sum_{k=1}^{K}\left(\frac{T_{\mathrm{amb},l_k}}{T_{\mathrm{array}}}-1\right)Q_0 \leq P \tag{4.54}$$

which results in

$$T_{\mathrm{array}} \geq \max\left\{T_{\min},\ \frac{\sum_{k=1}^{K} T_{\mathrm{amb},l_k} Q_0}{P+KQ_0}\right\}. \tag{4.55}$$

Thus, the estimation variance of the DART system with a fixed cooling temperature is represented as

$$\left[\sigma^2_{\mathrm{array}}\right]_{\mathrm{fixed}} = \sum_{k=1}^{K} \beta_k^2 \sigma^2_{\mathrm{array},l_k}\Big|_{\beta_k=\frac{1}{K}} = \sum_{k=1}^{K} \frac{1}{K^2}\frac{\alpha T^2_{\mathrm{array}}}{M n_{\mathrm{array},l_k}} \tag{4.56}$$

according to (4.46). Similarly, to compare with the DART system with M antennas, the total available cooling power for single-dish RAS is set as $P_{\mathrm{single}} = MP$ and thus the minimal achievable temperature at cooling capacity Q_0 is

$$T_{\mathrm{single}} \geq \max\left\{T_{\min},\ \frac{\sum_{k=1}^{K} T_{\mathrm{amb},l_k} Q_0}{P_{\mathrm{single}}+KQ_0}\right\}. \tag{4.57}$$

Therefore, the variance of estimation for the single-dish RAS wth a fixed cooling temperature is represented as

$$\left[\sigma^2_{\mathrm{single}}\right]_{\mathrm{fixed}} = \sum_{k=1}^{K} \beta_k^2 \sigma^2_{\mathrm{single}}\Big|_{\beta_k=\frac{1}{K}} = \frac{1}{K}\frac{\alpha T^2_{\mathrm{single}}}{n_{\mathrm{f}}} \tag{4.58}$$

according to (4.40) and the relationship $\sigma_{\mathrm{n}}^2 = \kappa T_{\mathrm{single}} B$.

4.6.2 Imperfect Temperature Information

We have assumed that the ambient temperature in each hour are perfectly known for cooling power allocation. However, temperature forecasting may not be perfect and the cooling power requirement in problem (4.49) may not be satisfied if the temperature is forecast with error. In this scenario, we consider to use a probability constraint on the cooling power shortage. In other words, we suppose that the probability of the required cooling power being larger than the total available power P should be no more than ϵ. To be specific, we assume that the temperature $\mathbf{T} = [T_{\text{amb},l_1}, \ldots, T_{\text{amb},l_K}]^{\mathrm{T}}$ is Gaussian distributed, $\mathbf{T} \sim \mathcal{N}(\boldsymbol{\mu}, \boldsymbol{\Sigma})$ where the mean values are forecast temperatures $\boldsymbol{\mu} = [\bar{T}_{\text{amb},l_1}, \ldots, \bar{T}_{\text{amb},l_K}]^{\mathrm{T}}$ and the covariance is represented by a Toeplitz matrix $\boldsymbol{\Sigma}$. Then, the first constraint of (4.49) is replaced by

$$\Pr\left[\sum_{k=1}^{K}\left(\frac{T_{\text{amb},l_k}}{T_{l_k}} - 1\right) Q_0 > P\right] \leq \epsilon. \tag{4.59}$$

Defining $x_{l_k} \triangleq 1/T_{l_k}$, and $\boldsymbol{x} = [x_{l_1}, \ldots, x_{l_K}]^{\mathrm{T}}$, the constraint is rewritten as $\Pr\left(\mathbf{T}^{\mathrm{T}}\boldsymbol{x} > \tilde{P}\right) \leq \epsilon$. Since $\mathbf{T}^{\mathrm{T}}\boldsymbol{x} \sim \mathcal{N}(\boldsymbol{\mu}^{\mathrm{T}}\boldsymbol{x}, \|\boldsymbol{\Sigma}^{\frac{1}{2}}\boldsymbol{x}\|_2)$, (4.59) is further represented as a second order cone constraint

$$\boldsymbol{\mu}^{\mathrm{T}}\boldsymbol{x} + Q^{-1}(\epsilon)\|\boldsymbol{\Sigma}^{\frac{1}{2}}\boldsymbol{x}\|_2 \leq \tilde{P} \tag{4.60}$$

where $Q^{-1}(\cdot)$ is the inverse function of the Q function. Therefore, the average performance optimization problem under imperfect temperature information is formulated as the following problem

$$\begin{aligned}
\text{(P3):} \quad \min_{\boldsymbol{x},\ \{\beta_k\}} \quad & \sum_{k=1}^{K} \beta_k^2 \frac{\alpha}{M n_{\text{array},l_k} x_{l_k}^2} \\
\text{s.t.} \quad & \boldsymbol{\mu}^{\mathrm{T}}\boldsymbol{x} + Q^{-1}(\epsilon)\|\boldsymbol{\Sigma}^{\frac{1}{2}}\boldsymbol{x}\|_2 \leq \tilde{P} \\
& \frac{1}{\bar{T}_{\text{amb},l_k}} \leq x_{l_k} \leq \frac{1}{T_{\min}} \\
& \sum_{k=1}^{K} \beta_k = 1, \quad \beta_k \geq 0.
\end{aligned} \tag{4.61}$$

We can observe that the modified power constraint will be reduced to the original power constraint in (4.49) if the temperatures are perfectly forecast as all elements in the covariance $\boldsymbol{\Sigma}$ would be zero. For the same power constraint, larger covariance or tighter probability constraint can result in smaller $\{x_{l_k}\}$ and therefore larger estimation variance. Likewise, the proposed alternating approach can be used to solve (P3). However, since the total cooling power constraint of (P3) is modified due to the uncertainty of ambient temperatures, the proposed power allocation strategy in Algorithm 1 is not applicable. To handle this problem, we use the convex optimization toolbox CVX[20]. Defining the variance of the nth iteration as $\left[\sigma^2_{\text{array}}\right]^{(n)} \triangleq \sum_{k=1}^{K} \beta_k^{(n)\,2} \frac{\alpha (T_{l_k}^{(n)})^2}{M n_{\text{array},l_k}}$ and the counterpart of (P1-1) for the imperfect temperature forecast scenario as

$$\begin{aligned}
\text{(P3-1):} \quad \{x_{l_k}^{(n)}\} = \arg\min_{x_{l_k}} \quad & \sum_{k=1}^{K} \left(\beta_k^{(n-1)}\right)^2 \frac{\alpha}{M n_{\text{array},l_k} x_{l_k}^2} \\
\text{s.t.} \quad & \boldsymbol{\mu}^{\mathrm{T}} \boldsymbol{x} + Q^{-1}(\epsilon) \|\boldsymbol{\Sigma}^{\frac{1}{2}} \boldsymbol{x}\|_2 \le \tilde{P} \\
& \frac{1}{\bar{T}_{\text{amb},l_k}} \le x_{l_k} \le \frac{1}{T_{\min}},
\end{aligned} \tag{4.62}$$

the following Algorithm 2 illustrates the proposed alternating optimization approach to find the cooling power allocation solution for imperfect temperature information scenarios.

Algorithm 2 Cooling Power Allocation Algorithm for Problem (P3)

1: Initialize $n = 1,\ \varepsilon > 0,\ \left[\sigma^2_{\text{array}}\right]^{(0)} = 2\varepsilon,\ \left[\sigma^2_{\text{array}}\right]^{(1)} = \varepsilon$ and $\beta_k^{(0)} = \frac{1}{K},\ \forall k = 1, \ldots, K$
2: **while** $\left(\left[\sigma^2_{\text{array}}\right]^{(n-1)} - \left[\sigma^2_{\text{array}}\right]^{(n)}\right) / \left[\sigma^2_{\text{array}}\right]^{(n-1)} > \varepsilon$ **do**
3: Solve (P3-1) with CVX, obtain $\{x_{l_k}^{(n)}\}$ and compute $\beta_k^{(n)} = \frac{1/\pi_k^{(n)}}{\sum_{l=1}^{K} 1/\pi_l^{(n)}},\ k = 1, \ldots, K;$
4: n = n + 1;
5: **end while**
6: Output $\{x_{l_k}^{(n)}\}$ and $\{\beta_k^{(n)}\}$.

4.6.3 Combination of DART and Single-dish RAS

We have proposed a DART system that can achieve an estimation performance as accurate as the conventional single-dish RAS. Now, a two-step approach to combine the observations of both systems is proposed to achieve the minimum estimation variance of the K independent observations: 1) the single-dish RAS and the DART system observe separately where the DART apply the estimation optimization approach to obtain the minimum estimation variance and the optimal cooling temperature, 2) the best linear unbiased estimation (BLUE) approach is applied to combine the two estimations from the single-dish RAS and the DART system, using the same weighting parameter θ as shown in (4.43). In particular, since the astronomical signal is significantly weaker than the noise, we assume the estimated signals

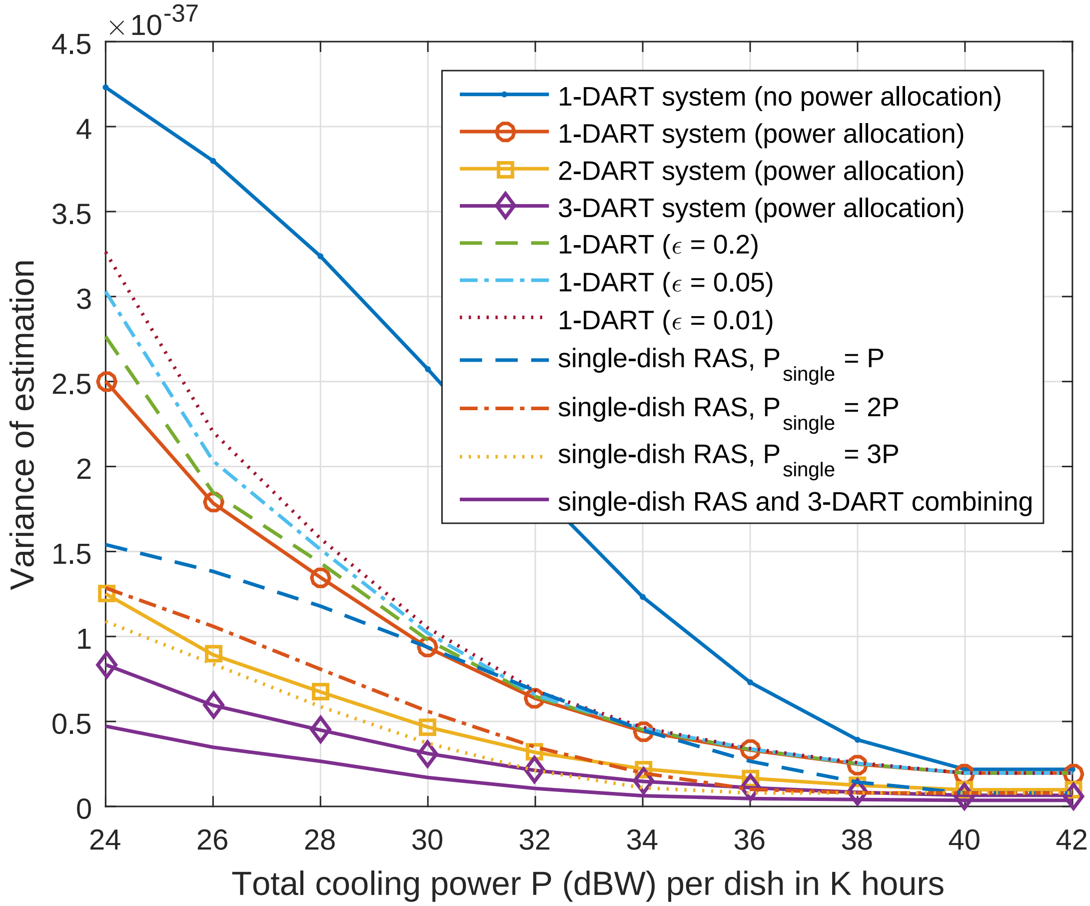

Figure 4.10: Radio astronomical signal power estimation variance comparison among different strategies.

of both systems are uncorrelated, i.e., ρ_{single} and ρ_{array} are uncorrelated. Using the BLUE approach as in (4.43), the variance of combined estimated power is $\bar{\sigma}^2 = \frac{\sigma^2_{\text{single}}\sigma^2_{\text{array}}}{\sigma^2_{\text{single}}+\sigma^2_{\text{array}}}$, where $\sigma^2_{\text{array}} = \sum_{k=1}^{K} \beta_k^2 \sigma^2_{\text{array},l_k}$ is the variance of estimation for the DART system according to (4.48).

4.6.4 Simulations

In the simulation, we set that 1) for the imperfect temperature information scenarios, $\bar{T}_{\text{amb},l_k} = 286,\ 285,\ 283,\ 282,\ 279,\ 282,\ 285,\ 289,\ 292,\ 295,\ 297,\ 298,\ 299,\ 300,\ 301,\ 302,$

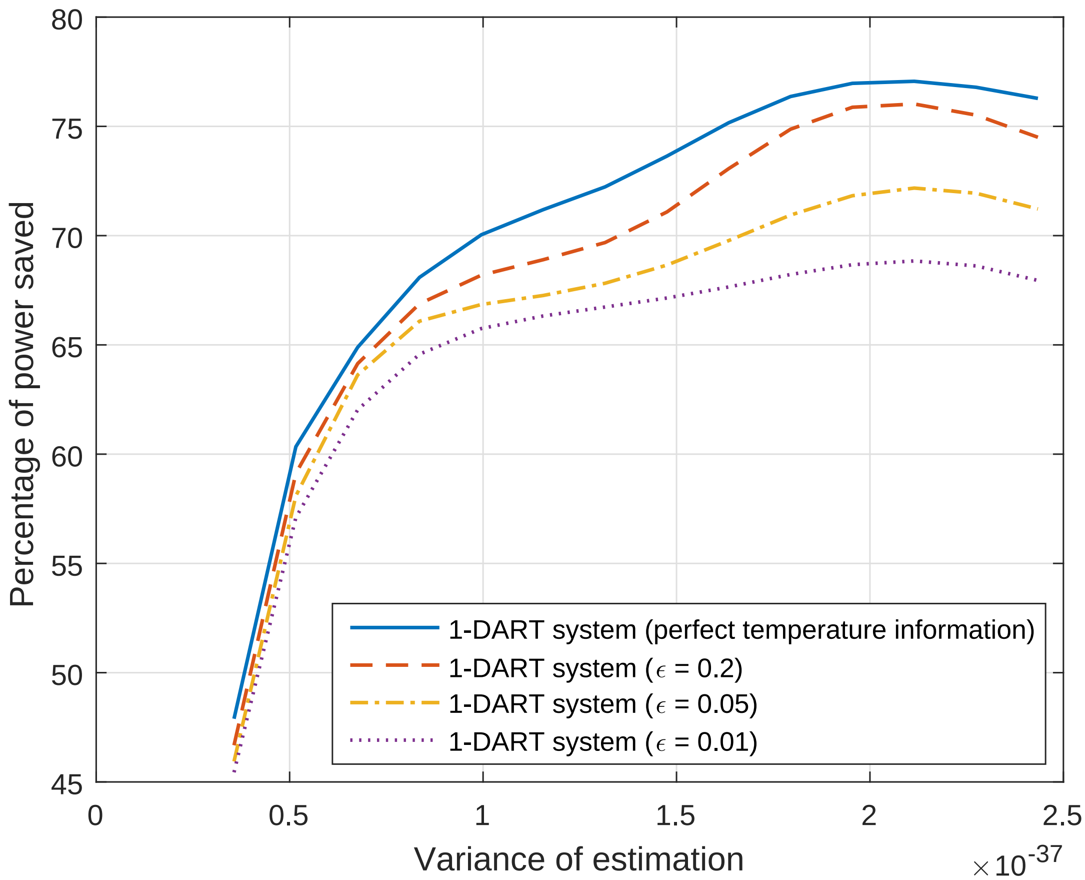

Figure 4.11: Percentage of power saved by the proposed dynamic cooling power allocation.

301, 300, 297, 294, 291, 290, 289, 288 Kelvin for $k = 1, \ldots, 24$ respectively, $\mathbf{\Sigma}$ is set to be a symmetric Toeplitz matrix whose first row is [30, 28.75, 27.5, 26.25, 25, 23.75, 22.5, 21.25, 20, 18.75, 17.5, 16.25, 15, 15.75, 16.5, 17.25, 18, 18.75, 19.5, 20.25, 21, 21.75, 22.5, 23.25] and 2) for the perfect temperature information scenarios, $T_{\text{amb},l_k} = \bar{T}_{\text{amb},l_k}$, $\forall k$. Other settings are adopted from previous sections and are the same for both scenarios.

Fig. 4.10 compares the average variances of the radio astronomical signal power estimation achieved by different strategies, namely, DART without power allocation (fixed cooling temperature), DART with power allocation, DART with power allocation and imperfect ambient temperature information, single-dish RAS (fixed cooling temperature) and the combination of single-dish RAS and DART's estimation, under total cooling power constraint for each DART ranging from 24 dBW to 42 dBW. First of all, we can observe that with increasing cooling power, the variances decrease, and the difference between DART with power allocation and that without power allocation converges to a very small value since all the temperatures are cooled down to the minimum achievable temperature $T_{\min}$. We also mention that the gap between the variance achieved by the two strategies cannot converge to zero since the proposed power allocation contains the BLUE procedure which outperforms the simple averaging of the different estimations, unless n_{array,l_k} is a constant for K hours. This implies our proposed power allocation strategy preforms better, especially in a power limited regime. Also, the relationship among the DART system with different numbers of antennas ($M = 1, 2, 3$) is shown in this figure. As the number of antennas increases from 1 to M, the variance reduces to $1/M$ times of the original value.

Fig. 4.10 also shows the variances achieved by single-dish RAS with the cooling power allocation strategy under different cooling power constraints. The three different P_{single} are set to compare with the DART system with different numbers of antennas. It can be observed that larger P_{single} corresponds to smaller variance. However, the decrease of the variance becomes remarkable when P_{single} increases. When $M = 1$ ($P_{\text{single}} = P$) and $M = 2$ ($P_{\text{single}} = 2P$), the variances achieved by single-dish RAS are less than those of 1-DART and 2-DART system respectively. While the number of antennas in DARTs increases to 3 ($P_{\text{single}} = 3P$), the variances of 3-DART system are less than those of single-dish RAS for most of the cooling power constraints. This observation indicates the combination of more DARTs with dynamic cooling power allocation will result in higher power efficiency than the single-dish RAS with fixed cooling temperature strategy.

Besides, the bottom curve in Fig. 4.10 shows the power estimation variance achieved by combining both the single-dish RAS ($P_{\text{single}} = 3P$) and the 3-dish DART system. Obviously, combining the observations of the two systems results in a smaller estimation variance than just applying individual system. For instance, the variance of combined estimation power is as small as half of the variance achieved by the single-dish RAS. These comparisons also imply our proposed DART system can significantly improve the accuracy performance (in terms of estimation variance) of the current RAS systems.

For imperfect ambient temperature information scenarios, three probability constraints are simulated and shown in Fig. 4.10. Compared with the scenario where ambient temperatures are perfectly forecast, the uncertainty results in higher variance, and tighter probability constraint corresponds to higher variance.

Fig. 4.11 shows the percentage of power saved by this strategy for certain achieved average variances according to the curves in Fig. 4.10. We notice that the percentage can be as high as 77 for our system settings. For imperfect temperature information scenarios, to achieve certain variances while guaranteeing a smaller probability of cooling power outage, i.e., from $\epsilon = 0.2$ to $\epsilon = 0.01$, the power saving rate decreases.

4.7 Conclusion

We have proposed a DART system to embrace the geographical and spectral coexistence between CWC and RAS, and to enhance the capability or performance of RAS. Under the time-division based shared spectrum access, not only RFI-free spectrum access is available to DART during pre-designed time slots, but also more DARTs can be deployed without requiring radio quiet zones. We have derived the theoretical performance analysis of the RAS signal power estimation under different ADC resolutions and their closed-form approximations for both the DART system without radio quiet zone and the single-dish RAS with radio quiet zone. Different ADC resolutions introduce different biases to the RAS power estimation but the bias compensation is feasible. With the bias compensation, higher ADC resolution offers the better performance in terms of estimation variance but results in higher data rate. However, the performance saturates for ADC resolution of 6 bits or more. By exploiting more DARTs, the proposed DART system can perform as accurate as (or better than) the conventional single-dish RAS.

Moreover, our proposed dynamic cooling power allocation approach for perfect temperature information scenarios results in a neat solution that always sets the receiver at the minimum cooling temperature for as many duration as possible in a precomputed order of the durations. Under our specific system settings, there is a power saving as much as 77% comparing to the previous method that simply maintains a fixed cooling temperature. Meanwhile, the proposed DART approach has higher power efficiency than the single-dish RAS when the number of antennas increases. For imperfect temperature information scenarios, our alternative optimization approach achieves similar results to those of perfect temperature information scenarios as well as significant power savings. We have also illustrated that when DART and single-dish RAS are combined, further performance improvements achieved.

4.8 Appendix Proof of proposition 4

Assuming the alternatively solving (P1-1) and (P1-2) converges at the $\bar{n}$th iteration according to Proposition 3, we have $T_{l_k}^{(\bar{n})} = T_{l_k}$. Then, substituting $\beta_k^{(n-1)} = \beta_k^{(\bar{n})} = \frac{1/\pi_k^{(\bar{n})}}{\sum_{l=1}^{K} 1/\pi_l^{(\bar{n})}}$, $\pi_k^{(\bar{n})} \triangleq \frac{\alpha(T_{l_k}^{(\bar{n})})^2}{M n_{\text{array},l_k}}$ and $T_{l_k}^{(\bar{n})} = T_{l_k}$ to the objective function of (P1-1), the objective can be simplified to

$$\min_{\{T_{l_k}\}} \quad \frac{\alpha}{M} \frac{1}{\sum_{k=1}^{K} \frac{n_{\text{array},l_k}}{T_{l_k}^2}} \tag{4.63}$$

which is equivalent to maximizing the denominator term and the problem is simplified to

$$\begin{aligned} \max_{\{T_{l_k}\}} \quad & \sum_{k=1}^{K} \frac{n_{\text{array},l_k}}{T_{l_k}^2} \\ \text{s.t.} \quad & \sum_{k=1}^{K} \left(\frac{T_{\text{amb},l_k}}{T_{l_k}} - 1 \right) Q_0 \le P \\ & T_{\min} \le T_{l_k} \le T_{\text{amb},l_k}. \end{aligned} \tag{4.64}$$

Next, substituting $T_{l_k} \triangleq \frac{T_{\text{amb},l_k}}{\omega_{l_k}}$ and $\tilde{P} = \frac{P}{Q_0} + K$ to this problem, (4.64) will be further simplified to problem (P-2) defined in the Proposition 4. In summary, beginning with the convergence condition of alternatively solving (P1-1) and (P1-2), we transfer the alternating optimization problem to a single variable optimization problem (4.64) which is equivalent to (P-2), hence, proving Proposition 4.

CHAPTER 5

CONCLUSION

We proposed, analyzed and optimized three independent systems for the next generation wireless communication and RAS. For a machine-type communication system, we developed methods 1) to enable the data aggregation of multiple tiers of MTCDs with different QoS constraints where the device densities and resource allocation parameters are jointly optimized, 2) to achieve variable tradeoffs between network utility and resource allocation fairness, 3) to maximize the weighted sum of QoEs under QoS and minimum device density constraints, and to optimize the MTCG power control strategy for randomly distributed gateways.

Instead of optimizing the resource allocation for different objectives, we analyzed a novel idea to extend the communication boundaries for a large-scale communication system using AmBC mechanism. In the new scheme, randomly distributed backscatter nodes are involved as secondary users to primary transmitter and receiver pairs. We derived the coverage probabilities for two network configuration scenarios expressed by quickly computable integrals with several system parameters. The theoretical and Monte-Carlo simulation results indicated the signal enhancing and interference effects of embedding clusters of AmBC nodes in conventional large-scale communication systems.

Besides the endless demand for spectrum in active wireless communication systems, we notice the radio astronomy society desires higher observation sensitivity and resolution for an RAS, as well as observation rights on more and more frequency bands. Thus, we proposed a DART system to enhance the performance of conventional radio telescopes and to mitigate the spectrum conflict between RAS and CWC systems. Theoretical performance analysis of the DART system with different quantization resolutions is presented. Cooling power allocation methods for DART receivers according to the ambient temperature are proposed. Furthermore, we illustrated that the combination of single-dish RAS and DART system achieves better performance. The analytical expression for the DART system parameters provide guidance in designing not only the DART system but also future radio telescope arrays, such as RAS satellites on non-geostationary orbit.

REFERENCES

[1] Afshang, M., C. Saha, and H. S. Dhillon (2017). Nearest-neighbor and contact distance distributions for Matérn cluster process. *IEEE Commun. Lett. 21*(12), 2686–2689.

[2] Akyildiz, I. F., W.-Y. Lee, M. C. Vuran, and S. Mohanty (2006). Next generation/dynamic spectrum access/cognitive radio wireless networks: A survey. *Computer networks 50*(13), 2127–2159.

[3] Alekseev, A. (2015). Basics of low-temperature refrigeration. *arXiv preprint arXiv:1501.07392*.

[4] Andrews, J. G., F. Baccelli, and R. K. Ganti (2011). A tractable approach to coverage and rate in cellular networks. *IEEE Transactions on communications 59*(11), 3122–3134.

[5] Andrews, J. G., S. Buzzi, W. Choi, S. V. Hanly, A. Lozano, A. C. Soong, and J. C. Zhang (2014). What will 5G be? *IEEE Journal on selected areas in communications 32*(6), 1065–1082.

[6] Bayat, S., Y. Li, Z. Han, M. Dohler, and B. Vucetic (2014). Distributed massive wireless access for cellular machine-to-machine communication. In *IEEE International Conference on Communications (ICC)*, pp. 2767–2772.

[7] Bharadia, D., K. R. Joshi, M. Kotaru, and S. Katti (2015). Backfi: High throughput wifi backscatter. *ACM SIGCOMM Computer Communication Review 45*(4), 283–296.

[8] Bhattacharyya, S. S., E. F. Deprettere, R. Leupers, and J. Takala (2013). *Handbook of signal processing systems*. Springer Science & Business Media.

[9] Boche, H. and M. Schubert (2009). Nash bargaining and proportional fairness for wireless systems. *IEEE/ACM Trans. Netw 17*(5), 1453–1466.

[10] Casas, P. and R. Schatz (2014). Quality of experience in cloud services: survey and measurements. *Computer Networks 68*, 149–165.

[11] Cengel, Y. A. and M. A. Boles (2002). Thermodynamics: An engineering approach. *Sea 1000*, 8862.

[12] Chowdhury, K. R. and I. F. Akyildiz (2008). Cognitive wireless mesh networks with dynamic spectrum access. *IEEE Journal on Selected Areas in Communications 26*(1).

[13] Colliander, A. et al. (2002). Noise injection radiometer test specifications and requirement. *Helsinki University of Technology*.

[14] Ding, Z., Z. Yang, P. Fan, and H. V. Poor (2014). On the performance of non-orthogonal multiple access in 5G systems with randomly deployed users. *IEEE Signal Processing Letters 21*(12), 1501–1505.

[15] ElSawy, H. and E. Hossain (2014). On stochastic geometry modeling of cellular uplink transmission with truncated channel inversion power control. *IEEE Transactions on Wireless Communications 13*(8), 4454–4469.

[16] ElSawy, H., E. Hossain, and M. Haenggi (2013). Stochastic geometry for modeling, analysis, and design of multi-tier and cognitive cellular wireless networks: A survey. *IEEE Communications Surveys & Tutorials 15*(3), 996–1019.

[17] Emerson, D. (2002). Why Single-Dish? In *Single-Dish Radio Astronomy: Techniques and Applications*, Volume 278, pp. 27–43.

[18] Fitzgerald, E., M. Pióro, and A. Tomaszewski (2018). Energy-optimal data aggregation and dissemination for the internet of things. *IEEE Internet of Things Journal*.

[19] Goldsmith, A. (2005). *Wireless communications*. Cambridge university press.

[20] Grant, M., S. Boyd, and Y. Ye (2008). CVX: Matlab software for disciplined convex programming.

[21] Grippo, L. and M. Sciandrone (2000). On the convergence of the block nonlinear Gauss–Seidel method under convex constraints. *Operations research letters 26*(3), 127–136.

[22] Guo, J., S. Durrani, X. Zhou, and H. Yanikomeroglu (2017). Massive machine type communication with data aggregation and resource scheduling. *IEEE Transactions on Communications 65*(9), 4012–4026.

[23] Haenggi, M. and R. K. Ganti (2009). Interference in large wireless networks. *Foundations and Trends in Networking 3*(2), 127–248.

[24] Hall, P. J. (2011). Power considerations for the Square Kilometre Array (SKA) radio telescope. In *General Assembly and Scientific Symposium, 2011 URSI*, pp. 1–4. IEEE.

[25] Han, D. and H. Minn (2017). Performance analysis of distributed radio telescopes under shared spectrum access paradigm. In *Global Communications Conference (GLOBECOM), IEEE*, pp. 1–7.

[26] Han, D., U. Tefek, T. J. Lim, and H. Minn (2017). Network dimensioning and radio resource management for multi-tier machine-type communications. In *IEEE Global Communications Conference (GLOBECOM)*, pp. 1–6.

[27] Han, K. and K. Huang (2017). Wirelessly powered backscatter communication networks: Modeling, coverage, and capacity. *IEEE Trans. Wireless Commun. 16*(4), 2548–2561.

[28] Han, Z. (2012). *Game theory in wireless and communication networks: theory, models, and applications*. Cambridge University Press.

[29] Hellbourg, G., A. Chippendale, J. Tuthill, and B. Jeffs (2015). Statistical performance of reference antenna based spatial RFI mitigation for radio astronomy. In *Antennas and Propagation & USNC/URSI National Radio Science Meeting, 2015 IEEE International Symposium on*, pp. 1518–1519. IEEE.

[30] Hu, R. Q. and Y. Qian (2014). An energy efficient and spectrum efficient wireless heterogeneous network framework for 5G systems. *IEEE Communications Magazine 52*(5), 94–101.

[31] Inaltekin, H., M. Chiang, H. V. Poor, and S. B. Wicker (2009). On unbounded path-loss models: effects of singularity on wireless network performance. *IEEE Journal on Selected Areas in Communications 27*(7).

[32] ITU-R (2003, Jun.). Preferred frequency bands for radio astronomical measurements. Recommendation RA.314-10, ITU.

[33] ITU-T (June. 2015). *Reference guide to quality of experience assessment methodologies.* ITU-T, Recommendation ITU-T G.1011.

[34] Jeffs, B. D., L. Li, and K. F. Warnick (2005). Auxiliary antenna-assisted interference mitigation for radio astronomy arrays. *IEEE Trans. Signal Process. 53*(2), 439–451.

[35] Kay, S. M. (1993). Fundamentals of statistical signal processing, volume i: Estimation theory.

[36] Kelly, F. (1997). Charging and rate control for elastic traffic. *Transactions on Emerging Telecommunications Technologies 8*(1), 33–37.

[37] Kim, S. H. and D. I. Kim (2019). Traffic-aware backscatter communications in wireless-powered heterogeneous networks. *IEEE Transactions on Mobile Computing*.

[38] Lan, T., D. Kao, M. Chiang, and A. Sabharwal (2010). An axiomatic theory of fairness in network resource allocation. In *IEEE INFOCOM*, pp. 1–9.

[39] Liao, Y., L. Song, Z. Han, and Y. Li (2015). Full duplex cognitive radio: a new design paradigm for enhancing spectrum usage. *IEEE Communications Magazine 53*(5), 138–145.

[40] Lien, S.-Y., K.-C. Chen, and Y. Lin (2011). Toward ubiquitous massive accesses in 3GPP machine-to-machine communications. *IEEE Commun. Mag. 49*(4).

[41] Lin, K., W. Wang, X. Wang, W. Ji, and J. Wan (2015). QoE-driven spectrum assignment for 5G wireless networks using SDR. *IEEE Wireless Communications 22*(6), 48–55.

[42] Lin, X., J. G. Andrews, and A. Ghosh (2014). Spectrum sharing for device-to-device communication in cellular networks. *IEEE Transactions on Wireless Communications 13*(12), 6727–6740.

[43] Liu, V., A. Parks, V. Talla, S. Gollakota, D. Wetherall, and J. R. Smith (2013). Ambient backscatter: wireless communication out of thin air. In *ACM SIGCOMM Computer Communication Review*, pp. 39–50. ACM.

[44] Liu, W., Y.-C. Liang, Y. Li, and B. Vucetic (2018). Backscatter multiplicative multiple-access systems: Fundamental limits and practical design. *IEEE Transactions on Wireless Communications 17*(9), 5713–5728.

[45] Liu, Y., Z. Ding, M. Elkashlan, and J. Yuan (2016). Nonorthogonal multiple access in large-scale underlay cognitive radio networks. *IEEE Transactions on Vehicular Technology 65*(12), 10152–10157.

[46] Liu, Y., C. Yuen, X. Cao, N. U. Hassan, and J. Chen (2014). Design of a scalable hybrid MAC protocol for heterogeneous M2M networks. *IEEE Internet of Things Journal 1*(1), 99–111.

[47] Liu, Y., C. Yuen, J. Chen, and X. Cao (2013). A scalable hybrid MAC protocol for massive M2M networks. In *IEEE Wireless Communications and Networking Conference (WCNC)*, pp. 250–255.

[48] Lu, X., D. Niyato, H. Jiang, D. I. Kim, Y. Xiao, and Z. Han (2018). Ambient backscatter assisted wireless powered communications. *IEEE Wireless Communications*.

[49] Luo, Z.-Q. and S. Zhang (2008). Dynamic spectrum management: Complexity and duality. *IEEE Journal of Selected Topics in Signal Processing 2*(1), 57–73.

[50] Malak, D., H. S. Dhillon, and J. G. Andrews (2016). Optimizing data aggregation for uplink machine-to-machine communication networks. *IEEE Transactions on Communications 64*(3), 1274–1290.

[51] Meng, J. J., W. Yin, H. Li, E. Hossain, and Z. Han (2011). Collaborative spectrum sensing from sparse observations in cognitive radio networks. *IEEE Journal on Selected Areas in Communications 29*(2), 327–337.

[52] Minn, H., Y. R. Ramadan, and Y. Dai (2016). A new shared spectrum access paradigm between cellular wireless communications and radio astronomy. In *Global Communications Conference (GLOBECOM), IEEE*, pp. 1–6.

[53] Mitola, J., J. Guerci, J. Reed, Y.-D. Yao, Y. Chen, T. Clancy, J. Dwyer, H. Li, H. Man, R. McGwier, et al. (2014). Accelerating 5G QoE via public-private spectrum sharing. *IEEE Communications Magazine 52*(5), 77–85.

[54] National Research Council (2007). *Handbook of Frequency Allocations and Spectrum Protection for Scientific Uses*. National Academies Press.

[55] National Research Council (2010). *Spectrum management for science in the 21st century*. National Academies Press.

[56] Novlan, T. D., H. S. Dhillon, and J. G. Andrews (2013). Analytical modeling of uplink cellular networks. *IEEE Transactions on Wireless Communications 12*(6), 2669–2679.

[57] Pankonin, V. and R. Proce (1981, Aug.). Radio astronomy and spectrum management: The impact of WARC-79. *IEEE Trans. Commun. COM-29*(8), 1228–1237.

[58] Park, I., D. Kim, and D. Har (2015). MAC achieving low latency and energy efficiency in hierarchical M2M networks with clustered nodes. *IEEE Sensors J. 15*(3), 1657–1661.

[59] Pritzker, P. and L. E. Strickling (June 2014). Fourth interim progress report on the ten-year plan and timetable and plan for quantitative assessments of spectrum usage. Technical report.

[60] Psomas, C. and I. Krikidis (2017). Backscatter communications for wireless powered sensor networks with collision resolution. *IEEE Wireless Communications Letters 6*(5), 650–653.

[61] Qian, J., F. Gao, G. Wang, S. Jin, and H. Zhu (2017). Noncoherent detections for ambient backscatter system. *IEEE Trans. Wireless Commun. 16*(3), 1412–1422.

[62] Qiu, W., B. Xie, H. Minn, and C.-C. Chong (2012). Interference-controlled transmission schemes for cognitive radio in frequency-selective time-varying fading channels. *IEEE Transactions on Wireless Communications 11*(1), 142–153.

[63] Ramadan, Y. R., Y. Dai, H. Minn, and F. Rodrigues (2016, 17-20 Oct.). Spectrum sharing between WiFi and radio astronomy. In *Radio Frequency Interference (RFI)*. IEEE.

[64] Ramadan, Y. R., H. Minn, and Y. Dai (2017). A new paradigm for spectrum sharing between cellular wireless communications and radio astronomy systems. *IEEE Transactions on Communications*. DOI: 10.1109/TCOMM.2017.2709319.

[65] Ruttik, K., R. Duan, R. Jäntti, and Z. Han (2018). Does ambient backscatter communication need additional regulations? In *IEEE International Symposium on Dynamic Spectrum Access Networks*, pp. 1–6.

[66] Saha, C., M. Afshang, and H. S. Dhillon (2018). 3GPP-inspired HetNet model using Poisson cluster process: Sum-product functionals and downlink coverage. *IEEE Transactions on Communications 66*(5), 2219–2234.

[67] Saleem, K., A. Derhab, and J. Al-Muhtadi (2014). Low delay and secure M2M communication mechanism for e-healthcare. In *IEEE 16th International Conference on e-Health Networking, Applications and Services (Healthcom)*, pp. 105–110.

[68] Sardarabadi, A. M., A.-J. van der Veen, and A.-J. Boonstra (2016). Spatial filtering of RF interference in radio astronomy using a reference antenna array. *IEEE Transactions on Signal Processing 64*(2), 432–447.

[69] Tefek, U. and T. J. Lim (2016, April). Clustering and radio resource partitioning for machine-type communications in cellular networks. In *IEEE Wireless Communications and Networking Conference*, pp. 1–6.

[70] Tefek, U. and T. J. Lim (2017, Feb). Relaying and radio resource partitioning for machine-type communications in cellular networks. *IEEE Trans. Wireless Commun. 16*(2), 1344–1356.

[71] Thompson, A. R. (2004). ITU-R recommendations of particular importance to radio astronomy. In *Spectrum Management for Radio Astronomy*, Volume 1, pp. 121.

[72] Tu, C.-Y., C.-Y. Ho, and C.-Y. Huang (2011). Energy-efficient algorithms and evaluations for massive access management in cellular based machine to machine communications. In *IEEE Vehicular Technology Conference (VTC Fall)*, pp. 1–5.

[73] Uddin, F. (2017). Energy-aware optimal data aggregation in smart grid wireless communication networks. *IEEE Transactions on Green Communications and Networking 1*(3), 358–371.

[74] Van Driel, W. (2009). Radio quiet, please!–Protecting radio astronomy from interference. *Proceedings of the International Astronomical Union 5*(S260), 457–464.

[75] Van Huynh, N., D. T. Hoang, X. Lu, D. Niyato, P. Wang, and D. I. Kim (2018). Ambient backscatter communications: A contemporary survey. *IEEE Commun. Surveys Tuts. 20*(4), 2889–2922.

[76] Verma, P. K., R. Verma, A. Prakash, A. Agrawal, K. Naik, R. Tripathi, M. Alsabaan, T. Khalifa, T. Abdelkader, and A. Abogharaf (2016). Machine-to-Machine (M2M) communications: A survey. *Journal of Network and Computer Applications 66*, 83–105.

[77] Wang, G., F. Gao, R. Fan, and C. Tellambura (2016). Ambient backscatter communication systems: Detection and performance analysis. *IEEE Trans. Commun. 64*(11), 4836–4846.

[78] Weber, S., J. G. Andrews, and N. Jindal (2010). An overview of the transmission capacity of wireless networks. *IEEE Trans. Commun. 58*(12), 3593–3604.

[79] Wen, X., S. Bi, X. Lin, L. Yuan, and J. Wang (2019). Throughput maximization for ambient backscatter communication: A reinforcement learning approach. *arXiv preprint arXiv:1901.00608*.

[80] Wildemeersch, M., T. Q. Quek, M. Kountouris, A. Rabbachin, and C. H. Slump (2014). Successive interference cancellation in heterogeneous networks. *IEEE transactions on communications 62*(12), 4440–4453.

[81] Wilson, T. L., K. Rohlfs, and S. Hüttemeister (2009). *Tools of radio astronomy*, Volume 5. Springer.

[82] Wu, D., Q. Wu, Y. Xu, J. Jing, and Z. Qin (2017). QoE-based distributed multichannel allocation in 5G heterogeneous cellular networks: A matching-coalitional game solution. *IEEE Access 5*, 61–71.

[83] Yang, G., Q. Zhang, and Y.-C. Liang (2018). Cooperative ambient backscatter communications for green internet-of-things. *IEEE Internet of Things Journal 5*(2), 1116–1130.

[84] Yucek, T. and H. Arslan (2009). A survey of spectrum sensing algorithms for cognitive radio applications. *IEEE communications surveys & tutorials 11*(1), 116–130.

[85] Zhang, H., C. Jiang, N. C. Beaulieu, X. Chu, X. Wang, and T. Q. Quek (2015). Resource allocation for cognitive small cell networks: A cooperative bargaining game theoretic approach. *IEEE Transactions on Wireless Communications 14*(6), 3481–3493.

[86] Zhang, N., S. Zhang, J. Zheng, X. Fang, J. W. Mark, and X. Shen (2017). QoE driven decentralized spectrum sharing in 5G networks: Potential game approach. *IEEE Transactions on Vehicular Technology 66*(9), 7797–7808.

[87] Zhao, G., G. Y. Li, and C. Yang (2009). Proactive detection of spectrum opportunities in primary systems with power control. *IEEE transactions on wireless Communications 8*(9).

BIOGRAPHICAL SKETCH

Dong Han was born in Liaoning, China. He received a BE degree in Communication Engineering from University of Electronic Science and Technology of China, Chengdu, in 2015 and a MS degree in Electrical Engineering from National University of Singapore in 2016. He is a PhD candidate in Electrical Engineering at The University of Texas at Dallas, Richardson, TX, USA. His research research works are in the areas of machine-type communications, air-to-ground communication systems, and the interdisciplinary research between NGSO satellite communications and radio astronomy systems.

He was a wireless system engineer intern at Corning Optical Communications SpiderCloud, San Diego, CA, USA, from May 2019 to August 2019. He was a research/teaching assistant at The University of Texas at Dallas, Richardson, TX, USA, from 2016 to 2020. He received the Louis Beecherl Graduate Fellowship and the Jan Van der Ziel Fellowship in 2018 and 2019, respectively.

CURRICULUM VITAE

Dong Han

May 2020

Contact Information:

Department of Electrical Engineering
The University of Texas at Dallas
800 W. Campbell Rd.
Richardson, TX 75080, U.S.A.

Email: dong.han6@utdallas.edu

Educational History:

BE, Communications Engineering, University of Electronic Science and Technology of China, Chengdu, China, 2015
MS, Electrical Engineering, National University of Singapore, Singapore, 2016
PhD, Electrical Engineering, The University of Texas at Dallas, Richardson, TX, USA, 2020
Advisor: Dr. Hlaing Minn

Employment History:

Wireless system engineer intern, Corning Optical Communications SpiderCloud, May 2019 – August 2019
Research/Teaching Assistant, University of Texas at Dallas, TX, USA, August 2016 – May 2020

Professional Recognitions and Honors:

Louis Beecherl Graduate Fellowship, The University of Texas at Dallas, TX, USA, 2018
Jan Van der Ziel Fellowship, The University of Texas at Dallas, TX, USA, 2019

Professional Memberships:

Institute of Electrical and Electronics Engineers (IEEE), 2017–present
IEEE Communications Society (IEEE ComSoc), 2018–present

PUBLICATIONS

Journals

1. **Dong Han** and Hlaing Minn, "Coverage Probability Analysis under Clustered Ambient Backscatter Nodes,"*IEEE Wireless Communication Letters*, vol. 8, no. 6, pp. 1713-1717, Sept. 2019.

2. Yucheng Dai, **Dong Han** and Hlaing Minn, "Impacts of Large-Scale NGSO Satellites: RFI and A New Paradigm for Satellite Communications and Radio Astronomy Systems,"*IEEE Transactions on Communications*, vol. 67, no. 11, pp. 7840-7855, July 2019.

3. **Dong Han**, Hlaing Minn, Utku Tefek and Teng Joon Lim "Network Dimensioning, QoE Maximization and Power Control for Multi-Tier Machine-Type Communications,"*IEEE Transactions on Communications*, vol. 67, no. 1, pp. 859-872, Jan. 2019.

4. **Dong Han** and Hlaing Minn, "Performance Analysis of Distributed Auxiliary Radio Telescopes Under Shared Spectrum Access Paradigm and Cooling Power Constraint,"*IEEE Access*, vol. 5, pp. 21709-21722, Oct. 2017.

5. Qiang Li, Wing-Kin Ma, and **Dong Han**, "Sum Secrecy Rate Maximization for Full-Duplex Two-Way Relay Networks Using Alamouti-based Rank-Two Beamforming,"*IEEE Journal of Selected Topics in Signal Processing*, vol. 10, no. 8, pp. 1359-1374, Dec. 2016.

Conferences

1. Hlaing Minn, **Dong Han**, and Yucheng Dai, "A New Paradigm for Non-Geostationary Satellite Communications and Radio Astronomy System,"in *IEEE International Conference on Communications (ICC) 2018*, Kansas City, May 2018.

2. **Dong Han** and Hlaing Minn, "Performance Analysis of Distributed Radio Telescopes under Shared Spectrum Access Paradigm," in *IEEE Global Communications Conference (Globecom) 2017*, Singapore, December 2017.

3. **Dong Han**, Utku Tefek, Teng Joon Lim, and Hlaing Minn, "Network Dimensioning and Radio Resource Management for Multi-Tier Machine-Type Communications," in *IEEE Global Communications Conference (Globecom)*, Singapore, December 2017.

4. Qiang Li and **Dong Han**, "Sum Secrecy Rate Maximization for Full-Duplex Two-way Relay Networks, " in *IEEE International Conference on Acoustics, Speech, and Signal Processing (ICASSP)*, Shanghai, March 2016.